FREE FORMING
OF
LOCALLY LASER HEATED PARTS

A THESIS SUBMITTED TO
THE GRADUATE SCHOOL OF NATURAL AND APPLIED SCIENCES
OF
MIDDLE EAST TECHNICAL UNIVERSITY

BY

MURAT ÖZMEN

IN PARTIAL FULFILLMENT OF THE REQUIREMENTS
FOR
THE DEGREE OF MASTER OF SCIENCE
IN
MECHANICAL ENGINEERING

MARCH 2005

Approval of the Graduate School of Natural and Applied Sciences

_____

Prof. Dr. Canan ÖZGEN
Director

I certify that this thesis satisfies all the requirements as a thesis for the degree of Master of Science.

_____

Prof. Dr. Kemal İDER
Head of Department

This is to certify that we have read this thesis and that in our opinion it is fully adequate, in scope and quality, as a thesis for the degree of Master of Science.

_____

Prof. Dr. A. Erman Tekkaya
Supervisor

Examining Committee Members

Prof. Dr. Engin Kılıç	(METU, ME)	_____
Prof. Dr. A. Erman Tekkaya	(METU, ME)	_____
Prof. Dr. Zafer Dursunkaya	(METU, ME)	_____
Assoc. Prof. Dr. Hakan Gür	(METU, METE)	_____
Assoc. Prof. Dr. Suat Kadıoğlu	(METU, ME)	_____

I hereby declare that all information in this document has been obtained and presented in accordance with academic rules and ethical conduct. I also declare that, as required by these rules and conduct, I have fully cited and referenced all material and results that are not original to this work.

Murat ÖZMEN

ABSTRACT

FREE FORMING OF LOCALLY LASER HEATED SPECIMENS

Özmen, Murat

M.S., Department of Mechanical Engineering

Supervisor: Prof. Dr.-Ing. A. Erman Tekkaya

March 2005, 166 pages

As metals have high formability at elevated temperatures, hot forming is preferred and widely used in manufacturing of complicated geometries. The term “hot forming” is usually used if the whole workpiece is processed at elevated temperatures. However, for certain products high formability is required only locally. Forming by local heating is proposed to provide ease of manufacturing of local forms on the workpiece. Also, tools can be simplified by this method. In this study, local laser heating procedures are applied to obtain local forms on cylindrical bulk metal products in a single step. Locally heated workpieces are formed between two flat dies. Both solid and hollow products have been investigated experimentally and by finite element modeling. The experimental studies and finite element analyses are done simultaneously in order to obtain optimum local deformation characteristics. Three different materials together with different initial geometries and various local laser-heating procedures are applied to search for the process window. The limits of applicability are determined and examples of application are supplied.

Keywords: Cold Forging, Hot Forging, Local Laser Heating, Finite Element Analysis

ÖZ

LAZER İLE LOKAL OLARAK ISITILAN PARÇALARIN ŞEKİLLENDİRİLMESİ

Özmen, Murat
Yüksek Lisans, Makina Mühendisliği Bölümü
Tez Yöneticisi: Prof. Dr.-Ing. A. Erman Tekkaya

Mart 2005, 166 sayfa

Metaller yüksek sıcaklıklarda daha kolay işlenebildiklerinden karmaşık şekilli parçaların üretiminde sıcak şekillendirme daha yaygın olarak tercih edilir ve uygulanır. Herbiri avantaj ve dezavantajlara sahiptir. "Sıcak Şekillendirme" terimi daha çok iş parçasının tamamının yüksek sıcaklıklarda işlenmesi durumu için kullanılmaktadır. Buna karşın, bazı ürünler için iş parçasında sadece bölgesel bir şekillendirmeye ihtiyaç duyulabilmektedir. Parça üzerinde bölgesel deformasyonların elde edilmesini gerektiren bu durumda bölgesel ısıtmaya dayalı bir şekillendirme işlemi üretim kolaylığı sağlayacaktır. Bunun yanısıra daha basit ekipmanların kullanımına da imkan verilecektir. Bu çalışmada lazer ile bölgesel olarak ısıtılan silindirik parçalarda tek işlemde ve sadece düz kalıplar kullanılarak lokal deformasyonların elde edilmesi amaçlanmıştır. İşlem bütün ve boru parçalar üzerinde deneysel olarak ve sonlu elemanlar yöntemi ile analiz edilmiştir. Bu çalışmaların birarada yürütülmesi suretiyle bölgesel deformasyon optimum seviyeye çıkartılmıştır. İşlemin sınırlarının belirlenmesi amacıyla değişik ilk geometrilerde üç farklı malzeme kullanılmıs ve lazerle ısıtma için farklı işlemler uygulanmıştır. Çalışma sonucu çıkan ürünlerden örnekler sunulmuştur.

Anahtar Kelimeler: Soğuk Dövme, Sıcak Dövme, Lazerle Bölgesel Isıtma, Sonlu Eleman Analizleri

ACKNOWLEDGEMENT

I would like to express my deepest gratitude and appreciation to my supervisor Prof. Dr.-Ing. A . Erman Tekkaya, who inspired, encouraged and supported me for this study.

I would like to thank to my colleague Oya Okman for his support and contribution

I would like to thank to my colleagues Dr.-Ing. Ursula Weidig, Christian Schelle, Tiziano Minghetti, and Hansruedi Huwiler, whose help and guidance made great contribution to this work.

This study was carried out at METU and RUAG Components as a cooperative research project. The support provided by METU Graduate School of Natural and Applied Sciences and RUAG Munition is greatly acknowledged.

I would like to thank Devrez, Elif, Çağrı, Ozan, Çiğdem for being such great friends and being with me in many memorable moments. I also would like to thank Bahar Tunçel for her positive energy that motivated me to write this thesis.

My best wishes to METU Technopolis group and Femlab members Ahmet Kurt, Kürşad Kayatürk, Mete Egemen, Halil Bil, Özgür Koçak, Muhsin Öcal for their patience and support

The greatest thanks go to my family members, my parents Kamuran and Mustafa Özmen, my sister Özge for their endless support and trust throughout my education.

TABLE OF CONTENTS

LIST OF TABLES

TABLE

LIST OF FIGURES

FIGURE

CHAPTER 1

INTRODUCTION

1.1 Bulk Metal Forming

According to DIN 8580 norm, metal forming is the manufacturing by plastic (permanent) change of the form of a solid body by preserving both the mass and cohesion. In other words, metal forming includes the plastic deformation of metals in either a cold or a hot state by some mechanical means, which does not include processes where metal is machined off nor does it include casting molten metal into the required form by the help of molds. This deformation is realized in the form of forging, bending, drawing or shearing throughout the process [1]. The workpiece may be either cold or hot formed. Here, cold working includes the cases where the temperature of the metal is around room temperature in everyday sense. On the other hand hot working occurs under conditions of temperature and strain rate such that recrystallization occurs simultaneously with deformation. Also warm forming term is used for the temperature range of below and around the recrystallization temperature (Table 1.1).

Regardless of the process temperature, bulk metal forming processes have some distinct advantages. High material utilization and high productivity with short production times make metal forming processes economic for production of many parts. In addition to this, the products are manufactured in high dimensional and shape accuracy within certain tolerances. Finally, especially for dynamic loadings, the final products have superior mechanical material properties [2].

Table 1.1 Classification of metal forming processes according to temperature

	Metal Forming Processes		
	Cold Forming	**Warm Forming**	**Hot Forming**
Temperature Range	Forming Below the Recrystallization Temperature	Forming Below or Around the Recrystallization Temperature	Forming Above the Recrystallization Temperature
Example	Steel : Room Temperature	Steel : 750 – 950 ^{o}C	Steel : 1150 – 1250 ^{o}C

1.1.1 Hot Forming Processes:

Hot working is defined as the plastic deformation of metals above their recrystallization temperature. The main advantages of the hot working processes are as follows [1];

- Energy requirement for the deformation is far less than that is for the cold working case
- Physical properties such as ductility, resistance to impact, and strength are generally improved, mainly as a result of the refinement of the coarse or columnar grains
- Impurities in the form of inclusions are broken up and distributed through the metal
- Porosity in the metal is eliminated

Naturally, the hot working applications have a few disadvantages that have to be taken into account during production. Hot working processes result generally a poor surface finish because of rapid oxidation or scaling of the material surface. As a result of scaling, close tolerances are usually difficult to be maintained. In addition to this extra energy is required for the heating process. Finally, the equipment and maintenance costs are high compared to the cold working applications.

1.1.2 Cold Forming Processes

Many of the operations used in hot forming may also be applied in cold forming, but the resulting effect on the crystalline structure and the physical properties varies. In hot forming the grain size is refined whereas in the cold working case, grains are merely distorted.

In order to deform the material, stresses exceeding the elastic limit at room temperature must be applied, which means greater pressures compared to the hot forming case. This brings about the requirement of heavier and more powerful equipment. Another important parameter in cold working is the ductility of the material, which determines the amount of cold work that the material will withstand. The final product will surely have less ductility compared to the initial one. In addition to this some residual stresses are likely to occur in the material. Also, in metallurgical point of view, imparted directional properties may be detrimental. These points make cold forming processes rather disadvantageous but there exist also advantages compared to hot working processes [1]. These are;

- Superior dimensional control is achieved
- Strength, fatigue and wear properties are improved as a result of strain hardening
- Better surface finish is obtained
- High production rates are possible as no heating is required
- Extra power is not required for heating

1.2 The Process Idea

1.2.1 Motivation

As a result of the facts explained above, conventional cold working processes appear to be inefficient for the production of the local forms on axisymetrical

workpieces. The suitable traditional methods are usually costly as complicated dies and high forming loads are required. In addition to this, the applied force should be even higher to ensure precision in case of near net shape applications.

The disadvantages of the cold working process in the manufacturing of local forms can be avoided by utilizing free forming together with local heating of the workpieces in the bulge area. By this way, energy is saved compared to a completely hot processing and additional operations like scale removal from the surface of the specimen, are eliminated. The flow stress of the material in the bulge area is decreased when it is heated up to an elevated temperature, above recrystallization temperature and below the melting point of the metal. The press force applied to the specimen will cause a more dominant material flow in this area compared to other regions of the specimen and locally high deformations can be obtained. The combined process will be different from the warm forming processes in which, not only the advantages but also the disadvantages of both the cold and hot forming processes are contained.

1.2.2 Aim and Scope of the Study

This study is focused on the applications of free forming process by local heating in order to obtain local forms on axisymetrical specimens. An innovative way of producing such forms is suggested by applying laser heating procedures for preheating purposes. In this method, it is aimed to make use of the highly local heating capability of laser heating procedures. As a result of the local heating, local deformation is expected in the subject area after the formation step. The idea behind this strategy is the reduction of flow stress of the metal in the locally heated region as previously stated.

In order to determine the availability and the limits of the process experiments are conducted and finite element method is applied for further analyses. The experiments are realized in four steps, that are;

- Specimen is clamped between two flat dies (without any formation)
- Laser heating procedures are applied by the help of the portable laser head which is mounted on a five-axis robot arm
- Laser head is drawn back
- Locally heated specimen is free formed between the flat dies
- Final product is cooled in air or water jet

The initial and final shapes of the specimen can be seen in Figure 1.1.

On the other hand, finite element analyses are utilized to find the limitations of the process and to obtain a process window. For this purpose, a commercial finite element method tool MSC/Marc is used for simulations. Finite element method simulations are mainly used to understand the ongoing process better and to define way for the following experiments.

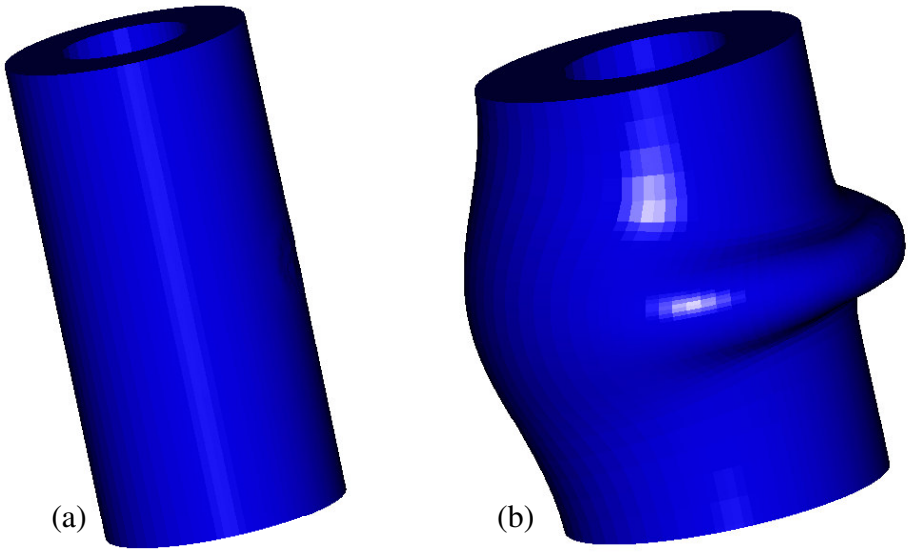

Figure 1.1 (a) Initial workpiece and (b) final product.

The thesis report on this study is composed of mainly eight chapters. Being the introduction chapter, this one gives overall information about the metal forming processes and the suggested application. The following chapter will be on literature

survey where previous studies on similar applications are investigated and brief information about laser physics is given. Third chapter will cover the summary of the finite element method and the simulation tool used. Experimental studies will be given in the fourth chapter. In Chapter 5, metallurgical results of the experiments are going to be examined especially to define the heat-affected areas. The solution parameters together with the modeling details will be presented in Chapter 6. The simulation results and explanations on the process characteristics will be given in the seventh chapter. Finally the last chapter will be composed of discussions, conclusion and further recommendations.

CHAPTER 2

LITERATURE SURVEY

2.1 Introduction

In this chapter, previous literature related to the current study will be covered. First, introductory information on lasers and their areas of application will be given. The local heating capability of the lasers will be discussed. Secondly, previous researches on the production of local forms will be presented.

2.2 Physics of Laser

The laser is a device that produces an emission of coherent electromagnetic energy by employing the principles of quantum electronics. This explanation can be simplified to an introduction level by regarding the laser as a special kind of lamp that emits a very bright light, which is extremely pure in color and can be focused onto a very tiny spot.

The term LASER is an acronym, which is formed by putting together the initial letters of the following words:

Light
Amplification by
Stimulated
Emission of
Radiation

The deeper explanation of these words will be given throughout the chapter. There are four important features that make the laser different from the other sources of light, such as lamps, flames or stars. These are; laser light is much more intense, it is in a narrow beam mode, it is monochromatic (one color), and also it is coherent. Further explanations on those are [3];

Intensity:

Intensity of the laser light can be made extraordinarily high, even much brighter than the sun light. By using the lasers it is possible to obtain bursts of light that is more than a billion watts of energy in a beam of about 1 cm^2. Also the laser can be focused down to tiny spots where the concentrated energy can reach beyond 10 gigawatts per cm^2.

Directionality:

Lasers have the specialty to emit very narrow beams of light. Their beams spread very little, and carry much farther as the energy is not wasted by spreading out widely.

Monochromaticity:

The term "monochromatic" means "one color", which represents only one wavelength. An ordinary lamp or the sun emits light that is composed of many different colors, which are mixed together. This is called "white light". A laser light is only one color and usually a pure color too. Also, it is possible to produce laser in any color of the rainbow. Laser even produce forms of light that the human eye can't see, which are infrared (IR) and ultraviolet (UV) radiation.

Coherence:

The coherent light has the property that all the waves are exactly alike, that is all the same height, all the same direction (spatial coherence) and always the same spacing between them (temporal coherence). The laser light is perfectly coherent. This is worth emphasizing since it is the basis in laser technology. Laser can be defined as the first coherent source of light ever designed and developed by man (Figure 2.1).

In order to understand the physics of the laser, it is necessary to start from the elementary concepts of the atomic theory. The positions of the electrons in the orbits play a critical role in realizing the laser.

Rest state is the state of the atom (and the electron), when the electron is in its lowest possible orbit, which is also the lowest energy level. The electron can be stimulated to move to a higher orbit if a quantum of energy (a photon) is absorbed. This new state is called the *excited state*. But, according to the minimum energy principle, the electron tends to move back to the lowest energy level and when this happens, a photon is given off. The important point in this concept is that, the electron cannot be excited unless exactly the right quantum of energy is received.

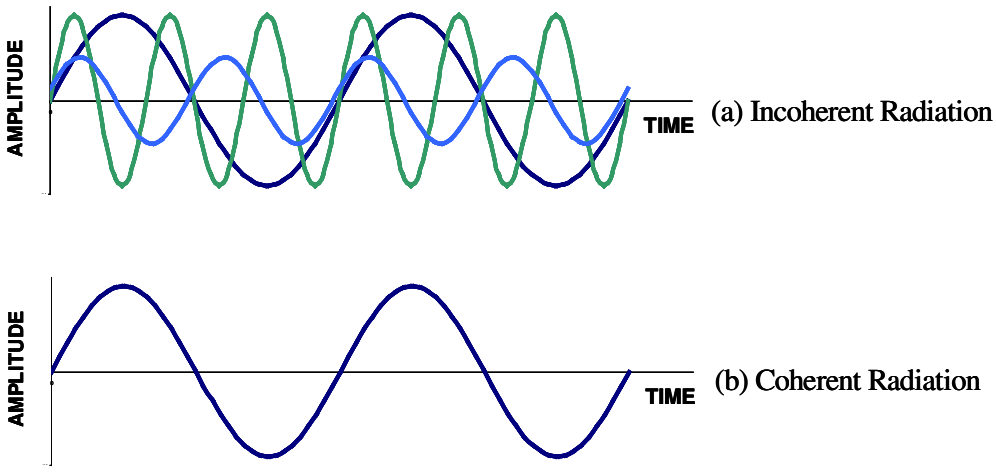

Figure 2.1 Sine waves of coherent and incoherent radiation [4].

When the atom releases a photon, a photon of certain fixed set of wavelengths are released which can be regarded as the "magic point" in LASER. The atoms can be identified by the wavelengths of the photons, they emit.

According to Einstein, there are three processes involved in absorbing or giving off the energy of a gas; absorption, emission, and stimulated emission [3];

Absorption:

When a quantum of energy (a photon) is received and interacts with an atom, the atom goes to an excited state as it gains energy by absorption (Figure 2.2).

Spontaneous Emission:

Emission occurs if an electron of the excited atom hops down from its high energy level to low energy level and gives off a photon in this process. As the atom de-excites itself and there is no external factor in the process, this type of emission is called the *spontaneous emission* (Figure 2.2).

Stimulated Emission:

Einstein's prediction states that there may be times when an excited atom is hit by a photon and in this particular case the atom don't get "more" excited but the electron drops back to the lower energy orbit and again gives off a photon. But this time the former photon that hit the atom is not absorbed and continues its way. As a result two photons come out where there had been just one, previously (Figure 2.2).

The important point in the development of laser is to find a way to "pump up" an atom to an excited state and keep it there, preventing from undergoing a spontaneous emission. By this way, a large number of atoms can be kept ready to be stimulated emission. This process is called the *population inversion*. The equilibrium condition is set as, *well populated* ground state and *poorly populated* excited state. A population inversion is required to obtain the laser. That is almost to depopulate the ground state, while the excited state gets populated [5].

Theodore Maiman was the first to build a laser at the Hughes Research Laboratories in Malibu. The working medium of Maiman's laser was an artificial ruby crystal, which is actually a different form of aluminum oxide where some of the aluminum atoms are replaced by chromium atoms (about 0,05 %). Knowing the fact that, the ruby crystals fluoresce when exposed to strong pulses of light, Maiman used a powerful flash lamp in order to excite the chromium atoms by the burst of light. A helical flash lamp was placed around the ruby rod so that the light would be received by the entire surface of the rod. The ends of the ruby rod was processed to be perfectly parallel and also coated by silver which reflects the light up to a certain intensity after which the silver coating allow the light to go through it (Figure 2.3).

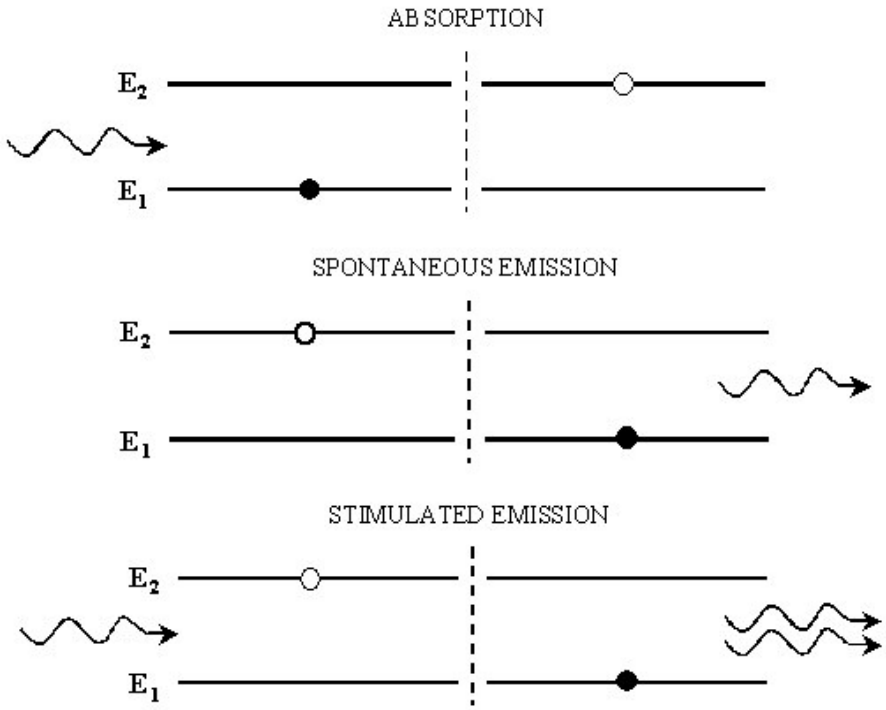

Figure 2.2 Schematic representations of absorption, spontaneous emission and stimulated emission

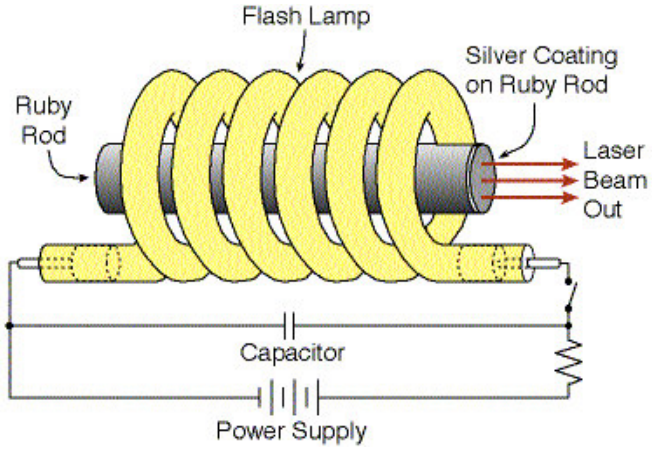

Figure 2.3 Simplified pictorial diagram of a ruby laser.

The chromium atom can reach two excited energy levels. If it reaches either of these levels, it immediately falls back to an intermediate state, but not the ground state which is about halfway between the ground and the highest energy level. This state is called the *metastable state* (partially stable state). Chromium atoms stay at

this state for about a few milliseconds, which is in fact a long time. While the atoms are in this metastable state, some of the atoms spontaneously emit photons and fall back to the ground state.

And as these photons are in exactly the same wavelength required for stimulated emission, another photon of again the same wavelength is produced. The process goes on as these photons hit the other atoms at metastable state (Figure 2.4). These photons move in almost every direction and only the ones that move exactly along the axis of the ruby rod reflects back from the silver ends and starts to increase the intensity in that direction. When the cascade of photons reaches a high enough intensity, finally it passes through the silver end and the pulse of laser light comes out [6].

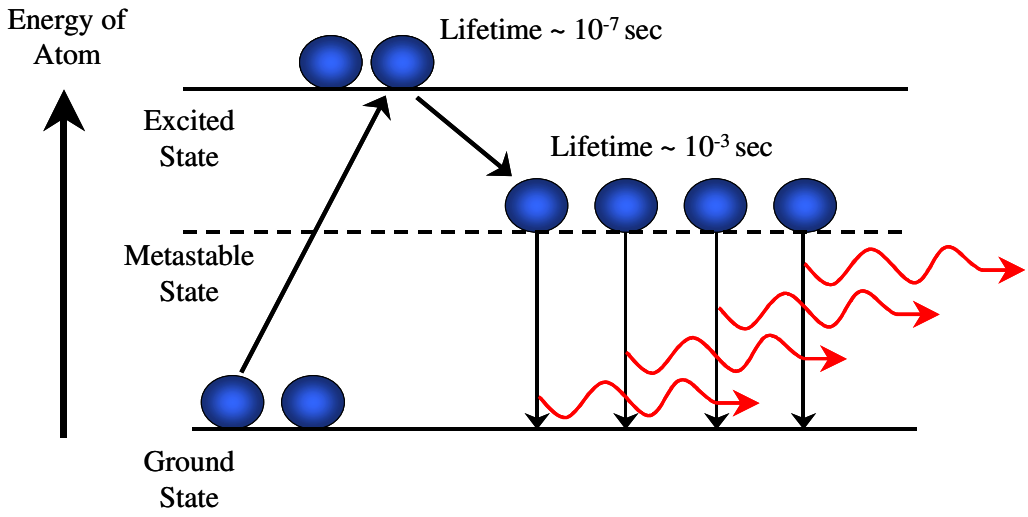

Figure 2.4 Population inversion and energy states of the chromium atom.

Apart from Chromium, a large variety of materials can be used in producing stimulated radiation. These materials are used generally in combination with different types of crystals such as ruby or other types of glass. Because of the fact that the output frequency is highly dependent on type and quantity of the doping element, it becomes possible to obtain coherent light at about any frequency, as the large number of materials is taken into consideration. Some of the most important types of lasers can be given as follows [7, 14]:

- The laser diode employing *gallium arsenide* works in the infrared part of the spectrum, which means the emissions are invisible. The infrared extends from the wavelength of 0.75 microns 1000 microns but the gallium arsenide laser operates at a wavelength of about 0.84 microns. Infrared lasers have the output power range of 100mW to 1 W and are important for communication and military purposes.
- Another common type of laser, using gas-filled tube containing the inert elements *helium and neon*, emits red light (632.8 nm) and operates at a relatively low energy level. HeNe lasers are low efficiency (0.01% to 0.1%) and low powered (max 10mW), but because they are simple and inexpensive, have become very popular. HeNe lasers are used in chemical research, spectroscopy, construction, holography, communications and weaponry.
- The *neodymium-YAG* laser is a special crystal laser, generating a continuous wave. The abbreviation *YAG* stands for yttrium-aluminum-garnet. The laser is actually a combination of liquid and solid materials, neodymium being a solution in the crystal YAG. The wavelength of this type of lasers is 1060 nm and the output powers for CW (continuous wave) mode range from 0.1 watts to 100 watts. The peak power for the pulsed mode can range from tens or hundreds of kilowatts with a pulse lasting milliseconds to over a hundred megawatts with a pulse lasting 10- 20 nanoseconds. The Nd-YAG lasers are mainly used in material processing such as drilling, spot welding, marking, surgical applications, pumping tunable visible light lasers and in military including range finders and target designators.
- The *carbon dioxide* laser is a molecular gas laser that emits radiation in the infrared region of the spectrum (with the lasing emission of 10.6μm and 9.6μm), and are the most efficient infrared lasers available. As a result, they comprise 45% of lasers built, and 98% of lasers used in industrial and medical applications. CO_2 lasers are widely used in welding, cutting, and drilling materials (CO_2 lasers are capable of cutting titanium, a procedure

difficult for mechanical cutting tools), in the heat-treatment of metals, and in medicine for surgical cutting and dermatological skin resurfacing.

- *Titanium sapphire* has the broadest tuning range (from about 660 nm to 1180nm) for any single solid-state, gas, or liquid laser medium. Titanium sapphire lasers are available as both CW and pulsed. The typical power output at 800 nm is from 150 to 1000 mW.
- *Diode* lasers are the most frequently used laser types in daily life. The advantages of diode lasers over other lasers are their high efficiency, high reliability, long lifetime, low cost and small weight. Some common uses of a laser diode are in CD/DVD players, CD-ROM drives and laser printers.

2.3 Applications of Laser

2.3.1 Lasers in Industry

As a result of the improvements in laser technology, lasers become powerful and useful tools in different branches of industry. Today, lasers can be used for making exact measurements, cutting, welding, drilling, soldering, component manufacture, quality assurance, etc. The neodymium-YAG , ruby, and carbon dioxide lasers are frequently used types of lasers in industry.

The highly directional characteristic of the laser beam makes it a useful tool in making exact measurements in even very short or long distances. The idea behind this application is based on measuring the time interval between the emitted laser light and the reflected laser light from the target object. A pulsed laser, a mirror and a timing device is enough for such a survey. In addition to this, lasers are also used for very precise measurement of small distances as they emit discrete wavelengths of energy on the order of nanometers. The technique used for this purpose is known as the interferometry. Interferometers are mainly used to ensure the given geometrical specifications of the apparatus as temperature changes, mechanical vibration or normal use can cause some misalignments or dimensional inaccuracies.

Apart from being a control device, lasers are also utilized directly in the manufacturing processes as a tool. The ability of the high-energy lasers to penetrate solid metals or concrete makes it useful to drill precise and very small holes if needed. Pulsed lasers are used in drilling more often. The hole is drilled by focusing all of the laser energy on a small area. The process of laser drilling is explained in more detail in the next section.

Cutting process is one of the most commonly used applications in industry. A suitable laser can be utilized to cut almost anything including wood, paper, plastics or rubber. A “light” version of the cutting process is used also for surface marking.

Pulsed lasers are also used more commonly in welding than continuous wave lasers. In large-scale welding applications, traditional methods are more economical to be used, but especially for micro-welding applications, lasers can be said to be the only tool. Also soldering, which can be regarded as a low temperature form of welding, can be done by utilizing the laser [8].

Metals are heat treated for different purposes; to make them harder or to remove the residual stresses. Traditionally heat treatments are done in furnaces or by using annealing wires. As an alternative to this application, continuous wave carbon dioxide lasers are utilized for heat-treating of metals. The key points in this application are; to coat the material with a substance, which is a good absorber of the laser energy, and the scanning rate.

Today, the laser applications are only economical for some extreme cases like micromachining, but with the improvements in technology it is clear that the laser will find new areas of application in industry especially as a result of its very precise process nature.

2.3.2 Laser Heating

Just like in the case of "burning glass" which uses the focused rays of the sun to ignite combustible materials, the laser light can also reappear as heat when it is absorbed.

In order to understand the heating characteristics of the laser, it is instructive to consider the results of a simplified theory, which considers heating by "continuous" laser beams. Suppose a uniform circular beam, of radius a and power w, falls perpendicularly upon a material of thermal conductivity k (Figure 2.5), and the beam is totally absorbed in a distance small compared with a, then the equilibrium temperature rise T at the center of the circular area on the surface of the material is given by [9];

$$T = \frac{W}{\pi k a} \tag{2.1}$$

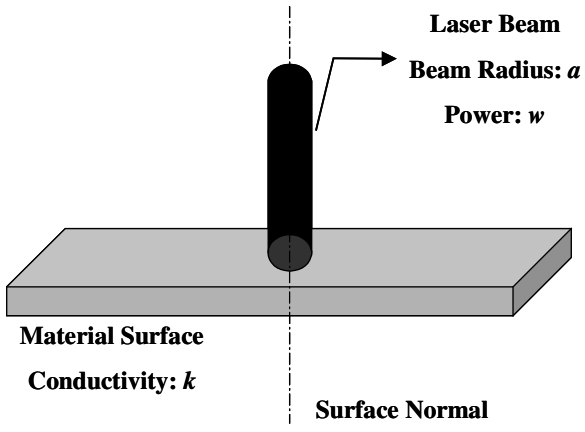

Figure 2.5 Schematic representation for Equation 2.1 and 2.2

This result is accepted to be exact only if the thickness of the material is larger compared to a. For such a case, the surfaces of constant temperature at a distance from the center of the beam large compared to a are hemispheres, and the temperature at a distance r from the origin is

$$T = \frac{W}{2\pi kr} \tag{2.2}$$

This behavior states that the heating effect of a continuous beam is highly localized. The temperature loss across the material is accepted to be negligible if the material is thin compared to the radius of the incident beam *a*, and as a results the surfaces of constant temperature are assumed to be cylindrical. No simple expression can be given for the surface temperatures in this case. On the other hand, in the case of a pulsed laser beam, we must consider transient conditions in which the flow of heat is modeled by a plane wave near the surface.

Of course, the formulations given above naturally assume that no phase changes take place during the process. The heated material does not melt or vaporize, and that the thermal constants are completely independent of the surface temperature. In many cases of application phase changes occur and the thermal constants vary distinctly with surface temperature. But, above all the equations can be said to give a useful key in predicting qualitatively what is likely to happen under given conditions.

Another important factor in heating effect of the laser is the power, which can be attained in the laser beam. The mean power, peak power and pulse duration are the important points that have to be taken into consideration in laser heating applications. The doped crystal lasers are preferred exclusively for heating applications because of the fact that they provide the highest mean power outputs at present.

The main limitation in the mean power output obtained is the heat generated in the laser rod. The heat arises from the nature of excitation process and cannot be entirely eliminated since light is always absorbed at one wavelength and emitted at a longer one. Apart from the limitation arising from the laser material, another limitation is imposed as a result of the thermal effects in the flash tubes that are used for excitation.

The applications involving the heating affects of the laser can be examined in three different titles; Low temperature applications, welding applications, and the applications involving the vaporization of the material [9].

Low-temperature applications

In low temperature applications no dominant phase change is observed in the heated material as the process is realized below the melting temperature. Process of determination of the thermal diffusivities can be examined in this kind of applications. The heat pulse, whose amount is under control, is applied to one side of the block of material and the resultant change of temperature on the other side is measured as a function of time. Another possible engineering application is the local heat treatment of metals and alloys, which can be utilized in just changing the material properties locally or as a starting step in a local deformation process as in the case of this study.

Welding applications

Laser welding is very popular and has important applications especially in the fields of electronics and microelectronics. The main reason in preferring laser welding in such applications is that; precise welding of very thin wires (as small as 10μm) or welding of very thin films is required. Also there exist some advantages that are unique for laser welding. Some of those can be given as follows;

- Extremely short times in the process makes it possible to be applied in regions adjacent to heat sensitive areas without affecting them
- Laser beam is used to apply welding in inaccessible areas, like inside a glass tube without giving harm to the tube or welding the two wires without removing the insulation
- Two dissimilar materials can be welded together by using the laser beam. Consequently, a thermocouple can be welded to a substrate without much damage to the material
- Apart from all, laser welding provides very precise location of the weld. That is to say, distortion and shrinkage of the weldment are negligible.

The factors that has to be taken into account in a pulsed laser welding application are:

1. Vaporization of the material must be prevented by monitoring the power per unit area in the laser beam.
2. The peak power value should be set as great as possible to reduce heat conduction losses and maximize the heat efficiency as the available mean power is limited.
3. The pulse time must be long enough to enable complete penetration of the melted zone to be achieved.

Applications involving vaporization

Relatively deep holes can be produced by laser applications involving the vaporization of the material. The main advantages of laser drilling can be given as follows;

- Drill-bit breakage and wear do not exist, as there is no physical contact between the material and the hole-forming tool.
- Very precise hole location is possible as the optics is used to focus the laser beam on the specimen
- Large hole depth to hole diameter ratios can be obtained.

Laser applications involving vaporization is still an inefficient method compared to the conventional methods. But, in special cases where conventional machining methods are difficult to be used, make such applications economic. Thus, it can be said that the laser applications will be widely used in “micro-machining” of materials when relatively low powers are adequate. The manufacturing of spinerettes used in fiber production and miniature ferrite cores for computers, can be given as possible applications.

2.4 Producing Local Forms by Utilizing Local Heating Techniques

The laser or any other local heating instrument can be used in the production of local forms on the workpieces by applying two different approaches. Local heating instrument can be used directly as a forming tool or for a pre-heating step in the process. The first application is mainly applied for the bending of sheet metals as well as tubular structures, whereas the second is used to force the material to flow in the desired direction by taking advantage of the local hot forming.

Laser bending, which is a new type of flexible manufacturing process for sheet metals, is an example of the first approach. The idea behind this type of processes is; heat expansion and cooling shrinkage of metals. In the study of Yanjin [10], it is shown that by applying the right laser processing parameters, it is possible to control the temperature distribution accurately and obtain the proper magnitude and distribution of the thermal stresses. This yields to the desired deformation without utilizing rigid tools or external forces.

By changing the processing parameters, it is possible to form different shapes, but mainly three types of forming mechanisms takes place [11]:

- *Temperature Gradient Mechanism*: This is the most widely used laser-bending mechanism. A differential thermal expansion through the thickness of the sheet is obtained as a result of the rapid heating of the surface by a laser beam and the slow heat conduction into the sheet. This mechanism takes place usually in thick sheets.

- *Buckling Mechanism*: Transition to the buckling mechanism occurs if the process parameters are altered. The most important parameter is the ratio of diameter of the heated area to the sheet thickness. This ratio is approximately 1 in case of temperature gradient mechanism, whereas it should be in the order of 10 for buckling mechanism. So, this mechanism is

applicable to the bending of thin sheets. As a result of this, there is no steep temperature gradient in the material. The mechanism can be summarized as the thermo-elasto-plastic buckling of the material formed as a result of the large amount of thermo-elastic strain, which is also the result of thermal compressive stresses develop in the sheet due to laser heating.

- *Upsetting Mechanism*: The process parameters in the upsetting mechanism are taken in a way similar to the buckling mechanism, but the main difference is the dimension of the laser-heated area, which is much smaller compared to the sheet thickness. This mechanism can be summarized as the shortening of the sheet and increase in thickness as a result of the nearly homogenous heating of the sheet and the restrictions in thermal expansion from the surrounding material, which causes an almost constant strain along the thickness.

Based on these different mechanisms, it is possible to obtain three distinct deformation modes:

1) *Forward bending*: a small bending angle in the direction away from the laser beam is formed (Figure 2.6a)
2) *Reverse bending*: a bending angle in the direction towards the laser beam is formed (Figure 2.6b)
3) *Elongation*: shortening of the whole cross section is obtained (Figure 2.6c)

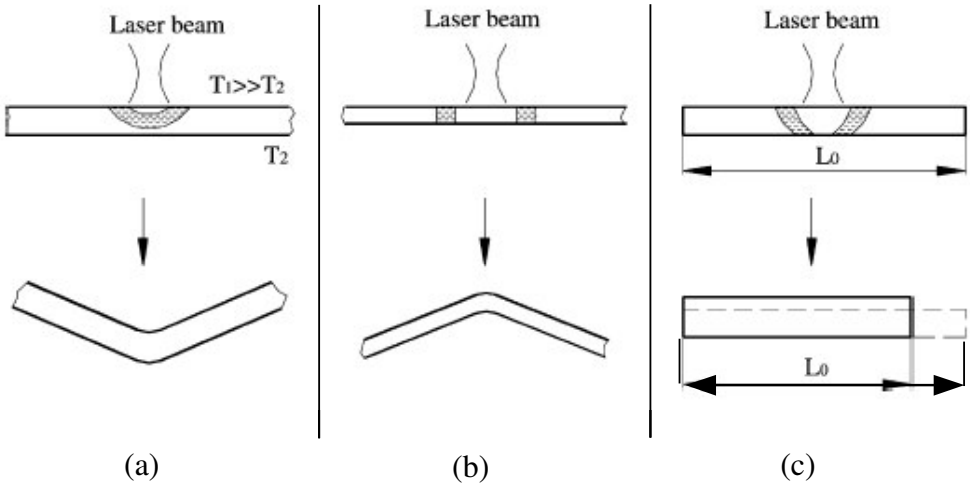

Figure 2.6 Different deformations based on different mechanisms [10]

Although this is a very innovative and flexible way of obtaining such bending forms, it is difficult to control the process especially for the thin sheets because the thin sheets can acquire forward or reverse bending with a little change in laser processing parameters.

Another application of laser bending processes is laser tube bending. The study of Li [12] shows that it is possible and also useful to use laser scanning in tube bending. It is known that, tube bending is important in the manufacturing of boilers, engines, heat exchangers and air conditioners. Mechanical methods are applied in manufacturing such products. Tensile stresses are utilized in these mechanical processes, which cause some kind of tensile failures such as neck or fracture occurring at extrados.

As in the previous sheet metal applications, laser bending of tubes is again achieved by plastic deformation induced by thermal stresses resulted from rapid heating and cooling, which results a springback free and non-contact forming technique. The process is shown schematically in Figure 2.7. Laser tube bending is suitable for small batch production, rapid prototyping, and applications where it is otherwise impossible to use mechanical bending.

Up to now, applications in which the laser heating is used as a forming tool are explained. Apart from this there exist also applications where laser heating is used as a pre-forming step. The main idea in such processes is to heat the material locally in some region and to obtain a lower flow stress in that region. Then, by mechanical means workpiece is formed and different characteristics of forming is obtained in the locally heated region. The idealized type of this idea is given in the study of Merrygold (Figure 2.8) [13].

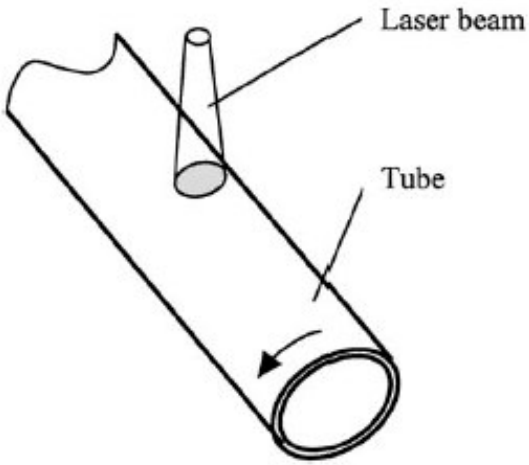

Figure 2.7 Schematic representation of laser tube bending [12].

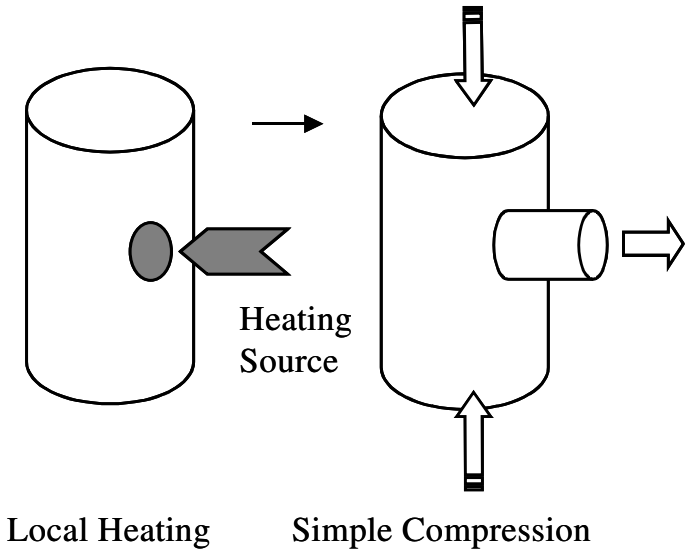

Figure 2.8 Idealized localized heating and forming.

In that study, local heating is realized by utilizing an oxyacetylene burner. The reason in selecting this tool rather than, for example, a induction heater is that, the flame heating penetrates the billet much faster which prevents the through heating of the workpiece. Different products are obtained as a result of different heating times (Figure 2.9). The induction heating was also applied to the part near the top plate and the results are shown in Figure 2.10.

Figure 2.9 The intensive flame heat was applied to an area of approximately 5x10 mm, where the billet length is 38.1 mm, the diameter is 25 mm.

A more extensive heating system will be required in order to produce parts with varying deformation in more than one location using simple compression. An example of the application can be demonstrated and idealized by the use of compound billets. Cylindrical aluminum billets of 25.4 mm diameter and 45 mm height were used and 3.5 mm holes were drilled through the billet section at various locations along the length of the billet. The holes were then filled with plasticine to simulate the softening of the material. Because the volume of the plasticine is much smaller compared to the volume of the billet, only a very small increment of compression is applied to the billet. Figure 2.11 shows the produced profile.

Figure 2.10 Part produced with induction heating

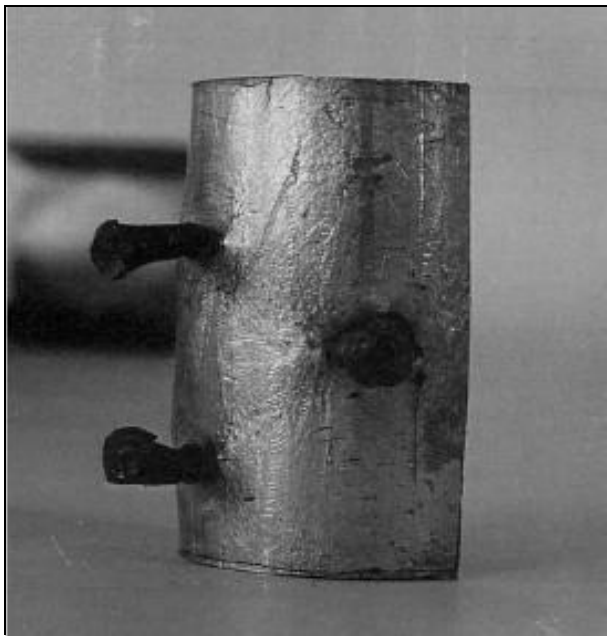

Figure 2.11 Simulation of local heating

Of course, it is impossible to obtain such large gradients of yield stress along the same material but future technologies may lead to this kind of metallurgical improvements. The mode of deformation in these examples is local and anisotropic, therefore a fast heating method such as that produced by laser could enable the production of near net complex profiles.

2.5 Conclusion

The idea behind the new researches in producing local forms is to save energy, reduce cost and obtain more reliable products. For this purpose local heating has great importance. As the material is not fully heated, energy is saved and the cost is reduced as a result of the decrease in tooling investment. So the key idea in the production of local forms is the heating strategy used. In this point of view, the study of Merrygold where local heating is successfully realized by torch and induction coil is worth examining.

On the other hand, the laser processing applications show how much capable the laser is for local forming and/or heating purposes. The studies of Yanjin and Kovacevic are important in understanding the fact that, the laser is a very useful tool for sending the right amount energy in the right profile, which gives the user a great chance to control the process.

Combining these studies, it is possible to imagine manufacturing products just like in Figure 2.12 by utilizing the right type of laser, by applying the right amount of energy and heating strategy, by selecting the suitable materials and by making long-term researches on this idea.

CHAPTER 3

REVIEW OF NON-LINEAR FINITE ELEMENT ANALYSIS

3.1 Introduction

In order to analyze and comment further on the suggested process finite element analysis is utilized. Commercial finite element programs, MSC/Superform and MSC/Marc, are used for this purpose. These programs provide a graphical user interface program that allows the user to execute a finite element analysis process from start to finish (Figure 3.1).

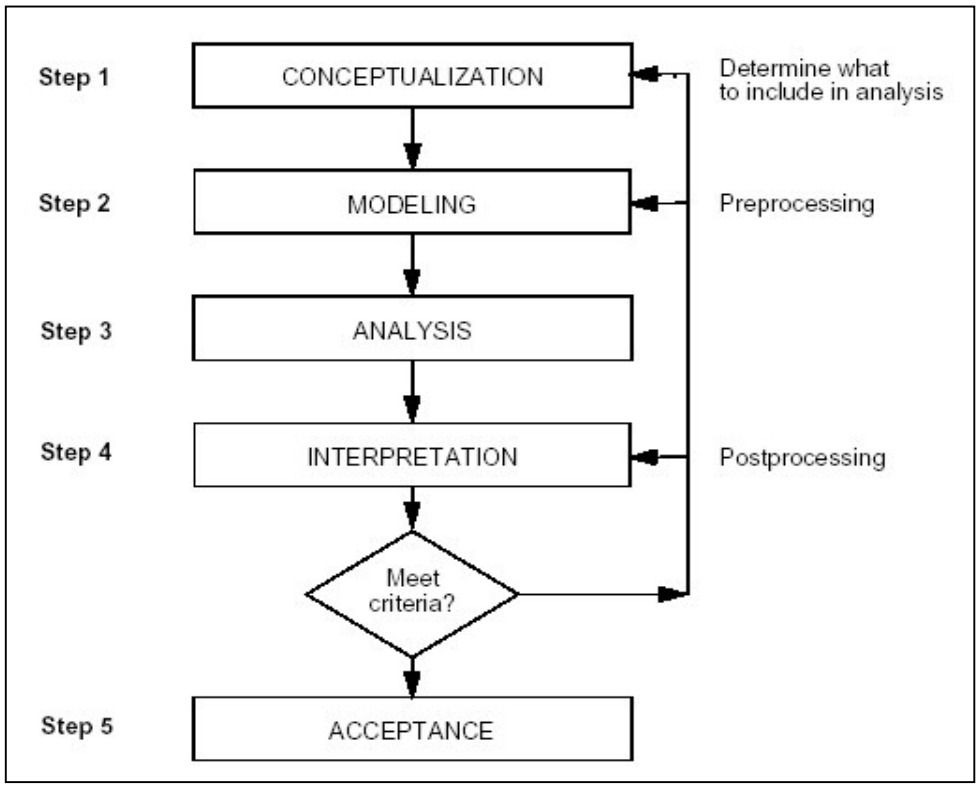

Figure 3.1 The Analysis Cycle.

A brief review of the theoretical fundamentals of the method and meanings of some of the important parameters will be given in this chapter. The results of the analyses will be later given in the sixth chapter.

3.2 Fundamental Steps for the Application of the Finite Element Method

Basic step-by-step procedure of the finite element method can be interpreted as follows regardless of the type of the problem, boundary conditions, or geometry [15]:

Step 1 *Idealization:* The whole continuum is divided into finite number of elements.

Step 2 *Discretization:* Infinite numbers of unknowns at infinite number of points are reduced to finite number of unknowns at finite number of points by the help of shape functions. These points are called nodes. The domains of the functions are called the finite elements.

Step 3 *Determination of Element Properties:* The relation between the unknown displacements and known forces is formed. The methods of deriving the stiffness matrices are:

- Direct Method
- Variational Method
- Weighted Residual Method

The relationship would be a linear function as in Equation (3.1) or a non-linear one as in Equation (3.2). It can be clearly understood that in linear equations structural stiffness is independent of the displacement whereas in a non-linear case stiffness is displacement dependent.

$$\{F\} = [k] \cdot \{u\} \tag{3.1}$$

$$\{F\} = [k\{u\}] \cdot \{u\} \tag{3.2}$$

Step 4 *Assembly of element stiffnesses to discretize the whole continuum:* This step can be interpreted as the construction of the geometry of the problem.

Step 5 *Introduction of boundary conditions:* Boundary conditions like force, displacement, etc. are applied to the related nodes.

Step 6 *Solution of the system of equations:* As a result of the previous steps a generally a large system of equations is obtained and solved by utilizing a computer.

Step 7 *Computation of strains and stresses:* After the displacements are calculated, the strains and finally the stresses are computed.

Step 8 *Interpretation and Verification:* The final results must always be verified in order to avoid a "garbage in garbage out" solution.

3.3 Basic Assumptions in Finite Element Method

The linearity assumption, with the basic equation given in Eq. 3.1, simplifies the solution of a problem dramatically. The linearity assumptions can be given as follows:

- Displacements are infinitesimally small
- Gradients of displacements are infinitesimally small
- Stresses depend linearly on strains
- Boundary conditions do not change during loading

Metal forming applications are regarded to be highly non-linear as the process includes large strains and displacements. The sources of non-linearity that lead to Eq. 3.2 can be given as:

- *Material Non-linearity*: Flow of material in plastic region, large strains. Metals exhibit an elasto-plastic behavior whereas rubber and polymers exhibit a non-linear elastic behavior.
- *Geometric nonlinearity*: Large rotation and displacement of the system with small strains.
- *Contact nonlinearity*: Contact of workpiece with other workpieces or tools, due to friction

3.4 Rigid Plastic and Elastic Plastic Approaches

Two different solution procedures are used for finite element analyses of metal forming problems, namely the rigid-plastic and elastic-plastic approaches. The rigid-plastic approach is favored in the analyses of metal forming problems because of the following reasons:

- This procedure is less time consuming because of the fact that the material does not require the consideration of the non-linear kinematics of the finite deformation.
- Rigid-plastic formulations are numerically rather robust and reliable.
- It is possible to formulate linear mixed tetrahedral elements, which allow easy automatic meshing in three-dimensional analysis.
- The computer implementation of rigid-plastic finite element code is simple.

Besides the advantages of this procedure, there are some serious disadvantages, which can be summarized as:

- Spring back and any other elastic based properties such as residual stresses cannot be analyzed by rigid-plastic material law as it neglects the elastic strains.
- Friction, which is always present between the tools and the workpiece in elastic regions of the workpiece especially in cold working applications, is not modeled correctly, because rigid-plastic models use a pseudo-elastic description of material regions, which are assumed to be rigid.
- Rigid-plastic material assumption cannot detect stress peaks, which occur at the transition between elastic and elasto-plastic material zones.
- If net shape forming processes are analyzed, the accuracy requirements of the analysis cannot be fulfilled usually.

Especially the friction parameter plays a critical role in this study, that's why the rigid-plastic material law is not suitable for the simulations. In addition to this, the cold regions can be modeled more accurate by using the elastic-plastic material approach.

3.5 General Solution Method

The typical element in a finite element problem can be modeled by a general spring element with the displacements and forces acting on the element as shown in Figure 3.2, where "U" stands for the displacements and "f " for the forces [16].

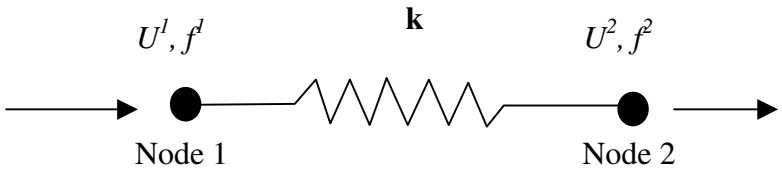

Figure 3.2 Demonstration of a typical element in a general solution.

It is known that, according to Hooke's law, when an elastic spring experiences an axial load the following equation holds;

Force = Spring Constant x Displacement

Then for this case,

$$f^1 = k \cdot (U^1 - U^2) \tag{3.3}$$

And for static equilibrium,

$$f^1 = f^2 \tag{3.4}$$

$$f^2 = -k \cdot (U^1 - U^2) \tag{3.5}$$

Finally the equation can be written in matrix form as,

$$\{ f \} = [k] \cdot \{ u \} \tag{3.6}$$

Force and displacement matrices can be interpreted as,

$$\{f\} = \begin{Bmatrix} f^1 \\ f^2 \end{Bmatrix} \text{ and } \{u\} = \begin{Bmatrix} u^1 \\ u^2 \end{Bmatrix} \quad \text{respectively,}$$

then the spring constant or the stiffness matrix in this general solution yields to,

$$[k] = \begin{bmatrix} k_{11} & k_{12} \\ k_{21} & k_{22} \end{bmatrix} = \begin{bmatrix} k & -k \\ -k & k \end{bmatrix} \tag{3.7}$$

The components of [K] are usually subscripted as k_{ij} to denote their location in the *i*th row and *j*th column of [K]. The square matrix [K] is known as the element stiffness matrix, the column vector { u } is the nodal displacement vector, and the column vector { f } is the nodal force vector for the element. For this simple example, it is possible to determine the exact values of the spring stiffness coefficients in the matrix [K], by using the Hooke's law. On the other hand, for more complex problems the stiffness coefficients are determined approximately by

using the assumed displacement functions. No matter how the coefficients are determined, the interpretation is the same; a typical stiffness coefficient k_{ij} is defined. For this example, it is the force required at node *i* to produce a unit deflection at node *j*. This definition holds, as only one force and one displacement exist at each node.

3.6 Interpolation Functions and Shape Functions

As it is stated above, it is necessary to use some "assumed displacement functions" in order to determine the stiffness coefficients. In this section, the method of defining those functions is given.

Consider a one-dimensional element of length *L*, as shown in Figure 3.3. The element has two nodes *i* and *j*, which are positioned at distances x_i and x_j from the origin. The general form of the interpolation function that defines the distribution of an unknown variable (displacement or something else) in the one-dimensional element is given as follows;

$$\phi = \alpha_1 + \alpha_2 \cdot x \tag{3.8}$$

by substituting the value of ϕ at each node into Equation 3.8 it can be derived that;

$$\alpha_1 = \frac{\phi_i \cdot x_j - \phi_j \cdot x_i}{x_j - x_i} = \frac{\phi_i \cdot x_j - \phi_j \cdot x_i}{L} \tag{3.9}$$

$$\alpha_2 = \frac{\phi_j - \phi_i}{x_j - x_i} = \frac{\phi_j - \phi_i}{L} \tag{3.10}$$

Again substituting these back into the Equation 3.8 gives,

$$\phi = \frac{\phi_i \cdot x_j - \phi_j \cdot x_i}{L} + \frac{\phi_j - \phi_i}{L} \cdot x \tag{3.11}$$

This equation can be rearranged further to get a result in terms of ϕ_i and ϕ_j as,

$$\phi = \frac{x_j - x}{L} \cdot \phi_i + \frac{x - x_i}{L} \cdot \phi_j \tag{3.12}$$

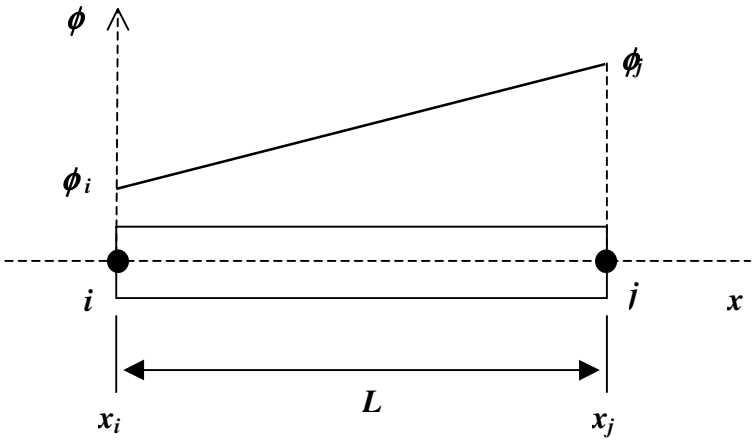

Figure 3.3 One-dimensional simple element

or

$$\phi = N_i \cdot \phi_i + N_j \cdot \phi_j = [\,N\,] \cdot \{\,\Phi\,\} \tag{3.13}$$

where N_i and N_j are called the shape functions. Each shape function is associated with one particular node, which is identified by the subscript. Note also that the shape functions are linear functions of *x* like the original interpolation function. It is always the case, that the interpolating functions and the shape functions are the polynomials of the same order.

3.7 Transformation of Local Coordinate System to the Global Coordinate System

During the application of finite element method it will be seen that, many terms need to be calculated by the integration of some function of the shape functions. In fact, this is not a difficult task but it is further simplified by the introduction of local coordinate systems, which belong to a particular finite element. After the required calculations the system should be converted to the main global coordinate system. This operation is done by assigning a transformation matrix (Figure 3.4). The "~" sign here denotes the local variables.

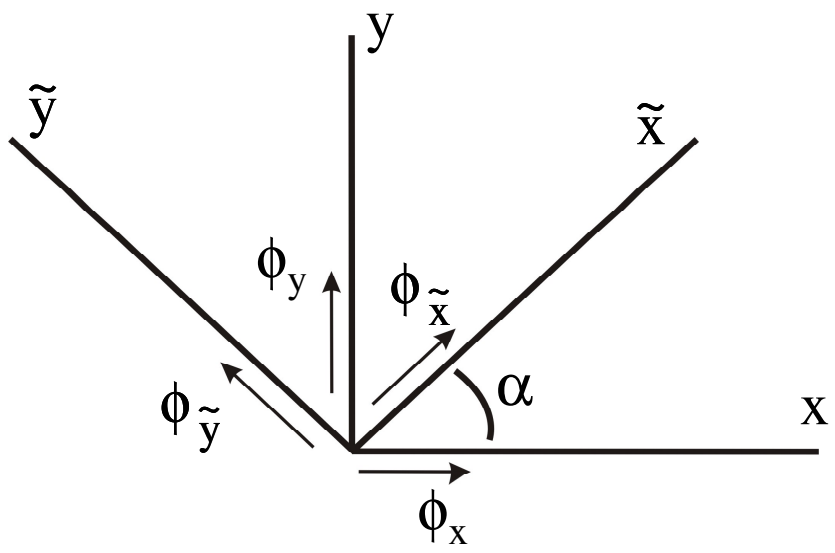

Figure 3.4 Transformation to the Global Coordinate System

By applying simple trigonometry, one can state that;

$$\phi_y = \phi_{\tilde{y}} \cdot \cos\alpha \tag{3.14}$$

$$\phi_x = \phi_{\tilde{x}} \cdot \cos\alpha \tag{3.15}$$

It is possible to express the transformation operation in matrix form as,

$$\begin{Bmatrix} \phi_x^1 \\ \phi_y^1 \\ \phi_x^2 \\ \phi_y^2 \end{Bmatrix} = \begin{vmatrix} \cos\alpha & 0 \\ \sin\alpha & 0 \\ 0 & \cos\alpha \\ 0 & \sin\alpha \end{vmatrix} \cdot \begin{Bmatrix} \phi_{\tilde{x}}^1 \\ \phi_{\tilde{y}}^1 \end{Bmatrix} \tag{3.16}$$

In general form, the transformation matrix, which is denoted as *A* matrix is included in the coordinate conversion operation step as in Eq. 3.17.

$$\{\phi\} = [A]^T \cdot \{\tilde{\phi}\} \tag{3.17}$$

then it is possible to rewrite Eq. 3.1 as,

$$\{\phi\} = [A]^T \cdot [\tilde{K}] \cdot \{\tilde{U}\} \tag{3.18}$$

further simplification is done by rearranging the position term just as the variable ϕ term as,

$$\{\tilde{U}\} = [A] \,.\, \{U\} \tag{3.19}$$

then combining the Eq. 3.18 and 3.19 it is possible to obtain,

$$\{\phi\} = [A]^T \cdot [\tilde{K}] \cdot [A] \cdot \{U\} \tag{3.20}$$

and finally the global stiffness matrix can be expressed as,

$$\{K\} = [A]^T \cdot [\tilde{K}] \cdot [A] \tag{3.21}$$

3.8 General Elastic-Plastic Finite Element Solution by Updated Lagrange Method

The updated Lagrange method is in fact the conventional Lagrange method in which the reference frame is updated at the end of each increment in the solution

procedure. The element stiffness is assembled in the current configuration of the element, and the stress and strain output are given with respect to the coordinate system in the updated configuration of the element. The updated Lagrangian approach is useful in:

- Analysis of shell and beam structures in which rotations are large so that the nonlinear terms in the curvature expressions may no longer be neglected.
- Large strain plasticity analysis, for calculations which the plastic deformations cannot be assumed to be infinitesimal.

The Lagrange method is used to obtain the equations of equilibrium for an elastic-plastic problem, whereas the Eulerian method is utilized in case of a rigid plastic problem. As previously stated the metal forming problems are usually modeled to be elastic-plastic and a general finite element solution by updated Lagrange method will be given accordingly in this section.

The starting point is the equation if equilibrium, which is, neglecting the mass forces and inertia effects can be given as,

$$\frac{\partial \sigma_{ji}}{\partial x_j} + q_i = 0 \tag{3.22}$$

This equation of equilibrium is valid for the body in the current or deformed configuration, which is denoted by using the small letters. Later in this section, the capital letters will be used for the initial or undeformed position. Here, the σ term stands for the true or Cauchy stress tensor and q for the body forces. The equilibrium equations are the strong form of the principle of virtual work. Integrating over the deformed configuration taking the external forces (t) into account gives out,

$$\int_V \sigma \cdot \frac{\partial \delta u}{\partial x} \cdot dv = \int_V q \cdot \delta u \cdot dv + \int_S t \cdot \delta u \cdot ds \tag{3.23}$$

Furthermore, it is known that it is possible to write the equation of equilibrium in the deformed configuration by the help of the Jacobian of the deformation if the undeformed configuration is known. Jacobian of the deformation is given as,

$$J = \frac{dv}{dV} = \det\left(\frac{\partial x}{\partial \boldsymbol{X}}\right) = \det(\boldsymbol{F}) \tag{3.24}$$

where F term stands for the deformation gradient tensor. By applying the Jacobian in Eq. 3.23 one can get,

$$\int_V J \cdot \sigma \cdot \frac{\partial \delta u}{\partial \boldsymbol{X}} \cdot d\boldsymbol{V} = \int_V \boldsymbol{Q} \cdot \delta u \cdot d\boldsymbol{V} + \int_S \boldsymbol{T} \cdot \delta u \cdot d\boldsymbol{S} \tag{3.25}$$

It is possible also to relate the original (undeformed) area to the current force, which defines the first Piola-Kirchhoff stress tensor. This unsymmetrical tensor can be interpreted as engineering stress definition. To define a symmetric stress tensor with respect to the original configuration, second Piola-Kirchhoff stress tensor (S) is defined through a pseudo force vector as,

$$J \cdot \sigma_{ij} = F_{ij}^{T} \cdot S_{ij} \cdot F_{ij} \tag{3.26}$$

The work conjugate of the second Piola-Kirchhoff stress tensor is defined as the Green-Lagrangian strain tensor, which is given as,

$$E_{ij} = \frac{1}{2}\left(F_{ij}^{T} \cdot F_{ij} - I\right) \tag{3.27}$$

the variation in the Green-Lagrangian strain tensor is then,

$$\delta E_{ij} = \frac{1}{2}\left(F_{mi}\frac{\partial \delta u_m}{\partial X_j} + \frac{\partial \delta u_m}{\partial X_i}F_{mj}\right) \tag{3.28}$$

finally, the principle of virtual work integrated over the undeformed configuration can be derived as,

$$\int_V \boldsymbol{S}^T \cdot \delta \boldsymbol{E} \cdot dV = \int_V \boldsymbol{Q} \cdot \delta u \cdot dV + \int_S \boldsymbol{T} \cdot \delta u \cdot d\boldsymbol{S} \tag{3.29}$$

The rate of virtual work can be found by just differentiating Eq. 3.29 with respect to time,

$$\int_V \left[\dot{S}_{ij} \cdot \delta E_{ij} + S_{ij} \cdot \frac{\partial v_k}{\partial X_i} \cdot \frac{\partial \delta u_k}{\partial X_j} \right] dV = \int_V \dot{Q}_i \cdot \delta u_i \cdot dV + \int_S \dot{T}_i \cdot \delta u_i \cdot dS \tag{3.30}$$

Although it is possible to derive theoretical constitutive equations of the type given in Eq. (3.30) for most materials, it is often more suitable to specify the equations with reference to the current state. The desired formulation can be obtained by taking Eq. (3.30) to the reference state as current state. Defining *D* as the deformation gradient, the conversion can be written as,

$$\delta E_{ij} = \delta D_{ij} \quad , \quad F_{ij} = \delta_{ij} \quad , \quad \frac{\partial}{\partial X_i} = \frac{\partial}{\partial x_i} \quad , \quad S_{ij} = \sigma_{ij} \tag{3.31}$$

then Eq. 3.30 turns to,

$$\int_V \left[\dot{\sigma}_{ij}^T \cdot \delta D_{ij} + \sigma_{ij} \cdot \frac{\partial v_k}{\partial x_i} \cdot \frac{\partial \delta u_k}{\partial x_j} \right] dv = \int_V \dot{b}_i \cdot \delta u_i \cdot dv + \int_S \dot{t}_i \cdot \delta u_i \cdot ds \tag{3.32}$$

In this equation, $\dot{\sigma}_{ij}^T$ is the Truesdell rate of Cauchy stress tensor, which can be obtained from the usual material rate of Cauchy stress tensor by differentiation of

$$\dot{\sigma}_{ij} = \dot{J}^{-1} F_{ik} \dot{S}_{kl} F_{jl} + J^{-1} \dot{F}_{ik} S_{kl} F_{jl} + J^{-1} F_{ik} S_{kl} \dot{F}_{jl} - \dot{J} J^{-2} F_{ik} S_{kl} F_{jl} \tag{3.33}$$

If current state is taken as the reference state, it follows that

$$\dot{\sigma}_{ij} = \dot{\sigma}_{ij}^T + \frac{\partial v_i}{\partial x_k} \cdot \sigma_{kj} + \sigma_{ik} \cdot \frac{\partial v_j}{\partial x_k} - \sigma_{ij} \cdot \frac{\partial v_k}{\partial x_k} \tag{3.34}$$

Truesdell rate of Cauchy stress is materially objective, which means that if rigid rotation is imposed on the material, the Trusdell rate vanishes, whereas the usual material rate does not vanish. The constitutive equations may well be formulated in terms of the Truesdell rate of Cauchy stress tensor. It may be written as

$$\dot{\sigma}_{ij}^{T} = L_{ijkl}(\sigma_{mn})D_{kl} \tag{3.35}$$

Here, a final relation must be given between the moduli L_{ijkl} and the classical elastic-plastic moduli, which can be given as,

$$L_{ijkl}^{e-p} = 2G \cdot \left[\delta_{ik} \cdot \delta_{jl} + \frac{\lambda}{2G} \cdot \delta_{ij} \cdot \delta_{kl} - \frac{3}{2} \cdot \frac{\sigma'_{ij} \cdot \sigma'_{kl}}{\sigma_o^{\,2}} \right] \tag{3.36}$$

These moduli supply the relation between the Jaumann rate of Cauchy stress tensor and the deformation rate

$$\dot{\sigma}_{ij}^{J} = L_{ijkl}^{e-p} D_{kl} \tag{3.37}$$

The Jaumann rate of Cauchy stress tensor is related to the material rate of Cauchy stress tensor with the equation

$$\ddot{\sigma}_{ij}^{J} = \dot{\sigma}_{ij} - \omega_{ik} \cdot \sigma_{kj} - \sigma_{ik} \cdot \omega_{jk} \tag{3.38}$$

where the spin tensor ω_{ij} is defined by,

$$\omega_{ij} = \frac{1}{2}\left(\frac{\partial v_i}{\partial x_j} - \frac{\partial v_j}{\partial x_i} \right) \tag{3.39}$$

The Jaumann rate of Cauchy stress is the rate of change of the Cauchy stress in a corotational system. The material rate of Cauchy stress can be eliminated from Eq. 3.34 and Eq. 3.38 by using Eq. 3.39, which yields the relation,

$$\dot{\sigma}_{ij}^{T} = \sigma_{ij}^{J} - D_{ik} \cdot \sigma_{kj} - \sigma_{ik} \cdot D_{kj} + \sigma_{ij} \cdot D_{kk} \tag{3.40}$$

Thus the relation between the large strain moduli and the classical elastic-plastic moduli can be easily formed as follows,

$$L_{ijkl} = L_{ijkl}^{e-p} - \delta_{il} \cdot \sigma_{kj} - \sigma_{il} \cdot \delta_{kj} + \sigma_{ij} \cdot \delta_{kl} \tag{3.41}$$

Note that the last term in Eq. 3.41 does not satisfy the usual symmetry relation. This is not relevant for material plasticity problems since the deformations are approximately incompressible. Hence, Eq. 3.41 may be approximated by,

$$L_{ijkl} \approx L_{ijkl}^{e-p} - \delta_{il} \cdot \sigma_{kj} - \sigma_{il} \cdot \delta_{kj} \tag{3.42}$$

Spatial discretization leads to the overall non-linear stiffness equations of the form

$$[K\{U\}] \cdot \{\Delta U\} = \{\Delta F\} \tag{3.43}$$

3.9 Numerical Solution Procedures for the Equations

The numerical methods must be utilized in order to solve the related equations of finite element applications of metal forming processes. This is mainly due to material, geometric and contact nonlinearities.

The most frequently used methods are; Euler method, self-correcting Euler method, Runga-Kutta method, direct iteration method, the Newton-Raphson method, modified Newton-Raphson method, and quasi Newton-Raphson method (Figure 3.5). Newton-Raphson method is used for the simulations in this study (Figure 3.6). Newton-Raphson method can be formulated by,

$$\left[k_t\left\{U^{i-1}\right\}\right] \cdot \left\{\Delta U^i\right\} = \left\{R\left\{U^{i-1}\right\}\right\} \tag{3.44}$$

The initial guess plays an important role in the Newton-Raphson method. A “bad” initial guess can even cause solution to divergence, so the stability of the solution is dependent on the initial guess. The Newton-Raphson method has quadratic convergence characteristics, which means that the relative error decreases quadratically in following iterations.

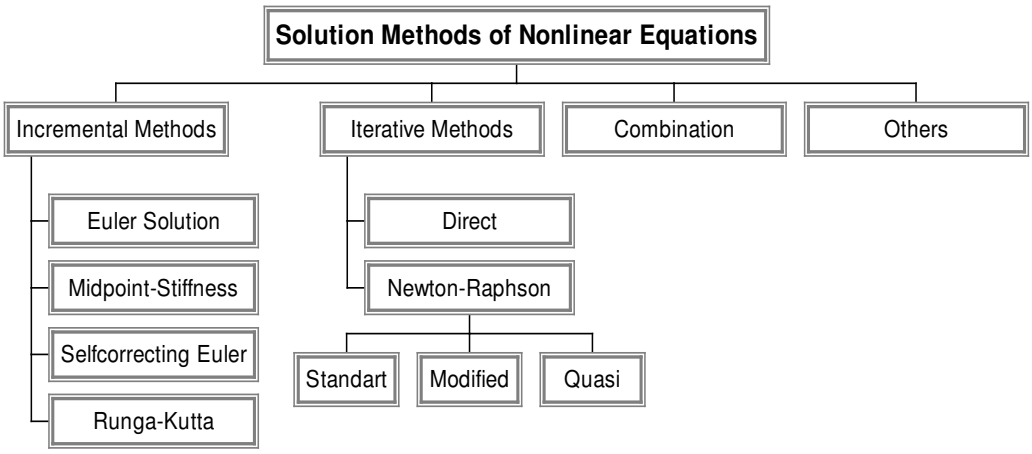

Figure 3.5 Solution methods of nonlinear equations.

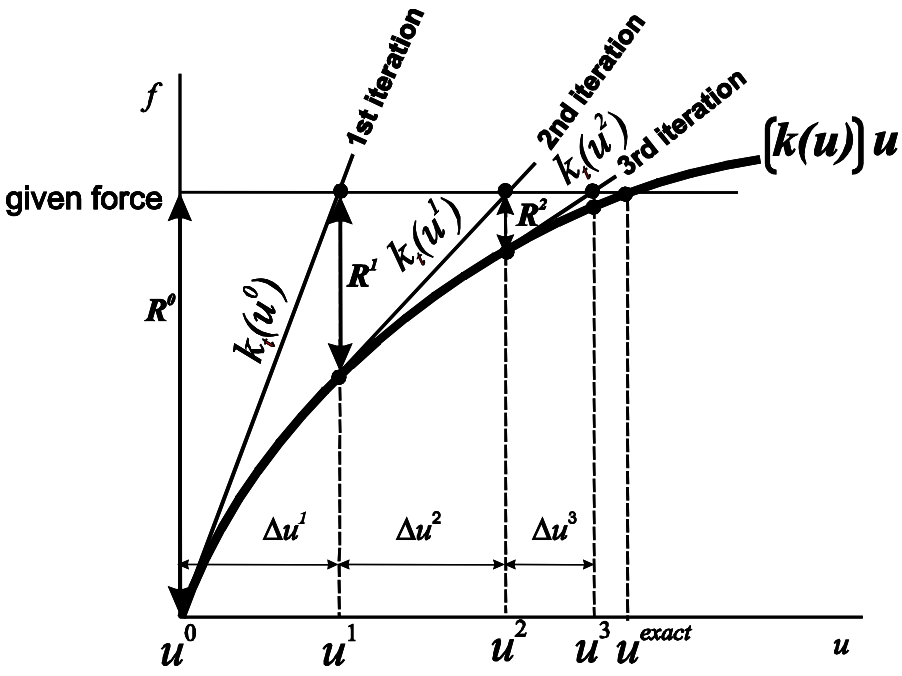

Figure 3.6 Newton-Raphson solution procedure

3.10 Convergence Criteria for the Solution

It is possible to define the convergence criteria in MSC Marc as the absolute values, relative values or both. The ratio of maximum residual force to the maximum

reaction force is defined to be the convergence criteria as it is safer than defining an absolute value which also requires the minimization of the magnitude residual loads. The residual loads and displacements are controlled separately in order to ensure convergence as [17],

- Residuals:

Relative residual checking

$$\frac{\left\| F_{residual} \right\|_\infty}{\left\| F_{resident} \right\|_\infty} < Tolerance \tag{3.45}$$

Absolute residual checking

$$\left\| F_{residual} \right\|_\infty < Tolerance \tag{3.46}$$

Here, the tolerance parameter is defined according to the level of accuracy required. Note also that, the $F_{residual}$ term corresponds to the R terms in Figure 3.6 and $F_{resident}$ defines the total applied force.

- Displacements:

Relative displacement checking

$$\frac{\left\| \delta u \right\|_\infty}{\left\| du \right\|_\infty} < Tolerance \tag{3.47}$$

Absolute displacement checking

$$\left\| \delta u \right\|_\infty < Tolerance \tag{3.48}$$

Here d_u denotes the displacement increment vector, and δu, the displacement iteration vector. Convergence is satisfied if the maximum displacement of the last iteration compared to the actual displacement change of the increment is smaller than the given relative or absolute displacement tolerance value. The value of the convergence criterion has an effect on the accuracy of the solution. When the convergence criterion is tighter, the solution becomes more accurate but the calculation time increases. The user has to make a clear assessment whether the result obtained from the simulation worth the time spend.

3.11 Modeling of Friction in FEM

Friction is in fact a complex physical phenomenon, which is still studied and involves many surface characteristics such as, roughness, temperature, normal stress and relative velocity. Because of the complexity of the case, friction is simplified to two idealistic models; namely Coulomb friction model and shear friction model.

- Coulomb Friction Model: This model is the most popular one, which is used for many applications with the exception of bulk forming such as forming. Coulomb fiction model is applied as in Eq. 3.49:

$$\sigma_{fr} \leq -\mu \cdot \sigma_n \cdot t \tag{3.49}$$

Where

σ_{fr} is the tangential (friction) stress

μ is the coefficient of friction ($0 \leq \mu \leq 0.577$)

σ_n is the normal stress

t is the tangential vector in the direction of the relative velocity

Usually, neutral lines develop in contact problems, which means that along a contact surface, the material flows in one direction in part of the surface and in the opposite direction in another part of the surface. In case of neutral points on the contact surface such as in rolling, the friction stresses may result instabilities due to back and forth of the friction force direction. To improve the stability, the friction terms are modified as shown in Figure 3.7. Because of the smoothed behavior of the modified friction law, anode in contact has always some slipping.

The Coulomb friction model often does not correlate well with experimental observations when the normal force/stress becomes large. If the normal stress becomes large, the Coulomb model might predict that the frictional shear stresses increase to a level that can exceed the flow stress or the failure stress of the material. As this is not physically possible, the choices are either to have a nonlinear coefficient of friction or to use the cohesive, shear based friction model.

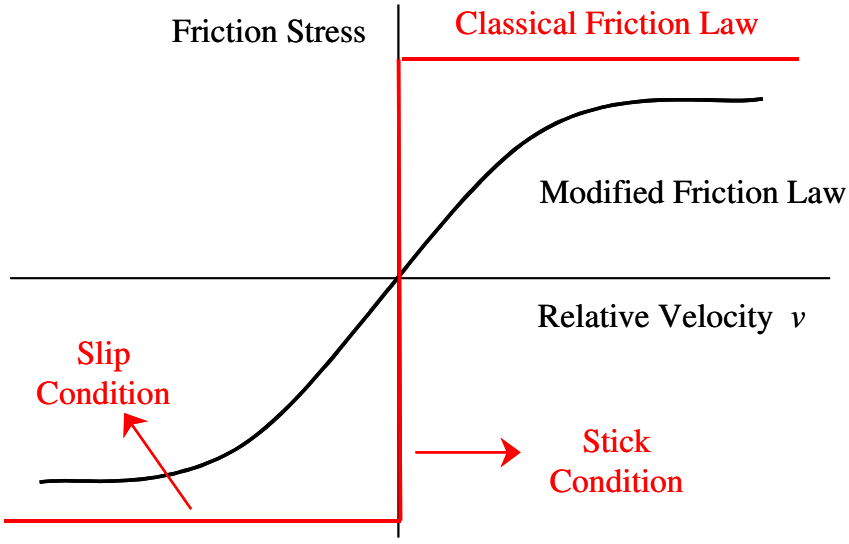

Figure 3.7 Modified friction modeling

- Shear Friction Model:

Frictional stress is a fraction of the equivalent stress in the material according to the shear friction model;

$$\sigma_{fr} \leq -m\frac{\sigma_f}{\sqrt{3}} \tag{3.50}$$

where,

m is the shear factor ($0 \leq m \leq 1$)

Shear friction model is generally used for the friction modeling in hot regions. Both approaches are suitable for simulating the subject process. But Coulomb friction model is selected.

3.12 Modeling of Thermo-Mechanical Analyses

It is possible to say that, finite element method permit a common Discretization for the thermal and mechanical analysis. The schematic structure of the calculation steps can be given as (Figure 3.8) [17]:

1. Velocity field calculation
2. Mesh Coordinates are updated
3. Temperature distribution calculation
4. Updating material properties with respect to temperature

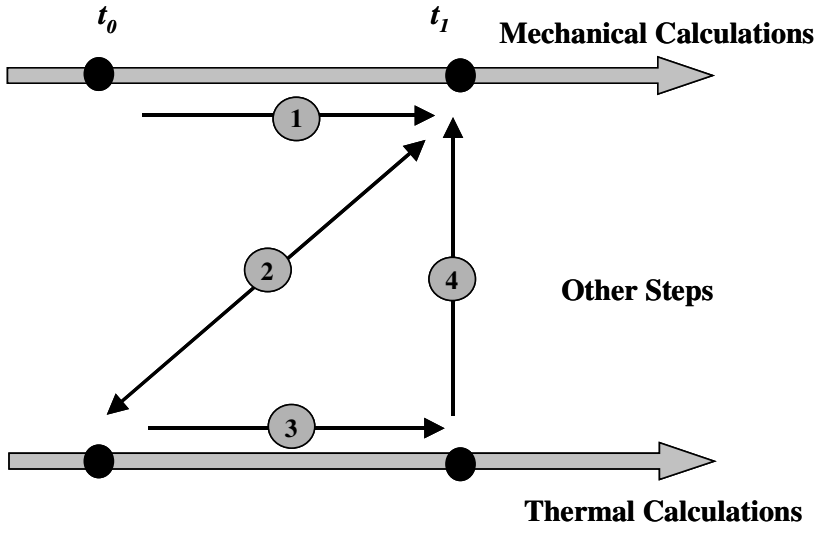

Figure 3.8 Calculation procedure for a loose coupled thermo-mechanical analysis

Thermo-mechanically coupled analyses should be carried out if the thermal stresses and temperature dependency of the material are considered to be critical for the process. The finite element modeling of the process should be a coupled one if the following conditions are present:

1. The body undergoes large deformations such that there is a change in the boundary conditions associated with the heat transfer problem.

2. Deformation converts mechanical work into heat through an irreversible process, which is large relative to other heat sources.

In any case, temperate distribution and as a result thermal stresses have important effects on the deformation of the body and the material properties.

CHAPTER 4

EXPERIMENTAL STUDIES

4.1 Introduction

In this chapter, the experimental setup used, specifications of the workpieces, the experimental procedure, and results of the experiments will be explained in detail. The experimental setup section will cover the laser source, the press, the robot arm, and the pyrometer. Material selection and the dimensional properties will be given in the specifications of the workpieces section. Laser heating and free forming applications will be explained step by step in the experimental procedure section and finally the interpretation of the results together with the pitfalls of the application will form the last section.

4.2 Experimental Setup

4.2.1 The Laser Source

Throughout the process Nd:YAG type of laser, which is mainly used in cutting, welding, drilling and hardening applications, is used to heat up the workpieces. Characteristic for the whole range is its flexibility with respect to the adaptation to the different applications.

Laser material for the Nd:YAG laser is 1% Neodymium (Nd) doped into Yttrium Aluminum Garnet (YAG). Pump sources are Xe or Kr lamps or diodes. Laser wavelength is 1064 nm. The main reason in selecting the Nd:YAG type of laser is

the relatively higher absorption characteristics for iron and steel (Figure 4.1). The absorption ratio is around 30% for iron and rather higher for steel. In addition to these average values the optical thickness of the materials should be taken into account

In the basic version, the optic system is integrated into the cubicle for utilization with fiber optic systems. As an option, the optics system can be freely mounted, which is in fact the case in the experimental procedure of this study. This type of usage is suitable for direct and indirect fiber optic beam guidance. For both beam guidance an extensive range of accessories is available.

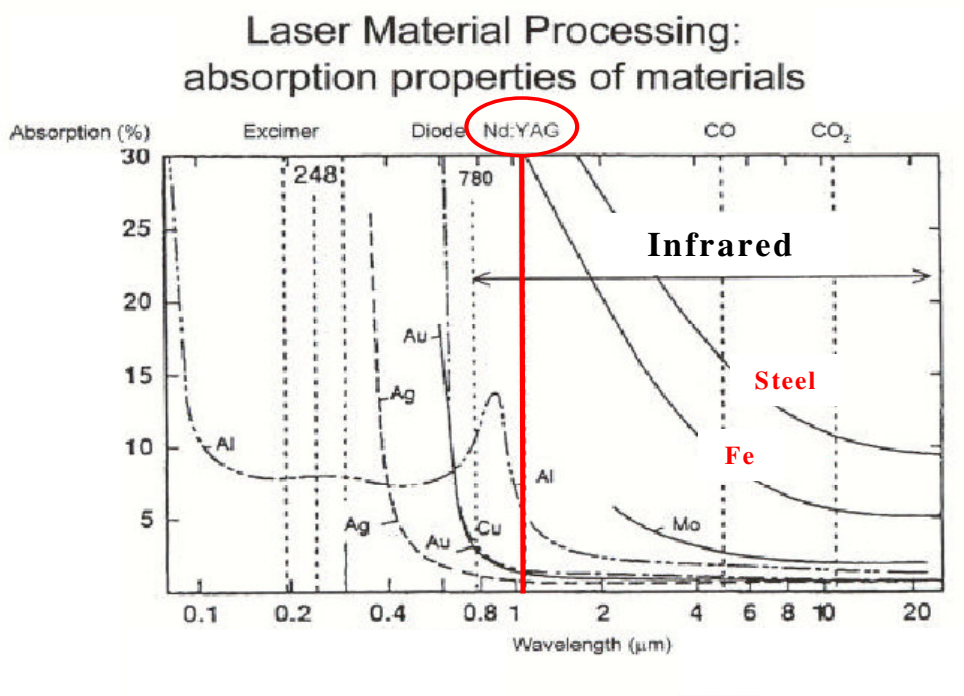

Figure 4.1 Absorption properties of materials with respect to different wavelengths of lasers

Power supply and control systems are housed in a completely closed cubicle (Figure 4.2a). The only access, both for operation and servicing, is from the front, so that the laser source can be placed against a wall or in a recess, which provides a space saving arrangement. The internal heat is removed with the cooling water and therefore is no burden on the surrounding [18].

The Nd:YAG laser is carried by using the fiberoptic cables to the press where the forming process takes place and attached to the five axes robot arm in order to perform the required heating profiles (Figure 4.2b).

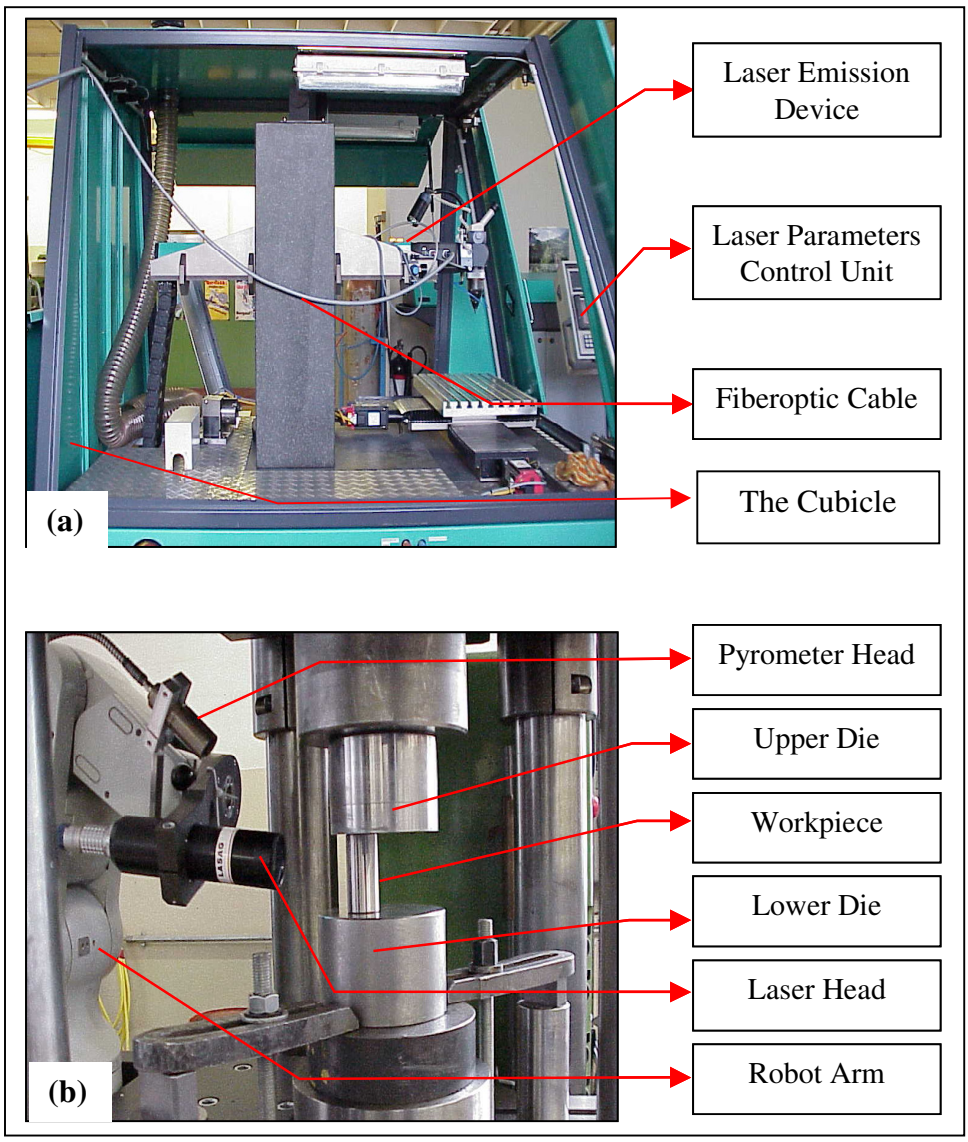

Figure 4.2 Main Parts of the laser heating setup.

4.2.2 The Press

The press used throughout the forming experiments is a Bucher-Guyer type LS 150 press, which is a hydraulic one with the specifications given in Table 4.1. The press was designed originally to be utilized for plastic materials' processing.

Hydraulic presses move in response to the oil pressure. This property makes them move slower, more massive and more costly to operate, when compared to the mechanical presses. On the other hand, they usually are much more flexible and have greater capacity of load. Since motion is in response to pressure and flow of the drive fluids, they can be programmed to have different strokes for different operations and different speeds within a stroke.

Table 4.1 Specifications of the Bucher-Guyer type LS 150 hydraulic press.

Total Press Force	150 Tons
Total Displacement	450 mm.
Distance Between Upper and Lower Pressing Surfaces	640 – 790 mm
Maximum Speed	10 mm/s
Minimum Speed	3.7 mm/s
Maximum Removal Punch Force	10 Tons
Maximum Reverse Direction Force	20 Tons

4.2.3 Pyrometer

One of most important problems about the heating experiments is related with the difficulties in collecting the data. The two-color pyrometer Infratherm IGAQ 10-LO that is a completely digital no contact temperature measurement instrument with fiber optics for medium and high range temperatures. It is equipped with a built-in display, a linear analog current output and a serial digital interface (Figure 4.2 and Figure 4.3). The processing of measured data works fully digital and thus is very exact. Linearizing and ambient temperature compensation are calculated correctly to the degree. Accuracy and repeatability are important properties of such devices, which are 0.5% and 0.3% of measured quantity in $^{o}C \pm 1^{o}C$ respectively, for this case.The pyrometer used throughout the experiments has a range of $349^{o}C$ to $1349^{o}C$. On the other hand for laser heating, as the energy is applied to a very small area, the temperature changes suddenly and to high temperatures around the melting point, which is around $1600^{o}C$ for the Titanium alloy. But, as the upper limit of the

pyrometer is not enough, the collected temperature data is used in finite element method simulations based on extrapolations after the upper temperature limit.

In order to take the heating data accurately during the process, the pyrometer and the laser head are arranged such that the guide laser spots are focused on each other. This allows the pyrometer to read the temperature data just at the laser heating area. The temperature data collected is the most important criterion in finite element method simulations.

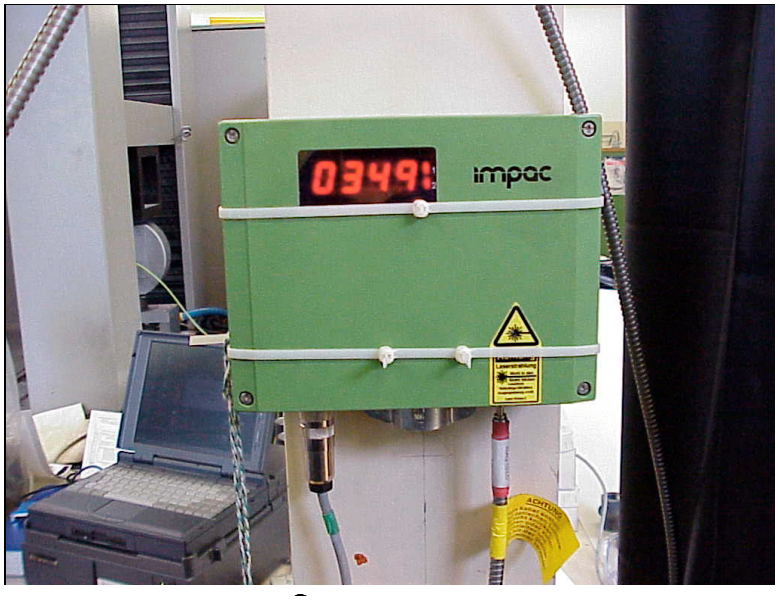

Figure 4.3 Display unit of the pyrometer

4.2.4 Five-Axes Robot Arm

The Nd:YAG laser is carried to the press where the forming process takes place as previously explained by using the fiberoptic cables. The Laser head together with the pyrometer is attached on a five-axes Mitsubishi industrial robot arm, which is programmed to perform the heating profiles (Figure 4.2 and Figure 4.4). The computer program is written by using a special computer language, which is quite similar to the case for CNC machines. The programs are created in a laptop computer and are loaded to the main control unit. The execution of the heating program is realized after giving the robot arm speed as another input. The remote

control unit is used to input the positions by “teaching” option if necessary and to interfere the motion in case of emergency.

The main body of the computer program, which controls the robot arm motion, is written in order to obtain a heating pattern that is composed of concentric circles. The “circles” are in fact collections of points, which lie on an n-gonal shape. The value of “n” should be kept as high as possible to simulate a perfect circle. On the other hand, each point on the extrapolating n-gonal causes extra time for calculating the position in three space variables (x,y,z). Furthermore, if the points to be visited are increased the speed of the robot arm decreases as each point means an extra “stop and start” in the motion (further explained in Section 4.4 & Figure 4.10).

The number of cycles, speed of the robot arm and the number of the inner circles can be modified on the computer program, according to the required heating procedure.

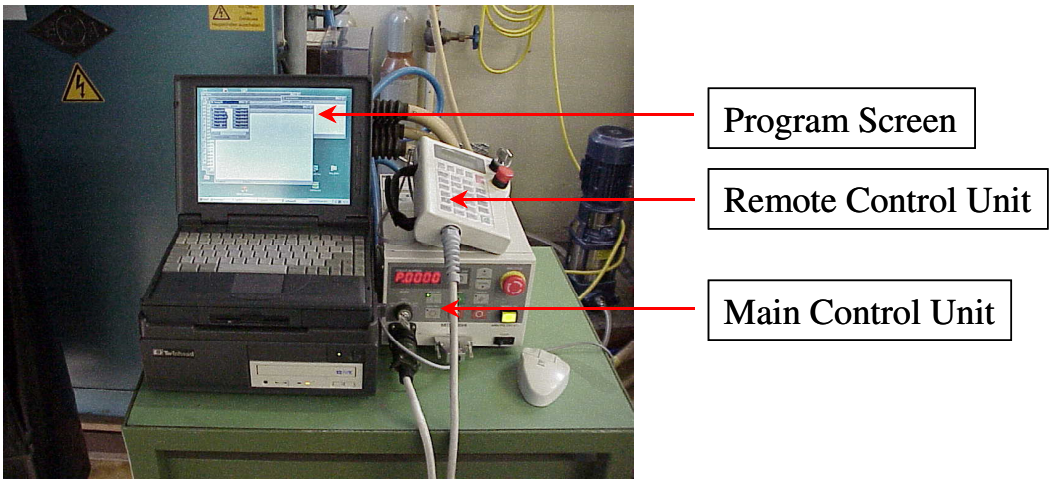

Figure 4.4 Robot arm control units.

An example to the robot arm computer program together with its explanations is given in the next page (Figure 4.5). The heating profile is composed of four concentric circles (largest one having a radius of 4 mm), which are in fact polygons with ninty edges (see Section 4.4). This structure is executed four times (cycles) to complete the heating profile.

```
10 'Interpolation 3D circle
20 '
30 DEF POS P1,P101,P361 'Input positions are given by teaching
40 'FOR TOOL DEFINITION
50 DEF FLOAT MPARTR,I,M,K,TETA,H,C 'Program variables are given
60 DIM POINT_MATRIX(4,91) '2D Point matrix of the visiting points
70 DIM HR(4) '1D matrix to store the radii of 4 concentric circles
80 '
90 P101=(0,0,0,0,0,0)
100 TOOL P101
110 '
120 FOR M=0 to 3 'Calculation of 4 concentric heating circles
130 HR(M+1)=0
140 HR(M+1)=4-(M)*0.5
150 NEXT M
160 MPARTR=15 'Radius of the workpiece is given as an input
170 '
180 'LI=10 'Distance of tool to workpiece surface
190 '
200 FOR I=0 TO 90 'Construction of the point matrix
210 POINT_MATRIX(1,I+1)=P1
220 POINT_MATRIX(2,I+1)=P1
230 POINT_MATRIX(3,I+1)=P1
240 POINT_MATRIX(4,I+1)=P1
250 NEXT I
260 '
270 FOR M=0 TO 3 'Calculation of the positions of the points
280 FOR I=0 TO 90
290 '
300 TETA=I*22/7/180*4
310 POINT_MATRIX(M+1,I+1).Z=P1.Z+HR(M+1)*COS(TETA)
320 POINT_MATRIX(M+1,I+1).Y=P1.Y+HR(M+1)*SIN(TETA)
330 H=SQR(MPARTR^2-(HR(M+1))^2*(SIN(TETA))^2)
340 POINT_MATRIX(M+1,I+1).X=P1.X-H+MPARTR
350 '
360 NEXT I
370 NEXT M
380 '
390 MOV P1 'Commands to realize the motion
400 DLY 1
410 '
420 FOR K=0 TO 14 'Execute the motion 15 times
430 FOR M=0 TO 3 'Define the heating circle
440 FOR I=0 TO 90 'Define the points on the heating circle
450 MOV POINT_MATRIX(M+1,I+1)
460 NEXT I
470 NEXT M
480 NEXT K
490 '
500 P361=POINT_MATRIX(4,91)
510 P361.X=POINT_MATRIX(4,91).X-20'Remove the laser head 20mm back
520 MOV P361
530 END
540
```

Figure 4.5 Robot arm computer program example

4.3 Material Selection

Three different materials are used throughout the experiments in order to investigate the effects of different physical properties on the process. Mainly the availability, thermal and mechanical properties of the materials are important factors in this selection. The materials are 16MnCr5, X5CrNi18_9, and Ti6Al4V.

16MnCr5 is an alloyed case hardening steel which is used in manufacturing highly stressed wear parts with medium cross sections for automotive and mechanical engineering, e.g. camshafts, bushings, connecting rods, gears, etc. Its conductivity, which is an important factor in local heating, is high when compared to the other two materials (Figure 4.7)

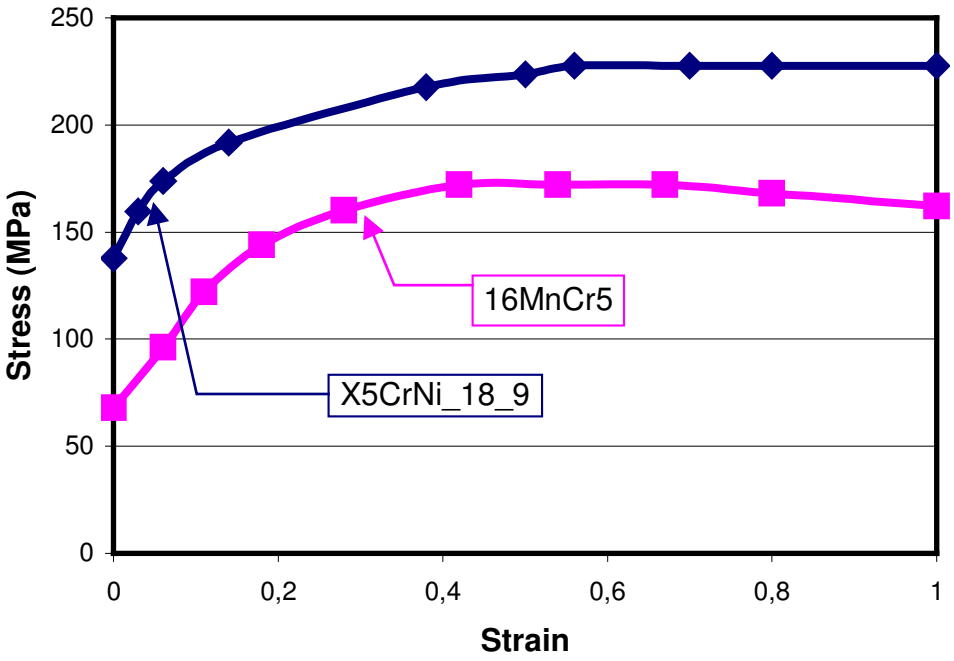

Figure 4.6 The flow curves of X5CrNi18_9 and 16MnCr5 at 1000°C and 8 s^{-1}

X5CrNi18_9 is a type of austenitic stainless steel with the property of high ductility. The flow curves of X5CrNi18_9 and 16MnCr5 are given in Figure 4.6. It is observed that approximately 40% higher stress values are required in order the stainless steel to yield. It resists rusting from all atmospheric sources and is

recommended for use in connection with foodstuff, sterilizing, most of organic chemicals and dyestuff.

Ti6Al4V is one of the most frequently used Titanium alloys in industry. It is an alpha-beta Titanium alloy, which means that it contains both alpha and beta phases at room temperature. The alpha phase is similar to that of unalloyed titanium but is strengthened by alpha stabilizing additions (e.g., aluminum). The beta phase is the high-temperature phase of titanium but is stabilized to room temperature by sufficient quantities of beta stabilizing elements such as vanadium, molybdenum, iron, or chromium. In addition to strengthening of titanium by the alloying additions, alpha-beta alloys may be further strengthened by heat treatment. The alpha-beta alloys have good strength at room temperature and for short times at elevated temperature. An example to the flow curve of Ti6Al4V is given in Figure 4.7. Ti6Al4V is available in all mill product forms as well as castings and powder metallurgy forms. One of the most important properties of this Titanium alloy is its low thermal conductivity, which makes it very suitable for local heating applications (Figure 4.8).

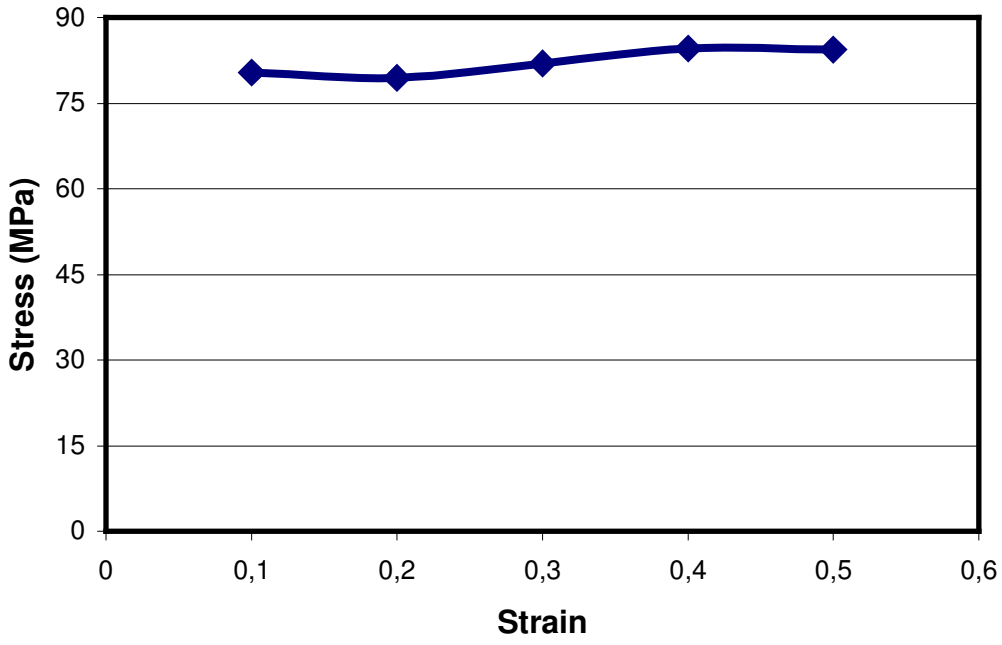

Figure 4.7 The flow curve of Ti6Al4V at 100^{o}C and 10s^{-1}

In thermal properties side, thermal conductivity and thermal diffusivity are taken into account in order to decide the availability of the material for local heating. Thermal diffusivity is defined as the material's capability of conducting the thermal energy relative to its capability of storing the energy. This property is formulated as (Equation 4.1) the ratio of thermal conductivity (capability of conduction of thermal energy) to the product of specific heat at constant pressure and mass density of the material (capability of storing thermal energy). The comparison of the thermal diffusivities of these three materials is given in Figure 4.9.

$$\frac{k}{\rho c} \equiv \frac{\text{Capability of Conduction of Thermal Energy}}{\text{Capability of Storing Thermal Energy}} \tag{4.1}$$

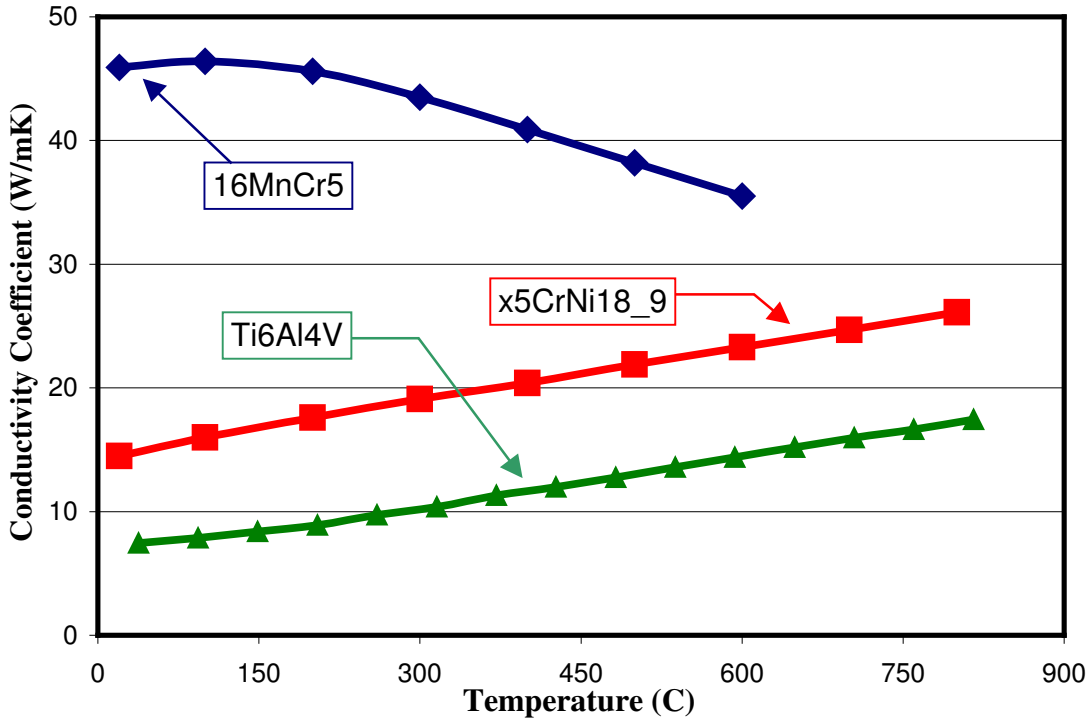

Figure 4.8 Conductivity values of 16MnCr5, X5CrNi18_9 (MARC material database) and Ti6Al4V [19].

In this study, as previously explained the local heating part of the experiment can be regarded as a transient process as the workpiece is not allowed to reach the steady state, therefore the thermal diffusivity of the material has an important role in heat

propagation. Thermal conduction is usually taken into account for steady state applications.

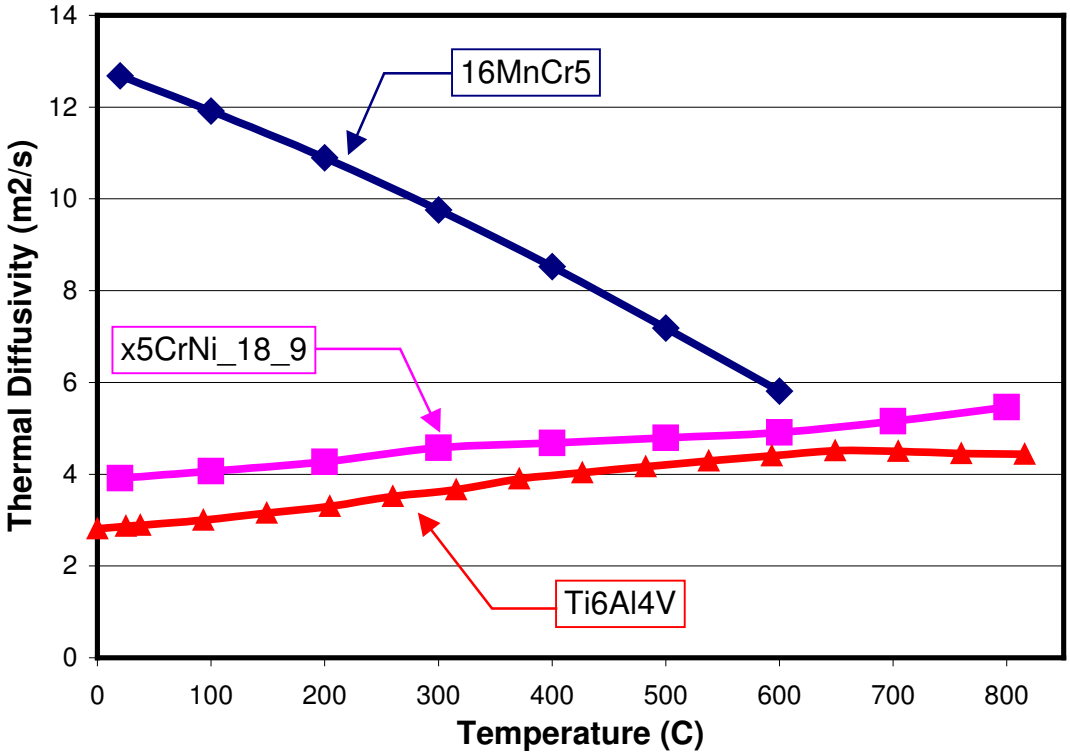

Figure 4.9 Thermal Diffusivity values of 16MnCr5, X5CrNi18_9 and Ti6Al4V

4.4 Laser Heating Experiments

In this section the general experimental procedure will be explained in detail. It is possible to divide the experiments in two subsections as, laser heating and free forming.

The experimental procedure can be given step by step as follows:

Step 1:

The laser parameters such as voltage, frequency and/or pulse duration are assigned by using the laser parameters control unit. The energy is measured just after the

laser beam leaves the cavity, and the energy value is displayed on the laser parameters control unit (Figure 4.3). There exists loss of energy in the fiberoptic cable, which transmits the laser to the press. This loss of energy is less than 4% up to the length of 10 m (the fiberoptic cable used throughout the experiments is exactly 10 m long). These parameters are modified to obtain the heating values that are previously defined. Because of the limitations arise from the flash lamp utilized and the usage of the fiberoptic cable; laser parameters' range is limited (Table 4.2).

Table 4.2 Application of different laser parameters for different materials

Material	**16MnCr5**	**X5CrNi18_9**	**Ti6Al4V**
Frequency (Hz)	60	60	60
Pulse Time (ms)	1.0	1.0	1.0
Voltage (V)	450	450-500	400-520
Energy (J/Pulse)	3.0	3.0 - 4.1	2.15 - 4.50

The surface condition and heat absorption characteristics of the materials play a critical role in laser heating. The more shiny the surface of the material, the more light will be reflected from the surface and consequently the material will be less heated which will cause problems in the subsequent forming step. As a precaution the surface of the materials are coated with black and dark blue paint (Figure 4.10). This painting process is mainly required for x5CrNi18_9 and Ti6Al4V specimens.

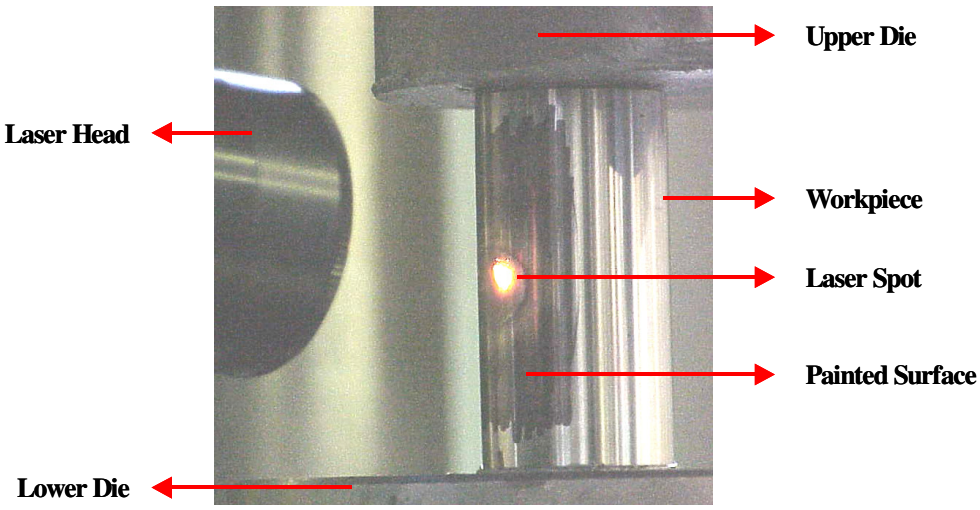

Figure 4.10 Laser Heating (surface is painted)

On the other hand, for the 16MnCr5 specimens the problem is the scale layer on the surface, which burns while heating and forms a dust layer on the lens of the laser head. This layer absorbs large amount of energy of the laser beam and causes failures on the lens.

Step 2:

The robot arm program parameters such as speed and the geometry of the heating profile are defined. As previously explained, the laser head and pyrometer is attached on the robot arm, which is programmed to create heating profiles. An example of these profiles is shown in Figure 4.11, which is composed of three concentric circles with the diameters 10 mm, 6 mm and 4 mm. The number of cycles, speed of the robot arm (which is approximately 8 mm/s at maximum level) and the number of the inner circles can be modified on the computer program, according to the required heating procedure. The number of cycles is determined due to the final temperature reached and the average temperature, which is required for local forming (around melting temperature).

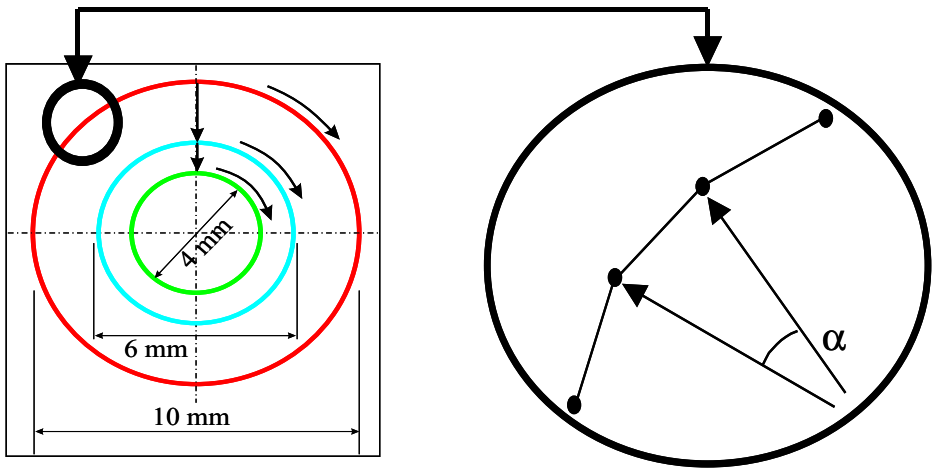

Figure 4.11 The heating profile (idealized & actual) representing the movement of the robot arm

In Figure 4.11, inner region of the smallest circle is not heated and a ring shaped profile is obtained. The idea behind this "ring" shape heating procedure is to weaken the material around a specified region and to obtain the local bulge by forming the inner, relatively harder region, which is only heated through conduction. This means in fact, obtaining a region on which the colder and the

harder part can easily slide. For this reason the heating depth, the speed of the robot arm and the area to be heated has great importance.

Another important parameter in the laser heating part of the process is the distance between the specimen and the laser head. The position is important because as the spot size changes the peak power value of the laser beam changes. The focus position of the beam is selected to be below the surface of the specimen as it is the case for most of the heating applications. Throughout the experiments the laser head position is kept 40 mm to 52 mm away from the specimen surface.

The depth of heating should be arranged such that, the required amount of relatively harder material is forced to move to the outside of the material to form the bulge region. On the other hand the speed of the robot arm and the radius of the heated region are mainly related with the aim of obtaining a stable heating region. This fact can easily be understood from Figure 4.12. In Figure 4.12(a) a Ti6Al4V specimen is heated by using a heating procedure composed of 4 concentric circles (with the diameters of 8 mm, 7 mm, 6 mm and 5 mm), 20 cycles, on the other hand in case (b) which is also composed of 4 concentric circles with the same diameters but 15 cycles are applied. The main difference between the two heating profiles is the speed of the robot arm. The speed is approximately 7.5 mm/s in case (a), whereas it is 6 mm/s in case (b). As it can be observed from the graph a more stable heating behavior is obtained in case (b), which would certainly be the preferred heating procedure. But this does not mean that the slower the robot arm speed the better is the heating result, because this may yield to surface melting.

Step 3:

Both the laser and the robot arm are executed simultaneously. This is done manually due to the setup but it can also be automated. When the duration of the heating process is finished the laser shuts itself down and the robot arm moves back. Finally, the press is activated and the forming stage starts.

One of the most important problems about heating is related with the difficulties in collecting the temperature data at the laser-heated region (see Section 4.2.3). As the

energy is applied to a very small area in laser heating, the temperature changes suddenly to elevated temperatures around the melting point, which is around 1650^{o}C for Ti6Al4V. But, as the upper limit of the pyrometer is not enough for the measurement, the temperature data taken from the pyrometer is processed to understand the general characteristics of the heating curve. This is important especially for comparing the temperature data of the finite element method simulations to the actual case.

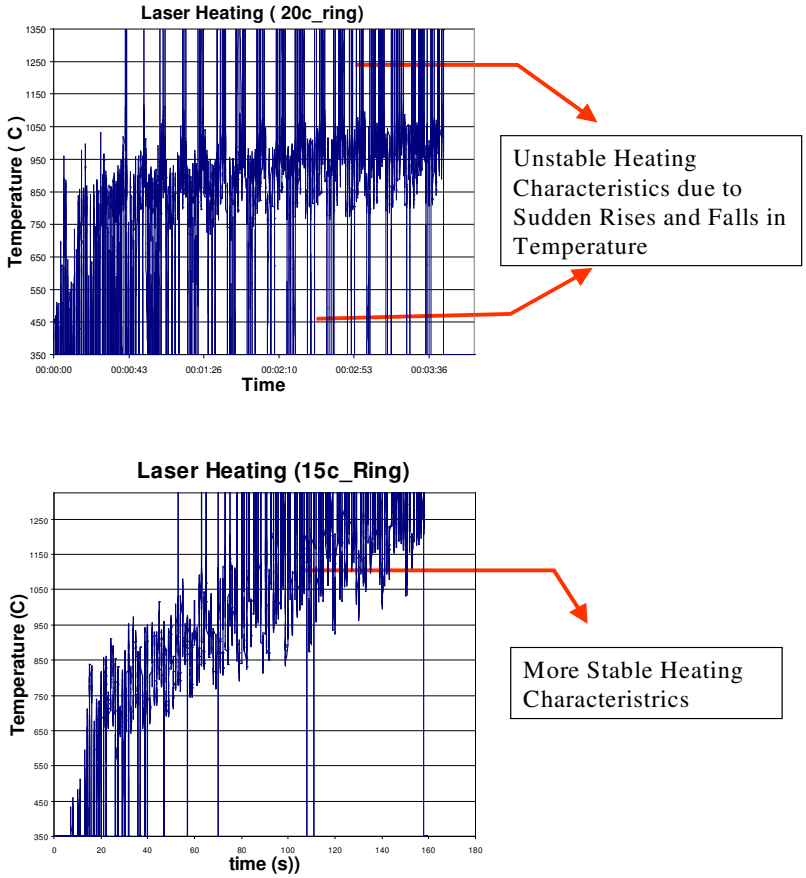

Figure 4.12 Example of an unstable and a stable heating characteristics.

4.5 Forming Experiments

The forming parameters are the upsetting ratio and the deformation rate. Upsetting ratio (Equation 4.2) should be selected such that the localized bulge formation should be observed. If the upsetting ratio is too much then the bulge region gets

wider together with barreling and localization cannot be maintained, on the other hand if the ratio is too low then it will be hard to obtain any bulge formation out of the specimen body. Throughout the experiments a constant upsetting ratio of 2/3 is applied.

$$\text{Upsetting Ratio} = \frac{l_{final}}{l_{initial}} \tag{4.2}$$

Deformation rate is mainly related to the heating problem. The deformation rate should be selected as high as possible because as the time passes the workpiece cools down and the plastic region that is aimed to be forged out gets smaller and shallower. A constant press speed of 3.7 mm/s is applied due to experimental setup limitations. As the press is designed not for metal forming but for processing plastics the press force is not maintained at higher press speeds.

Cylindrical specimens are used and the length to diameter ratio is chosen to be 2.0, which is less then the critical value of 2.3 in terms of buckling in a single stroke upsetting process, for solid steel specimens. It is known that the critical ratio is smaller for hollow specimens, however due to the limitations of the set up (the robot arm collides with the upper column of the press for smaller final workpiece lengths); the ratio of 2 is kept also constant for the hollow specimens. Also the specimens are prepared in four different geometries. The outer diameter and the length, which are 30 mm and 60 mm respectively; being constant the inner diameter varies from 0 to 22 mm (Table 4.3).

Also, in order to reduce the friction between the workpiece and the flat dies and to suppress tool wear, GleitMetall-Paste of Techno Service GmbH is used as the lubricant. This lubricant is effective in the temperature range of -180^{o}C to 1450^{o}C under maximum working pressure of 2353 N/mm^2.

Table 4.3 Geometric specifications of the specimens used

Outer Diameter of the Workpiece	***Inner Diameter of the Workpiece***
d_0 ***(mm)***	d_i ***(mm)***
30 / 40	0 / 21
Length of the Workpiece	18 / 24
L_0 *(mm)*	20 / 27
60	22 / 29

4.6 Results of the Experiments and Comments on the Process

Before commenting on the experimental results and the forming and heating parameters that affect the resultant final shape, it is vital to understand the general mechanisms of the process. More than 160 experiments were done in order to understand and to gain control on the process. Approximately 100 of them were only laser heating experiments for obtaining stable and adequate heating profiles. In these experiments the effect of the heat flux applied, effect of material type, effect of the distance between laser head and the surface of the workpiece (an optimum distance was selected), effect of the initial geometry on heating, and effects of different heating profiles were examined. The remaining experiments were the forming experiments. A list of all the experiments is given in Table 4.3 at the end of the chapter. The selected and examined heating profiles were applied to the specimens as a preheating step and forming was realized. Cut sections were taken from the sample experiments and the flowlines and the microstructure were examined. The results of the sample experiments and comments on the final products will be given throughout the section.

Figure 4.13 shows a cut section that is chemically etched in order to make the flowlines visible under microscope. The final product can be examined in two main regions, the locally laser heated front side and relatively colder backside. The backside is cold formed, and only buckling behavior is observed in this region. Just

like the walls of an unheated hollow workpiece that is formed between two flat dies, the backside buckles outside of the workpiece body. On the other hand, forming mechanisms are much more complicated in the locally laser heated front side, where mainly three different regions are observed; the *primary local bulge*, the *central region,* and the *secondary inner bulge*. The material flow in the region shows parallel behavior with the temperature gradient in the subject region and for this particular case the temperature distribution is observed to be homogenous in the heated zone. Also effect of high heat flux is observed in primary local bulge region.

If the flowlines are examined, it is observed that the forming first takes place in the primary local bulge. The primary bulge is fed from the upper and lower walls as shown in Figure 4.14. Apart from these two material flow paths, material also flows from the two sides to the primary and secondary bulge regions. The relative thinning on the two sides proves this idea, which makes these regions critical for crack formation also (Figure 4.15).

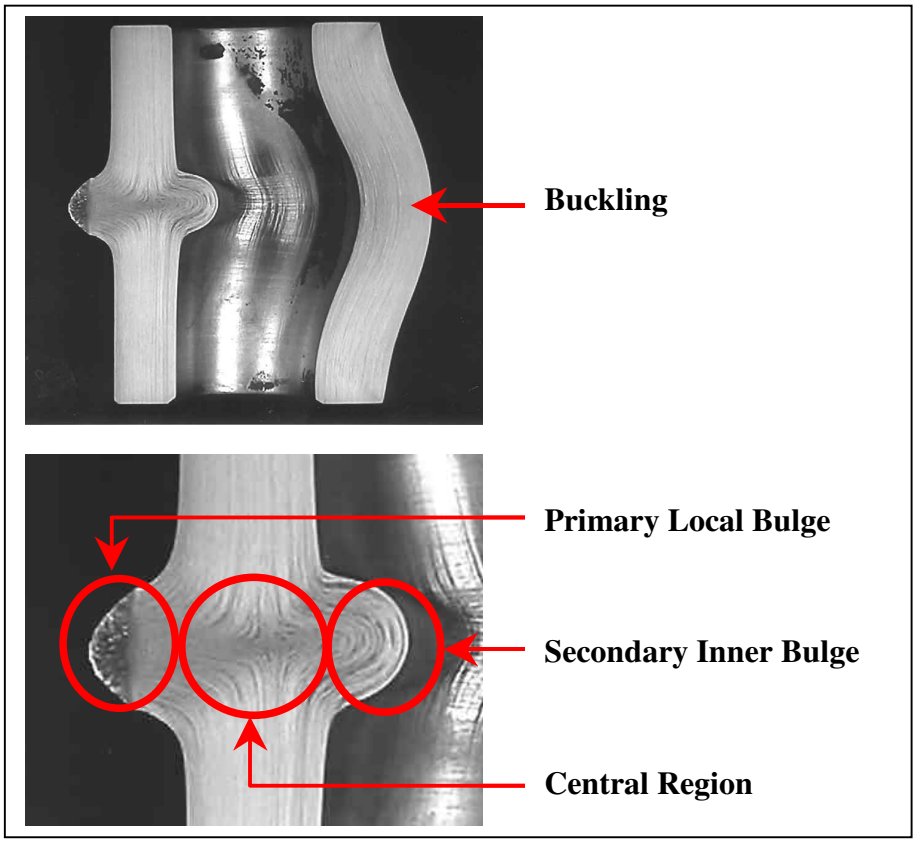

Figure 4.13 Flowlines of a final hollow product

During the forming operation, the material flowing from upper and lower regions collide (or fold on each other) and forms the central region which acts as a *separator* that directs some of the material to the primary bulge region and some of them to the inside to form the secondary inner bulge region (Figure 4.14). It is also understood throughout the experiments that, the formation of the secondary inner bulge is a *must* for the formation of a local primary bulge. This behavior occurs as a result of the cooling of the inner region. As the material in the central region gets colder, the yield strength increases and as a result the material that flows from the upper and lower regions is directed to the primary local bulge region.

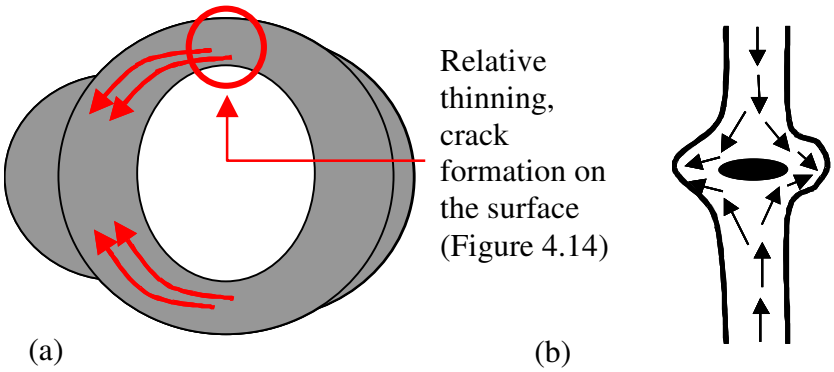

Figure 4.14 Material flow paths.

In the light of the heating experiments conducted, the most important parameters affecting the forming procedure in this study are; the surface temperature and the heat penetration into the material. In case of inadequate heating, it becomes impossible to form a bulging region. Because of the friction between the workpiece and the die surfaces, there occurs buckling to the inside of the specimen on the midplane (Figure 4.16b). On the other hand if the heating procedure is appropriate, the material flows to the inside and outside of the hollow specimen simultaneously and forms the bulging region (Figure 4.16c). So it can be concluded that the process window is dependent on the heating parameters (which is also proven by FEM, see Chapter 6).

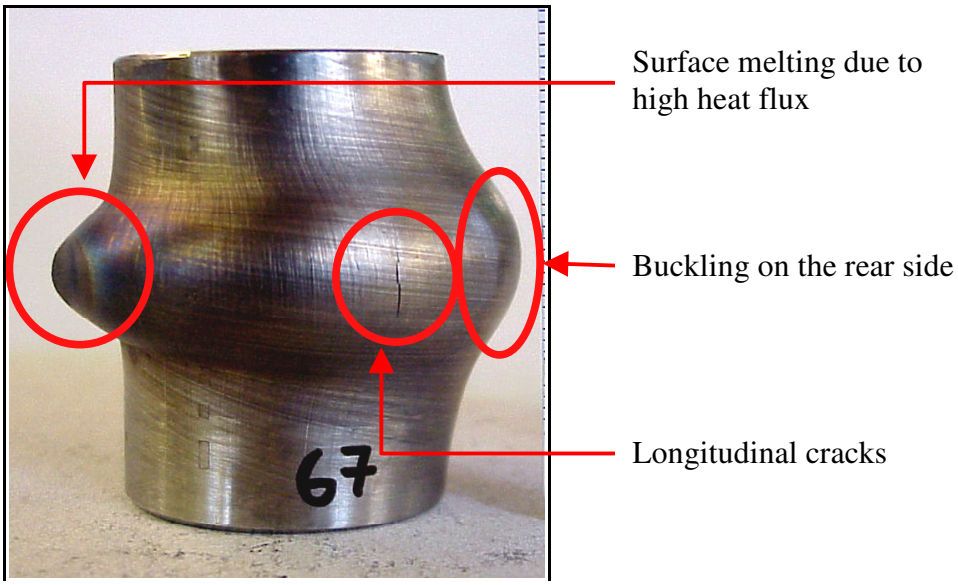

Figure 4.15 Crack formation on a Titanium alloy product

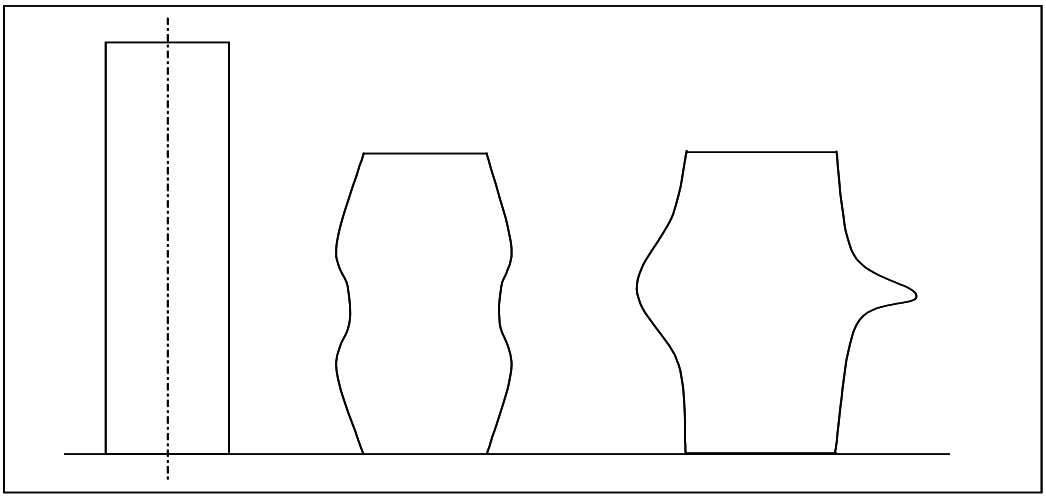

Figure 4.16 (a) Initial Shape of the Specimen (b) Final Shape Obtained for Inadequate Heating (c) Final Shape Obtained for Proper Heating.

The effect of the thermal energy given to the specimen by comparing the final shapes of the specimens, whose initial geometries are the same but subjected to different energy levels. As previously explained, the energy output of the laser can be controlled by adjusting the voltage applied. In Figures 4.17 and 4.18, the results are shown (same initial geometry, same heating profile and time are applied). It is

observed that, as the energy given is increased the heated region gets more and more localized as the rate of energy given to the target region becomes much more compared to the rate of energy drawn by thermal conduction.

Similarly in Figure 4.18, the initial dimensions of the specimens are again the same, but the final shapes of the rear walls that are different from each other. The barrel shape of the rear side is due to buckling. In experiment 72, the heat flux given to the specimen is less than the others; therefore, the temperature gradient between the heated side and the rear side is less compared to the other two samples. As a result, the final shapes of the walls on the two sides are more like each other. On the other side, in experiment 77, the shapes of the heated and the rear-side walls are different. The desired local deformation on the heated side is more visible in this case.

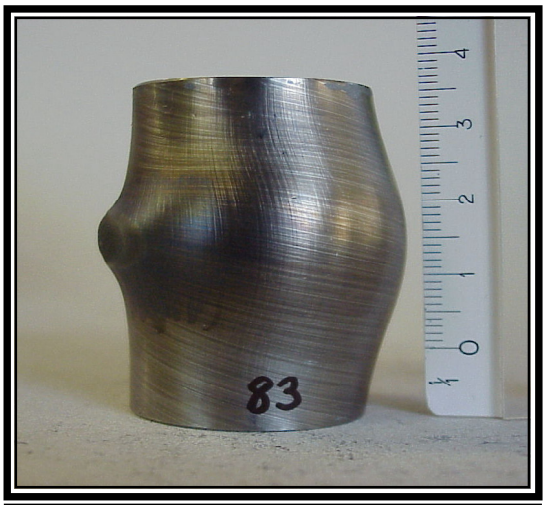

Experiment 83
Voltage: 475 V
Energy: 3.6 J/Pulse

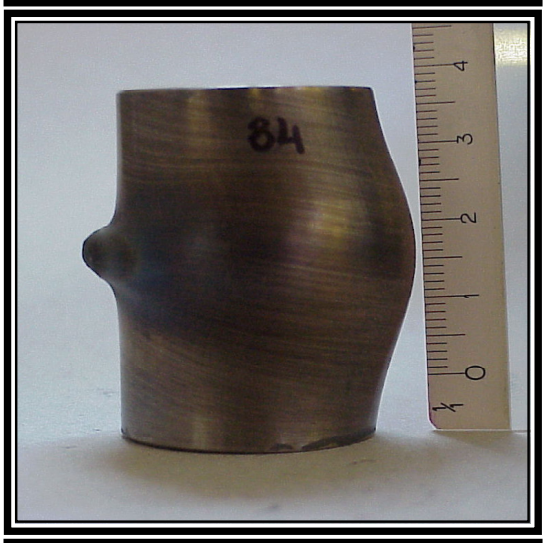

Experiment 84
Voltage: 500 V
Energy: 4.1 J/Pulse

Experiment 85
Voltage: 520 V
Energy: 4.5 J/Pulse

Heating Profile: 4 Inner Heating Circles, 25 Passes.

Initial Geometry: Outer Diameter: 30 mm
Inner Diameter: 16 mm
Length: 60 mm

Figure 4.17 The effect of energy given to the workpiece.

Experiment 72
Voltage: 400 V
Energy: 2.1 J/Pulse

Experiment 71
Voltage: 450 V
Energy: 3.1 J/Pulse

Experiment 77
Voltage: 475 V
Energy: 3.5 J/Pulse

Heating Profile: 4 Inner Heating Circles, 25 Passes.

Initial Geometry: Outer Diameter: 30 mm
Inner Diameter: 18 mm
Length: 60 mm

Figure 4.18 The effect of energy given to the workpiece.

In fact, there exist some limitations on this mechanism. First of all, the limitations of the laser heating setup must be taken into account. The maximum energy that can be produced by the laser device is limited because of the utilization of the fiberoptic cable and the portable laser head. As previously explained, less than 4% of the energy is lost in the fiberoptic cable, in addition to this, the voltage and consequently the maximum energy is also limited by the laser head usage. The maximum allowable voltage value of 520 V and the energy of 4.5 J/ms were applied throughout the experiments.

In addition to this, the surface quality of the final product sets a limitation on the maximum energy level. In laser heating, material is scanned by the laser, which is focused on a very small area (see Chapter 2). As a result of this, high heat flux values are obtained. On the contrary, this may cause sudden rises and falls in the temperature of a distinct position on the surface of the workpiece (Figure 4.19), which lead to the melting or even vaporization of the material. That means, the material is removed from the surface of the specimen and poor surface quality is observed on the final product.

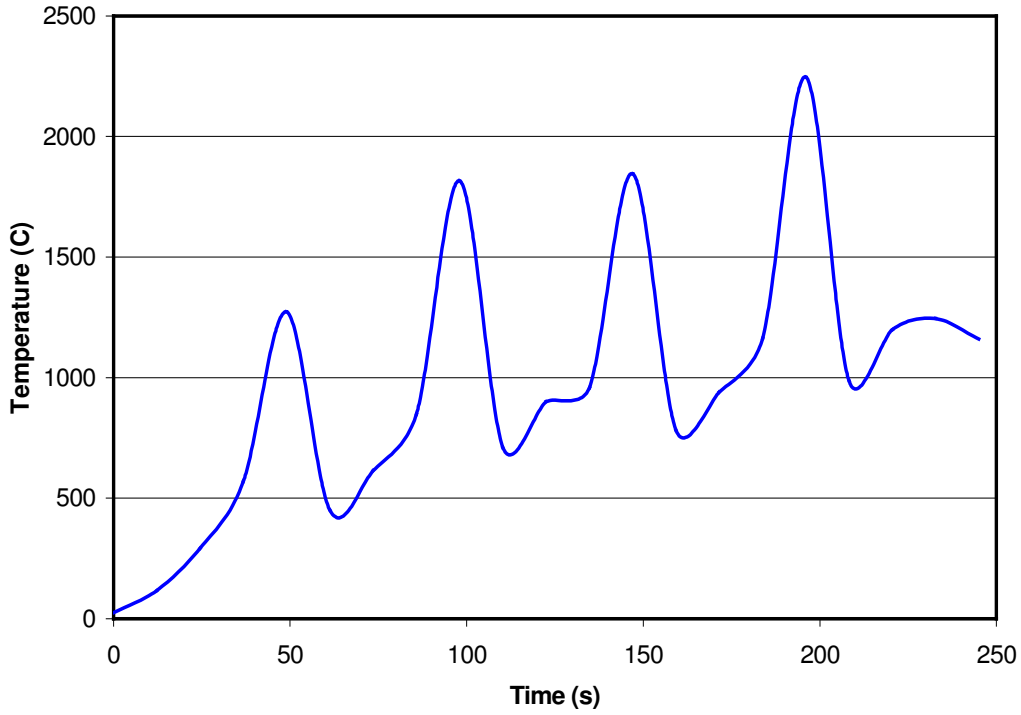

Figure 4.19 Sudden rises & falls in the temperature of a certain point on the surface (FEM data for experiment 85)

Another important point that has to be taken into account is the differences of ductility in different regions of the workpiece due to the temperature effect. For most of the materials, as the temperature increases the ductility of the material also increases (sometimes dramatically). As the local heating is applied to the target region, the ductility of the material increases much more in that region compared to the other parts, for example the rear side of the specimen. And if high stains are applied for forming, this difference in ductility becomes an important problem for the process such that, as the local heated part is hot forged, the rear side is (relatively) cold forged which *may* cause some cracks on that regions. This yields to the unsatisfactory final products, especially for less ductile materials (Figure 4.20). This fact is also proven by finite element method simulations. The representation in Figure 4.20 shows the strain distribution in a sample problem where light colors imply the higher strain regions. Relatively larger strains on the two corners shows approximately the same behavior as in the actual case, which predicts the possible regions for crack formation.

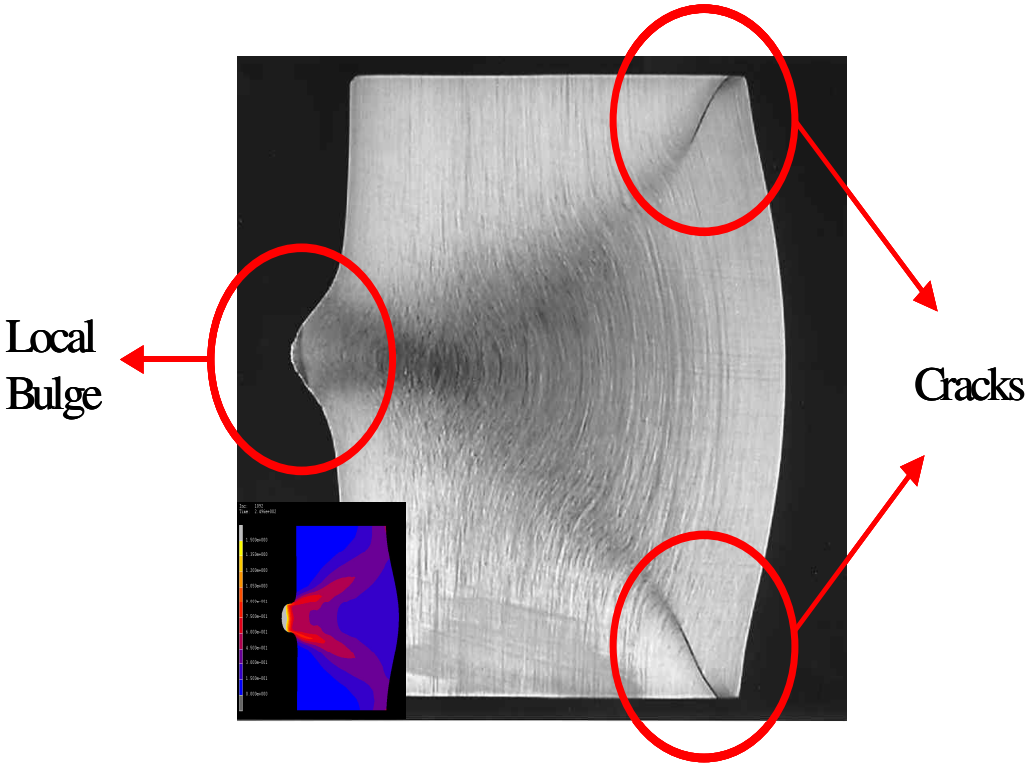

Figure 4.20 Crack formation in relatively cold regions (Ti6Al4V) & strain distribution by FEM.

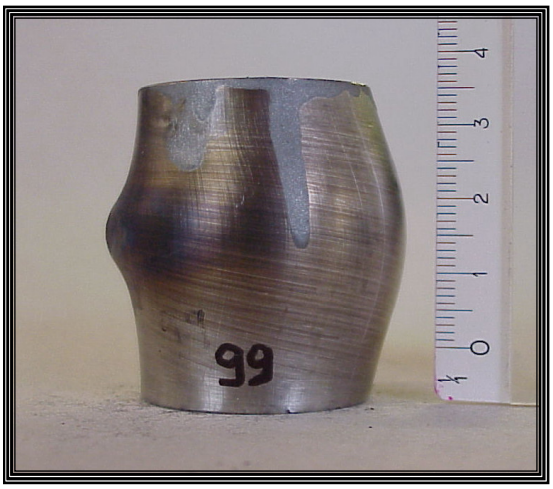

Experiment 99

D_0 = 30 mm

D_i = 14 mm

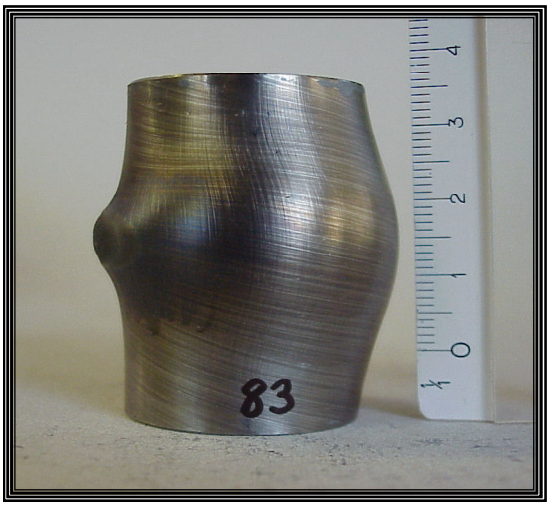

Experiment 83

D_0 = 30 mm

D_i = 16 mm

Experiment 77

D_0 = 30 mm

D_i = 18 mm

Heating Profile:	4 Inner Heating Circles, 25 Passes.
Voltage:	475 V
Energy:	3.6 J / Pulse

Figure 4.21 Effect of the initial workpiece geometry.

Finally, the initial geometry of the specimens must be carefully taken into account (Figure 4.21). From both the heating and forming point of views, the volume of material has great importance. As the volume of the material that can be formed increases, the size of the local bulge on the final product increases. But, the limitation is that; when the amount of the material increases it becomes more and more difficult to ensure the local heating. This is mainly because of the relation between thermal conduction and the heat capacity of the material.

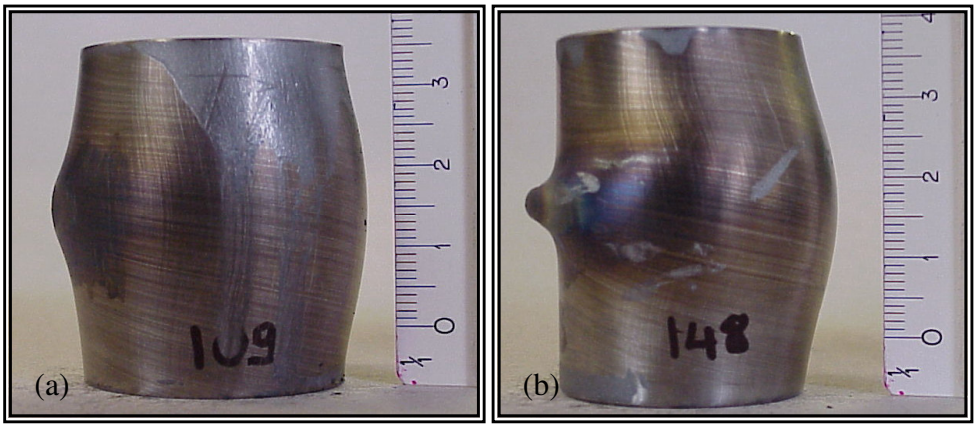

D_o : 30 mm L_0 : 60 mm L/L_0 : 3/4	Energy : 4.1- 4.2 kJ/ms Material: Ti6Al4V

Figure 4.22 Local formations on a solid and a hollow specimen

In order to explain this phenomenon, two cases for the initial geometry can be considered; a solid specimen (Figure 4.22a) and a hollow specimen (with the inner diameter of 14 mm, Figure 4.22b). In case of solid workpiece, there exist more than enough material to form a bulge on the heated region, but on the other hand heat is conducted directly inside of the workpiece to, for example, the rear side. This weakens the effect of local heating but strengthens the formability of the local bulge. On the other hand, in case of a hollow specimen, heat is much more localized on the target region as heat cannot be conducted directly to the other regions and the hole in the middle, can be thought as an air channel for cooling. This time, the deformation on the heated area becomes much more localized but, the buckling effects on the rear parts get dominant on the deformation process as the wall

thickness decreases. So, the optimum point should be found by taking the energy level and the initial geometry into account.

4.7 Conclusion & Recommendations

The experiments show that there exist many parameters that affect the final shape of the product. The laser heating parameters, such as; energy, distance from the laser head to the workpiece surface, the heating profile applied (the shape of the profile and the robot arm speed), the forming parameters such as upsetting ratio, press speed, effect of friction and the initial geometry of the specimens have to be carefully taken into account for obtaining acceptable products.

In order to obtain better primary local bulges, the central region and the secondary inner bulge have to be cooled down as soon as possible during the process. By this way, the material flowing from the upper and lower walls and the side regions can be directed to the local formation area or extra dies may be added to assure the direction of the flow. In addition to this, buckling behavior in the rear part of the workpieces must be avoided to make the local formation on the heated region more visible. For this purpose, larger wall thickness or even solid specimens can be utilized together with a much more effective heating equipment to assure local heating and avoid heat propagation by conduction. Besides, a faster robot arm together with a stronger laser would be beneficial for obtaining stable local heating and to avoid sudden rises and falls which causes surface melting. In addition to these, the initial geometry of the specimens has great effects on both the heating and forming applications and as a result on the final shape of the product.

Apart from the energy and geometrical parameters, the physical properties of the materials must be carefully studied. Approximately 10 of the experiments were conducted with 16MnCr5, 30 of them with X5CrNi18_9 and the remaining 120 with the titanium alloy. In the light of the results of the experiments, following conclusions for material selection can be drawn:

- 16 MnCr5 is found to be “not suitable” for simultaneous hot and cold forming procedures with laser heating for the current parameters because of the following reasons:
  - The material surface is covered with scale that burns easily with laser heating which later sticks on the laser optics and causes the lens failure.
  - Due to high thermal conduction coefficient, the local heating could not be achieved in a shorter time.

The lens failure may be prevented by using a powerful air suction system, which collects and removes the dust before it sticks on the lens. On the other hand, local heating problem can be recovered by conducting the experiment without using the fiberoptic cables, which limit the maximum power to be used.

- X5CrNi18_9 is found to be “suitable” for simultaneous hot and cold forming procedures with laser heating with the current parameters because of the following reasons:
  - Lower thermal conductivity, which makes the localized heating available.
  - Better surface conditions (No scale or dust).
  - Main disadvantage is due to its shiny surface, which can be overcome by painting.

- Ti6Al4V is found to be “the most suitable” for local forming procedures with laser heating (Figure 4.23) for the current parameters because of the following reasons:
  - Extremely low thermal conductivity of the material allows only the heating of the outer shell and constrains heat propagation, which would cause problems for forming.
  - Surface properties are acceptable.
  - Disadvantage of shiny surface may again be recovered by painting.

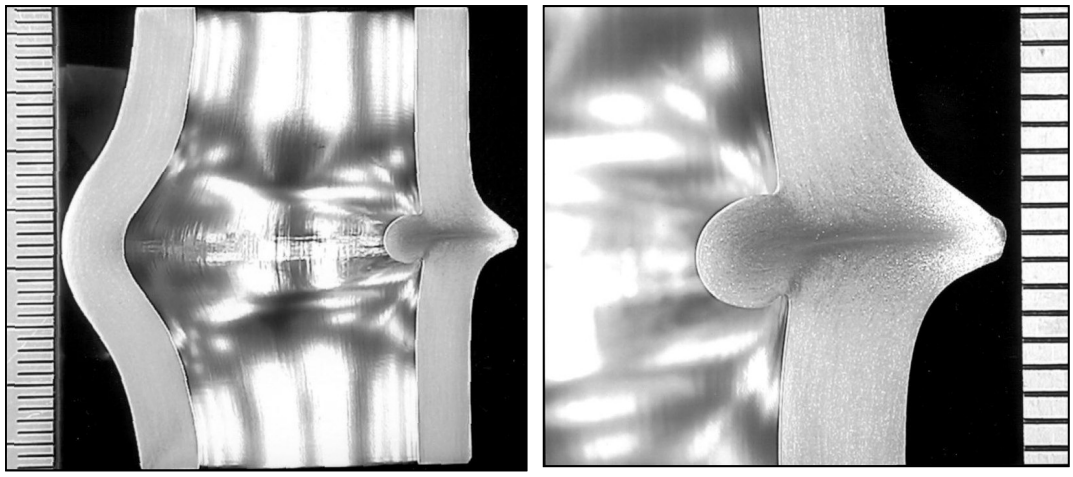

Figure 4.23 Bulge formation on the heated side of the Ti6Al4V specimen.

A summary of all of the experiments is given in Table 4.4, where the experiment number, the laser heating profile applied, the material of the specimen (*St, SS, Ti* denotes 16MnCr5, X5CrNi18_9 and Ti6Al4V respectively), the geometry, the laser parameters and comments (*h* is for *heating*, *u* is for *upsetting*, *R()* is for the *repetition* of a previous experiment, *NS* is for *unsatisfactory local form* and *S* is for the *successful local form*) on the experiments are given. First 40 experiments were for testing purposes; therefore some of the data are missing. The results of the experiments are concluded as successful or not, depending on the size of the local form. An experiment is evaluated as "satisfactory" if a final product is obtained as in the Figure 4.16 (c). It is obvious that the workpieces with the cracks on the surface or with poor surface quality must also be regarded as "not satisfactory". The heating profiles are defined by the number of the concentric heating circles, value of α (see Figure 4.11), diameter of the largest heating circles and the number of passes. The forming experiments are performed after a heating procedure is concluded to be an adequate one; therefore the number of experiments on local laser heating is much more compared to the forming experiments.

Table 4.4 Summary of the experiments

Experiment Number	Heating Profile	Material	d_o	d_i	Voltage (V)	Energy (j/ms)	Comment
1		St	30	-	450	3.0	h
2		St	30	-	450	3.0	h
3		St	30	-	450	3.0	h
4		SS	30	20	450	3.0	h
5		SS	30	20	450	3.0	h
6	4circle_8deg_d8_40ring	SS	30	20	460	3.3	h
7	4circle_8deg_d8_40ring	SS	30	22	460	3.3	h, spark
8		SS	30	16	460	3.3	h
9	4circle_10deg_d8_60ring	SS	30	16	460	3.3	h, melting
10	4circle_10deg_d8_50ring	SS	30	16	460	3.3	h, poor surface
11	4circle_10deg_d8_50ring	SS	30	16	460	3.3	h, spark
12	4circle_10deg_d8_50ring	SS	30	18	460	3.3	u
13	4circle_10deg_d8_50ring	SS	30	18	455	3.2	h
14	4circle_10deg_d8_50ring	SS	30	18	455	3.2	h
15	4circle_10deg_d8_50ring	SS	30	18	455	3.2	h
16	4circle_10deg_d8_50ring	SS	30	18	460	3.3	h
17	4circle_10deg_d8_50ring	SS	30	18	460	3.3	h, spark
18	4circle_10deg_d8_50ring	SS	30	18	460	3.3	h
19	4circle_10deg_d8_50ring	SS	30	18	460	3.3	h
20	4circle_10deg_d8_50ring	SS	30	18	470	3.6	h
21	4circle_8deg_d8_50ring	SS	30	18	470	3.6	h
22	4circle_8deg_d8_50ring	SS	30	18	500	4.1	h
23	4circle_8deg_d8_50ring	SS	30	18	500	4.1	u
24	4circle_8deg_d8_50ring	SS	30	18	500	4.0	u, R(23)
25	4circle_8deg_d8_50ring	SS	30	22	500	4.0	u
26	4circle_8deg_d8_35ring	SS	30	22	500	4.0	u
27	4circle_8deg_d8_50ring	SS	30	-	500	2.15	u
28	4circle_8deg_d8_20ring	Ti	30	-	400	2.15	h
29	4circle_8deg_d8_20ring	Ti	30	-	400	3.0	h
30	4circle_8deg_d8_20ring	Ti	30	-	450	3.0	h
31	4circle_8deg_d8_20ring	Ti	30	16	450	3.0	h
32	4circle_4deg_d8_10ring	Ti	30	-	450	3.0	h
33	4circle_4deg_d8_15ring	Ti	30	-	450	3.0	h
34	4circle_4deg_d8_15ring	Ti	30	-	450	3.2	u
35	4circle_4deg_d8_15ring	Ti	30	16	450	3.2	u
36	4circle_4deg_d8_15ring	Ti	30	18	435	2.9	u
37	4circle_4deg_d8_15ring	Ti	30	20	430	2.8	u
38	4circle_4deg_d8_15ring	Ti	30	22	430	2.7	u
39	4circle_4deg_d8_25ring	SS	30	14	500	4.1	h
40	4circle_4deg_d8_40ring	SS	30	14	500	4.1	h
41	4circle_4deg_d8_40ring	SS	30	14	500	4.1	u
42	4circle_4deg_d8_32ring	SS	30	16	500	4.0	h

Table 4.4 Summary of the experiments (Continued)

Experiment Number	Heating Profile	Material	d_o	d_i	Voltage (V)	Energy (j/ms)	Comment
43	4circle_4deg_d8_32ring	SS	30	16	500	4.0	u
44	4circle_4deg_d8_32ring	SS	30	16	500	4.0	h
45	4circle_4deg_d8_25ring	SS	30	16	500	4.1	u
46	4circle_4deg_d8_25ring	SS	30	18	450	3.1	h
47	4circle_4deg_d8_25ring	SS	30	18	450	3.1	h
48	4circle_4deg_d8_25ring	SS	30	18	450	3.1	h
49	4circle_4deg_d8_25ring	SS	30	20	450	3.1	h
50	4circle_4deg_d8_25ring	SS	30	20	450	3.1	u
51	4circle_2deg_d8_17ring	SS	30	20	450	3.1	h
52	4circle_2deg_d8_25ring	SS	30	20	400	2.1	h,
53	4circle_4deg_d8_25ring	SS	30	20	450	3.1	h,
54	4circle_4deg_d8_15ring	Ti	30	20	430	2.7	h
55	4circle_4deg_d8_15ring	Ti	30	20	400	2.1	h,
56	4circle_4deg_d8_15ring	Ti	30	20	400	2.0	u, NS
57	4circle_4deg_d8_15ring	Ti	30	20	400	2.0	u, NS
58	4circle_4deg_d8_15ring	Ti	30	18	400	2.0	u
59	4circle_4deg_d8_15ring	Ti	30	20	400	2.0	h 47mm
60	4circle_4deg_d8_15ring	Ti	30	20	430	2.7	h 47mm
61	4circle_4deg_d8_15ring	Ti	30	20	454	3.1	h 47mm
62	4circle_4deg_d8_15ring	Ti	30	20	452	3.1	u, S
63	4circle_4deg_d8_25ring	Ti	30	20	400	2.0	h
64	4circle_4deg_d8_25ring	Ti	30	20	430	2.7	h
65	4circle_4deg_d8_25ring	Ti	30	20	450	3.05	h
66	4circle_4deg_d8_25ring	Ti	30	20	430	2.7	u, l_{final}=50mm S
67	4circle_4deg_d8_25ring	Ti	30	20	430	2.7	u, l_{final}=42mm S
68	4circle_4deg_d8_25ring	Ti	30	18	430	2.7	h
69	4circle_4deg_d8_25ring	Ti	30	18	400	2.1	h.
70	4circle_4deg_d8_25ring	Ti	30	18	450	3.1	h
71	4circle_4deg_d8_25ring	Ti	30	18	450	3.1	u (upset 70), NS
72	4circle_4deg_d8_25ring	Ti	30	18	400	2.1	u (upset 69), Crack
73	4circle_4deg_d8_25ring	Ti	30	18	450	3.15	u ratio 1:2
74	4circle_4deg_d8_25ring	Ti	30	18	450-400		u, NS
75	4circle_4deg_d8_25ring	Ti	30	18	475	3.55	h
76	4circle_4deg_d8_25ring	Ti	30	18	475	3.55	h 49mm
77	4circle_4deg_d8_25ring	Ti	30	18	475	3.55	u, 49mm, S
78	4circle_4deg_d8_25ring	Ti	30	18	500	4.05	u, 52mm, S
79	4circle_4deg_d8_25ring	Ti	30	16	430	2.65	h, 47mm
80	4circle_4deg_d8_25ring	Ti	30	16	430	2.7	h, 47mm

Table 4.4 Summary of the experiments (Continued)

Experiment Number	Heating Profile	Material	d_o	d_i	Voltage (V)	Energy (j/ms)	Comment
81	4circle_4deg_d8_25ring	Ti	30	16	450	3.05	h, 47mm
82	4circle_4deg_d8_25ring	Ti	30	16	475	3.65	h, 49mm
83	4circle_4deg_d8_25ring	Ti	30	16	475	3.6	u, 49mm, S
84	4circle_4deg_d8_25ring	Ti	30	16	500	4.1	u, 49mm, S
85	4circle_4deg_d8_25ring	Ti	30	16	520	4.5	u, 52mm, S
86	4circle_4deg_d8_25ring	Ti	30	16	500	4.1	u, 49mm, S
87	4circle_4deg_d8_25ring	Ti	30	14	430	2.7	h, 47mm
88	4circle_4deg_d8_25ring	Ti	30	14	450	2.9	h, 47mm
89	4circle_4deg_d8_25ring	Ti	30	-	430	2.5	h, 47mm
90	4circle_4deg_d8_25ring	Ti	30	-	430	2.5	h, 47mm
91	4circle_4deg_d8_25ring	Ti	30	-	430	2.5	h, 47mm
92	4circle_4deg_d8_25ring	Ti	30	-	450	3	h, 47mm
93	4circle_4deg_d8_25ring	Ti	30	-	475	3.5	h, 47mm
94	4circle_4deg_d8_25ring	Ti	30	-	500	4.0	h, 47mm dust
95	4circle_4deg_d8_25ring	Ti	30	-	500	4.0	h, 49mm dust
96	4circle_4deg_d8_25ring	Ti	30	-	500	4.0	h, 52mm
97	4circle_4deg_d8_25ring	Ti	30	-	520	4.4	h, 52mm
98	4circle_4deg_d8_25ring	Ti	30	14	398	3.6	h, 47mm
99	4circle_4deg_d8_25ring	Ti	30	14	398	3.7	u, 47mm, S
100	4circle_4deg_d8_25ring	Ti	30	14	418	4.2	h, 47mm
101	4circle_4deg_d8_25ring	Ti	30	14	398	3.7	h, 49mm
102	4circle_4deg_d8_25ring	Ti	30	14	418	4.3	h, 49mm
103	4circle_4deg_d8_25ring	Ti	30	14	418	4.3	u, 49mm, S
104	4circle_4deg_d8_25ring	Ti	30	14	418	4.2	h, 52mm
105	4circle_4deg_d8_25ring	Ti	30	14	430	4.55	h, 52mm
106	4circle_4deg_d8_25ring	Ti	30	14	430	4.5	u, 52mm, S
107	4circle_4deg_d8_25ring	Ti	30	14	335	2.1	h, 47mm
108	4circle_4deg_d8_25ring	Ti	30	-	335	2.1	h, 47mm
109	4circle_4deg_d8_25ring	Ti	30	-	416	4.2	u, 49mm, NS
110	4circle_4deg_d8_25ring	Ti	30	-	402	3.7	u, 47mm, NS
111	4circle_4deg_d8_40ring	Ti	30	-	424	4.2	u, 52mm, S
112	4circle_4deg_d8_40ring	Ti	30	-	424	4.2	h, 52mm
113	4circle_4deg_d8_25ring	Ti	40	29	360	2.7	h, 47mm
114	4circle_4deg_d8_25ring	Ti	40	29	380	3.1	h, 47mm
115	4circle_4deg_d8_25ring	Ti	40	29	380	3.1	u, 47mm, NS
116	4circle_4deg_d8_25ring	Ti	40	29	396	3.6	h, 49mm
117	4circle_4deg_d8_25ring	Ti	40	29	418	4.2	h, 49mm
118	4circle_4deg_d8_25ring	Ti	40	29	396	3.6	u, 49mm, S
119	4circle_4deg_d8_25ring	Ti	40	29	418	4.2	u, 49mm, S

Table 4.4 Summary of the experiments (Continued)

Experiment Number	Heating Profile	Material	d_o	d_i	Voltage (V)	Energy (j/ms)	Comment
120	4circle_4deg_d8_25ring	Ti	40	29	418	4.2	u, 49mm, R(119), S
121	4circle_4deg_d8_25ring	Ti	40	27	383	3.1	h, 47mm
122	4circle_4deg_d8_25ring	Ti	40	27	383	3.1	u, 47mm, NS
123	4circle_4deg_d8_25ring	Ti	40	27	400	3.6	h, 49mm
124	4circle_4deg_d8_25ring	Ti	40	27	400	3.6	u, 49mm, S
125	4circle_4deg_d8_25ring	Ti	40	24	400	3.6	h, 49mm
126	4circle_4deg_d8_25ring	Ti	40	24	400	3.6	u, 49mm, NS
127	4circle_4deg_d8_25ring	Ti	30	20	400	3.6	h, 49mm
128	4circle_4deg_d8_25ring	Ti	30	-	400	3.6	h, 49mm
129	4circle_4deg_d8_25ring	Ti	30	16	338	2.1	h, 47mm
130	4circle_4deg_d8_25ring	Ti	40	27	417	4.2	u, 52mm, S
131	4circle_4deg_d8_25ring	Ti	40	24	416	4.1	u, 49mm, S
132	4circle_4deg_d8_25ring	Ti	40	21	416	4.2	u, 49mm, NS
133	4circle_4deg_d8_25ring	Ti	40	24	432	4.5	u, 52mm, NS
134	4circle_4deg_d8_25ring	Ti	40	21	432	4.5	u, 52mm, NS
135	4circle_4deg_d8_25ring	Ti	40	-	400	4.5	u, 52mm, NS
136	4circle_4deg_d8_25ring	Ti	30	20	365	2.7	u, 47mm, S
137	4circle_4deg_d8_25ring	Ti	30	20	424	4.15	h, 49mm
138	4circle_4deg_d8_25ring	Ti	30	18	424	4.2	h, 49mm
139	4circle_4deg_d8_25ring	Ti	30	16	424	4.2	h, 52mm
140	4circle_4deg_d8_25ring	Ti	30	20	423	4.2	h, 52mm
141	4circle_4deg_d8_25ring	Ti	30	18	438	4.5	h, 52mm
142	4circle_4deg_d8_25ring	Ti	30	20	438	4.6	h, 52mm
143	4circle_4deg_d8_25ring	Ti	30	18	418	4.2	u, 52mm, R(78), S
144	4circle_4deg_d8_25ring	Ti	30	16	434	4.5	u, 52mm, R(85), S
145	4circle_4deg_d8_25ring	Ti	30	14	434	4.5	u, 52mm, R(106), S
146	4circle_4deg_d8_25ring	Ti	30	-	434	4.5	u, 52mm, NS
147	4circle_4deg_d8_40ring	Ti	30	-	434	4.5	u, 52mm, S
148	4circle_4deg_d8_25ring	Ti	30	14	418	4.2	u, 49mm, S
149	4circle_4deg_d8_40ring	Ti	30	-	438	4.7	h, 49mm
150	4circle_4deg_d8_40ring	Ti	30	-	438	4.6	u, 49mm, S
151	4circle_4deg_d8_55ring	Ti	30	-	438	4.6	h, 49mm

Table 4.4 Summary of the experiments (Continued)

Experiment Number	Heating Profile	Material	d_o	d_i	Voltage (V)	Energy (j/ms)	Comment
152	4circle_4deg_d8_55ring	Ti	30	-	438	4.6	u, 49mm, NS
153	4circle_4deg_d8_25ring	Ti	30	-	438	4.6	h, 47mm
154	4circle_4deg_d8_25ring	Ti	30	-	438	4.6	u, 47mm, NS
155	4circle_4deg_d8_25ring	Ti	30	-	438	4.6	u, 49mm, NS

CHAPTER 5

METALLURGICAL INVESTIGATIONS

5.1 Introduction

The metallurgical investigation must be done on the resultant samples in order to design and to control the heat treatment procedures, because of the fact that, some properties of the materials are functions of their microstructures and consequently, of their thermal histories. This makes the knowledge and understanding of phase diagrams, very critical. The most of the phase diagrams provide the stable states and microstructures, but even in that case, they are still useful in understanding the development and preservation of nonequilibrium structures and their attendant properties [20].

The materials that were used throughout the experiments are introduced very briefly in the previous chapter. These materials are of three different types; alloy case hardening steel (16MnCr5), stainless steel (X5CrNi18_9), and titanium alloy (Ti6Al4V). If the results of the experiments are examined, the titanium alloy seems to be most advantageous material for such a process (see Section 4.7). For that reason, a detailed information on the microstructural and metallurgical properties of the Ti6Al4V alloy will be given together with the metallurgical study on titanium alloy results. On the other hand, brief information on steel samples, especially for heating experiments will also be submitted in this chapter.

5.2 Metallurgical Investigations on Steel Samples

The heat-affected zones are examined in steel samples as well as the titanium alloy ones. Before giving some examples, it is useful to give some brief information on the iron-carbon system.

5.2.1 The Iron-Carbon System

Some substances are capable of changing within the solid state to other phases or crystalline structures. This ability of changing into different phases is called "allotropy". Being an allotropic element, iron changes from face-centered cubic to body-centered cubic during cooling. The cooling curve for iron, Figure 5.1, shows the temperatures at which important structural changes occur. Iron solidifies at 1538°C into a BCC form known as *delta (δ) iron*. Upon further cooling to 1401°C, the atoms rearrange themselves to a FCC austenite, known as *gamma (γ) iron*. Gamma iron is found to be nonmagnetic. As the temperature further drops to 908°C, another phase chance occurs, in which the FCC structure changes back to a BCC nonmagnetic structure known as *beta (β) iron*. Below 768°C, alpha iron becomes magnetic alpha (α) iron accompanied by changes in internal energy and electrical conductivity [21].

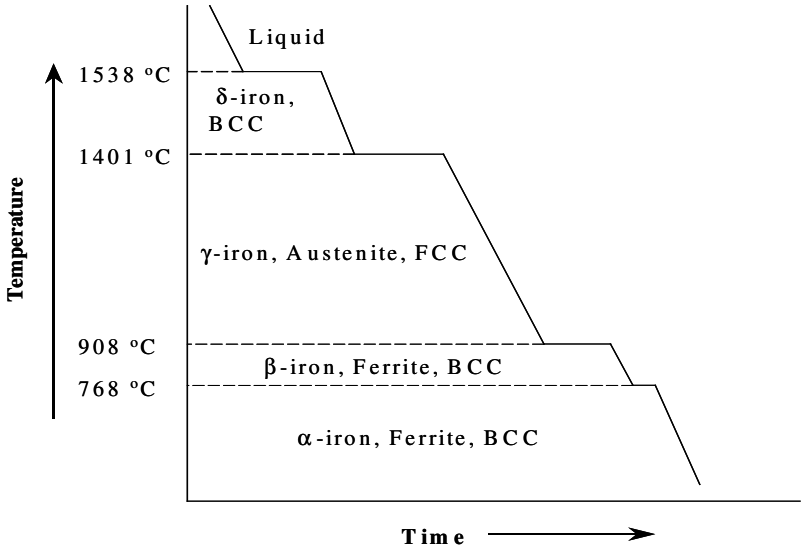

Figure 5.1 Cooling curve for pure iron.

On the other hand the cooling rate has great importance in the transformation phenomena. Continuous cooling transformation diagram shows the limits of the reaction curves in Figure 5.2. It can be observed from the diagram that according to different cooling rates different phases are obtained.

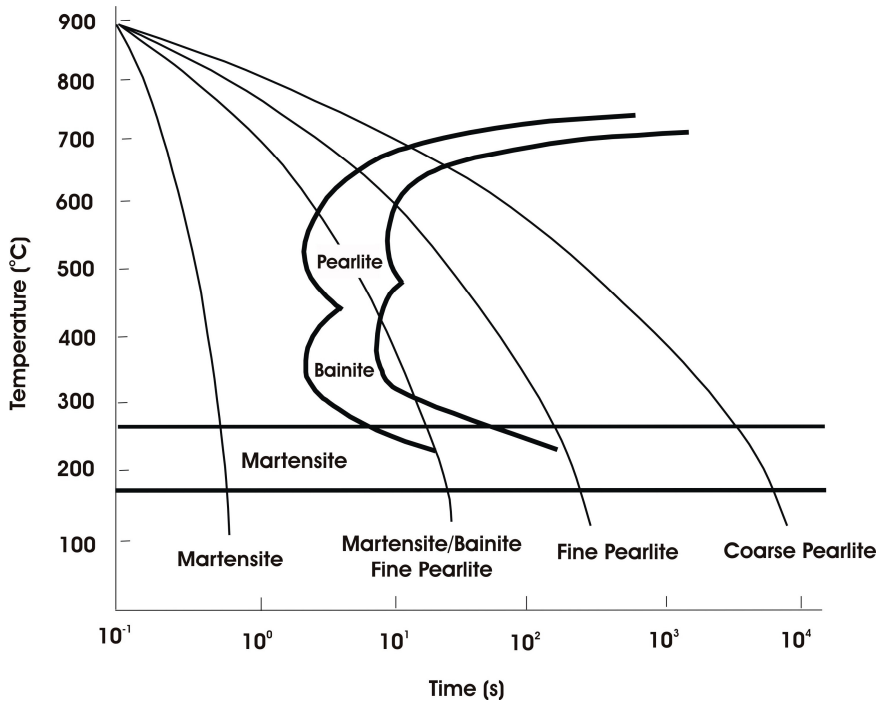

Figure 5.2 Continuous cooling transformation diagram of the iron-carbon system.

The allotropic change temperatures given above are influenced by the presence of the alloying elements. When iron is alloyed with another metal, the temperature of phase changes will be different for every combination of the two metals. Alloys of iron and carbon are the most widely used and least expensive of all metal alloys. The important point about the iron-carbon alloys that has to be emphasized is the fact that, their properties can be very decidedly changed by heating and cooling under controlled conditions.

The iron-carbon diagram (Figure 5.3) not only shows the type of alloys formed under very slow cooling, but also indicates the proper heat-treating temperatures. In addition to this, it is possible to observe that the properties of steel and cast iron can be radically changed by heat treatments. More detailed information on the iron-carbon phase diagram is given in the next section.

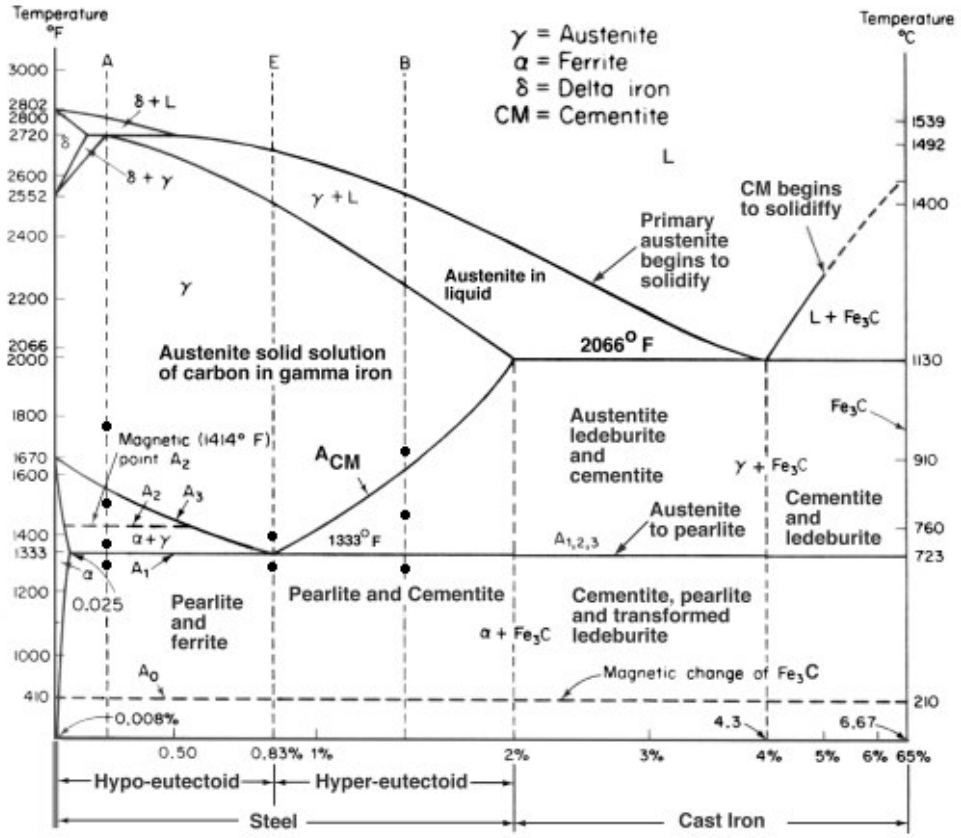

Figure 5.3 Iron-carbon phase diagram [22]

5.2.2 Description of Iron-Carbon System Structure

The structures shown on the iron-carbon alloy diagram (Figure 5.3) and on the continuous cooling transformation diagram (Figure 5.2) will be described in this section.

When carbon steel is viewed through a microscope, the microstructure may be identified as *pearlite, ferrite, cementite (iron carbide), austenite, or bainite* with some variations depending on the heat treatment [20, 21, 23].

- *Cementite* is the hardest structure on the iron-carbon diagram. The carbon content is 6.67% by weight. Cementite structure is brittle and has low tensile strength but high compressive strength.
- *Austenite* is a solid solution of carbon in FCC gamma (γ) iron. It has the ability to dissolve carbon to a maximum limit of 2% at 1129°C. Austenite is not stable

below the critical temperature and decomposes into pearlite, ferrite and/or cementite.

- *Ferrite*, which is also known as alpha (α) iron, has the BCC structure. It dissolves only 0.008% carbon at room temperature and has a limit of 0.025% carbon at 721^{o}C. Ferrite is the softest structure that appears in the diagram.
- *Pearlite* can be said to be a two-phase lamellar structure consisting of thin platelets of iron carbide in a ferrite matrix. Slow cooling is an important point in the formation of the pearlite structure (Figure5.4c).

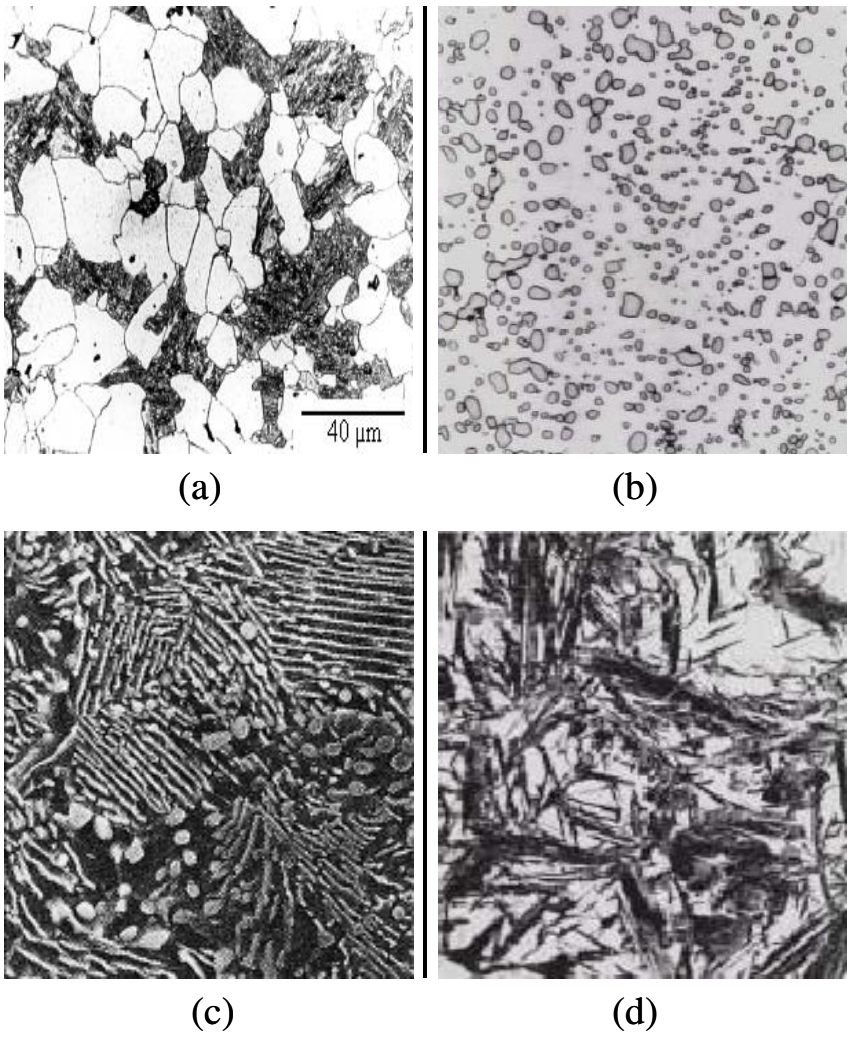

Figure 5.4 Microstructures viewed under microscope; (a) Bainite (b) Spherodite (c) Pearlite (d) Martensite [20]

- *Bainite* has a microstructure that is composed of ferrite and cementite phases. Electron microscopy is necessary to observe the microstructural details of bainite, as they are very fine and as a result of this fine microstructure, bainitic steels are harder than the pealitic ones and have a good combination of ductility and strength (Figure5.4a).
- *Spheroidite* microstructure is observed if a steel alloy having either pearlite or bainite microstructures is heated to, and left at a temperature below the eutectoid for a sufficiently long period of time. The most important fact about the spheroidite microstructure is that, of all steel alloys, those that are the softest and weakest have a spheroidite microstructure (Figure5.4b).
- *Martensite* is formed as a result of rapid cooling of austenitized iron-carbon alloys. On the contrary of the spheroidite structure, the martensitic one is the hardest and the strongest type. In addition to this, martensite phase is the most brittle one with negligible ductility (Figure5.4d).

5.2.3 Examinations on Heat Affected Zones in Steel Samples

After the heating experiments some of the products were cut and microstructural examinations were applied. If a heated and cooled stainless steel sample is studied, three different regions on the material are observed (Figure 5.5).

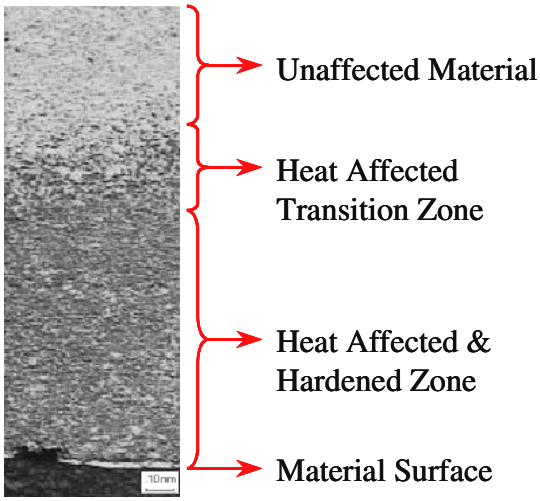

Figure 5.5 Different zones in the microstructure of a stainless steel product.

These three regions are the hardened material zone, transition material zone and the unaffected material zone. The hardened material zone together with the transition zone forms totally the “heat affected” zone. The hardening of the material can be interpreted as the martensite forming during the high cooling rate after the laser heating process. This rapid cooling is directly related with the amount of material that is heated above the recrystallization temperature. As laser heating is applied from the surface and it is not easy to penetrate the heat into the material quickly, cooling takes place on the surface and after the application is completed the heat-affected zone is rapidly cooled from the surface by convection and by conduction inside the material. In the light of this information, the hardened material zone or totally the heat-affected zone is highly dependent on material, surface conditions, laser head position and laser power parameters. Here, one can suggest increasing the power that is given by the laser beam to the material surface. But, this creates other problems rather than solving the existing ones, such as the melting of the surface (Figure 5.6), which causes the formation of the sparks between the lens and the surface. This may lead to the failure of the lens. But after all, a hardened surface may be interpreted as an advantage depending on the final product required.

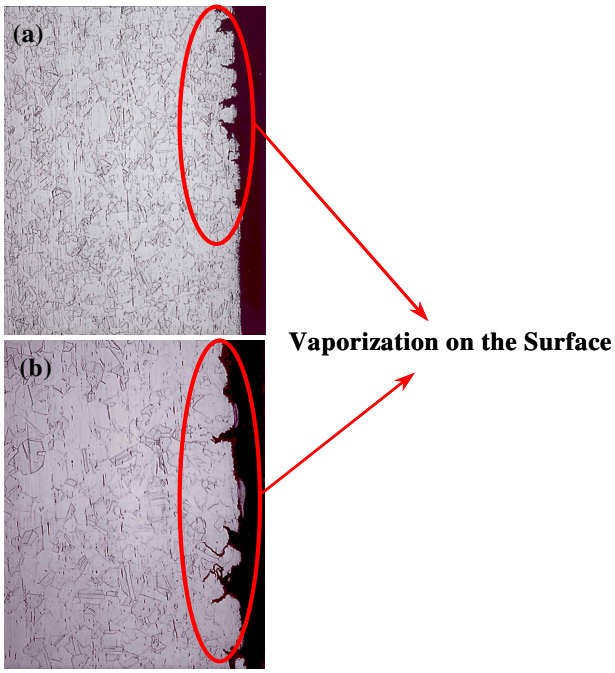

Figure 5.6 Vaporization on the stainless steel surface due to high energy level. Magnification of (a) 49X (b) 90X

5.3 Metallurgical Investigations on Titanium Alloy Samples

The heat affected material zones due to local laser heating are examined together with the local hardness values in order to study and understand the formation characteristics. As most of the successful products are obtained from the titanium alloy, a more detailed examination is done. Before commenting on the results, some basic microstructural properties of Ti6Al4V will be discussed.

5.3.1 Brief Information on Titanium and Titanium Alloys

Titanium is a silver-gray metal with the density of 4.5 g/cm^3 and a melting point of 1726^{o}C. The *pure* titanium has the purity of 99.5%-99.0% by weight. The main alloying elements are iron, carbon, oxygen and nitrogen, which are also called the interstitials Just like the iron, titanium is also an allotropic element in nature and may exist in either the hexagonal close packed (alpha) or body centered cubic (beta) structure, but *pure* titanium is considered to be an alpha phase in which the oxygen is the alloying element. At approximately 883^{o}C, transition from alpha phase to beta phase occurs. The exact transformation temperature is strongly influenced by interstitial and substitutional elements, therefore depending on the purity of the element.

Oxygen content also determines the grade and strength of the material. Such that, addition of each 0.1% Oxygen equivalent of interstitials elements (Eq. 5.1) in pure titanium increases the strength by approximately 120MPa (Figure 5.7). On the other hand, addition of interstitials decrease the toughness. Therefore if high toughness is required for a particular application, the alloy is produced with extra-low interstitials (ELI grade). Titanium provides a wide range of physical and mechanical properties with about twenty specific commercial alloy compositions [21, 24].

$$\% \text{ O Equivalent} = \% \text{ O} + 2\% \text{ Ni} + 0.67\% \text{ C} \qquad \text{(Eq. 5.1)}$$

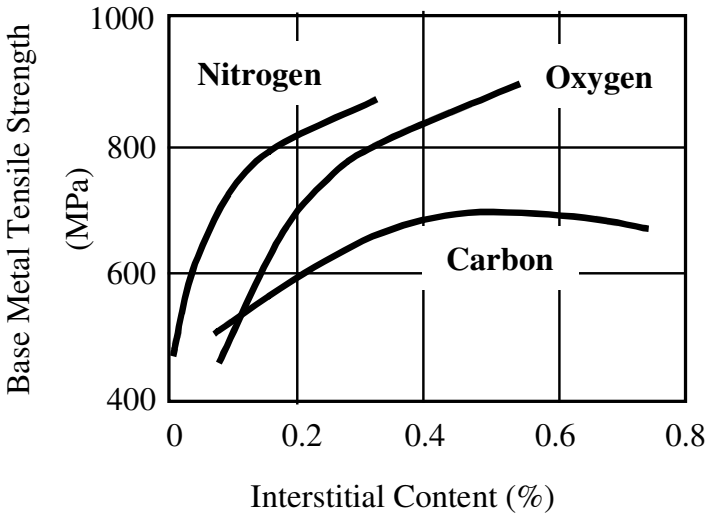

Figure 5.7 Effect of interstitial element content on the tensile strength.

By adding certain alloying elements, like oxygen, nitrogen, and aluminum, the alpha phase can be stabilized therefore the beta transus temperature is increased. On the other hand, some other alloying additions including chromium, columbium, copper, iron, manganese, molybdenum, tantalum and vanadium, are used to stabilize the beta phase by decreasing the transition temperature.

The important fact about the phase changes of titanium is that, a HCP alpha alloy slowly starts to form just below the transformation temperature, as a result of the cooling of BCC beta alloy. The point is; it is not possible to retain the beta phase even by rapid cooling.

5.3.2 Titanium Alloy Classification

Commercial titanium alloys are classified conventionally in three different categories as alpha alloys, alpha-beta alloys, and beta alloys according to their equilibrium constitution, which varies with the types and concentration of alloying elements. The effects of the alloying elements are summarized in Table 5.1.

Alpha alloys are single-phase alloys that are stable at the room temperature. The crystal structure is hexagonal close packed structure. Alpha alloys usually contain aluminum as a stabilizer (Figure 5.8) and has a strong hardening effect (Figure 5.9). The most important and widely used alpha alloy is Ti5Al2.5Sn. These alloys have excellent strength characteristics and oxidation resistance in especially the 315°C – 595°C range.

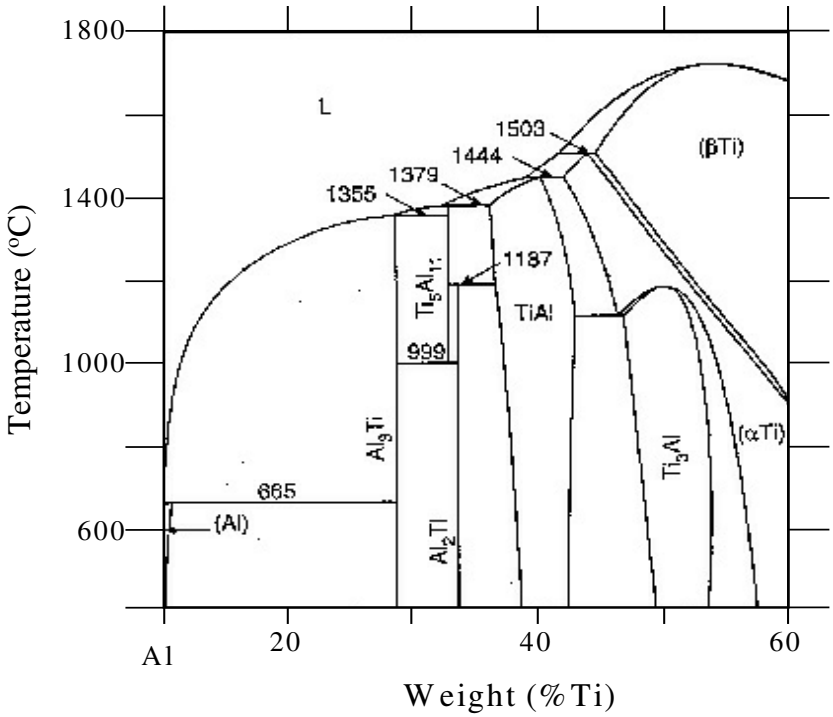

Figure 5.8 The Titanium Aluminum Phase Diagram. Small addition of aluminum increases the amount of alpha phase stable at a given temperature [25].

Table 5.1 Effects of Alloying Elements

Alloying Element	Range (wt %)	Effect on Structure
Aluminum	2-7	α– Stabilizer
Tin	2-6	α– Stabilizer
Vanadium	2-20	β– Stabilizer
Molybdenum	2-20	β– Stabilizer
Chromium	2-12	β– Stabilizer
Copper	2-6	β– Stabilizer
Zirconium	2-8	α and β strengtheners
Silicon	0.05-1	Improves creep resistance
Gallium, Germanium, Carbon, Oxygen and Nitrogen are also α stabilizers.		

Alpha phase alloys have good ductility and weldability. An important point about the alpha alloys is that, they cannot be hardened by heat treatment. The can be hardened by cold working but that may lead to directional properties.

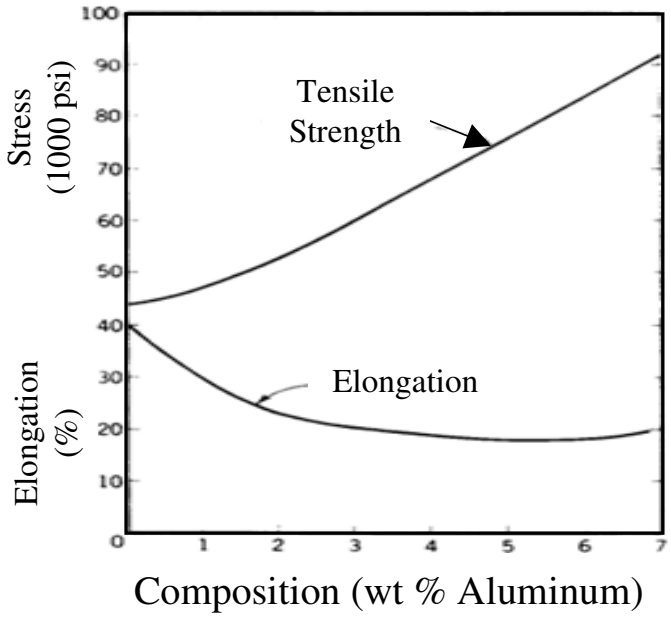

Figure 5.9 The Hardening Effect of the Addition of Small Amounts of Aluminum to Titanium [25].

Beta alloys have a room temperature stable phase of the body centered cubic structure. Vanadium, chromium and aluminum are the beta stabilizing elements. Figure 5.10 shows the increase in the beta phase stability with the addition of vanadium. An addition of only 4% of vanadium reduces the α-β transus temperature nearly 200°C. In case of bending and cold forming operations, beta alloys have inherent superiority over the alpha alloys with their BCC structure. Only Ti13V11Cr3Al is produced in large quantities.

Alpha-beta alloys are formed by the addition of controlled amounts of beta stabilizing elements to titanium. This results in the persistence of beta phase below the beta transus temperature, down to the room temperature. Two phase system of body centered and CPH and BCC crystal systems are observed. Three different types of microstructures can be obtained by changing the thermo-mechanical processing route; a fully lamellar structure, a fully equiaxed structure, and a duplex

or bi-modal microstructure containing equiaxed primary alpha in a lamellar alpha-beta matrix.

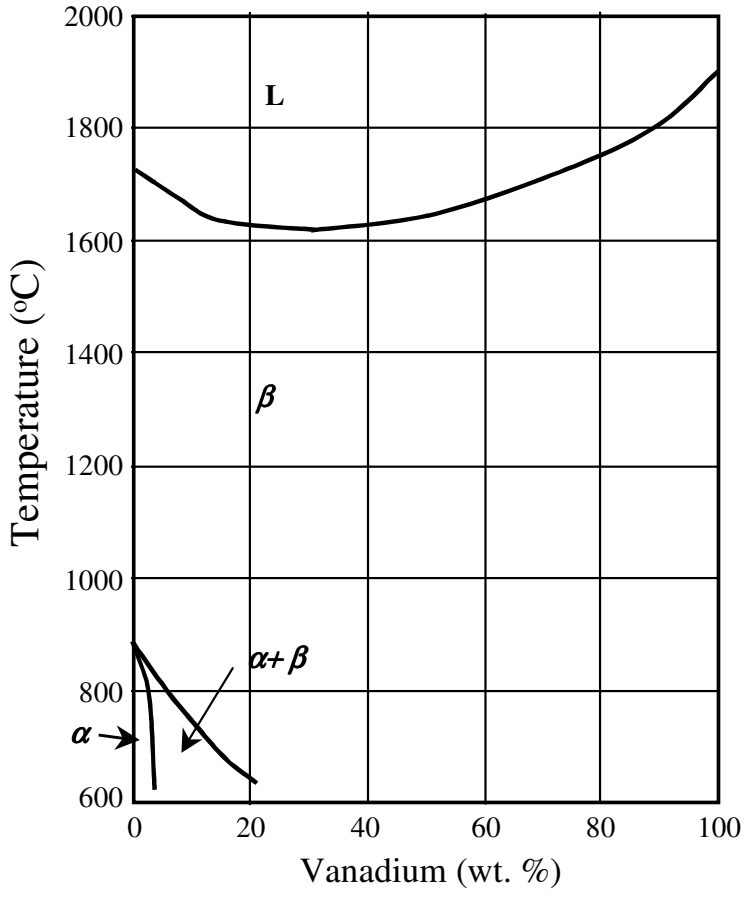

Figure 5.10 Effect of addition of vanadium (β phase encouraged)[25].

These two-phase alloys can be strengthened by quenching from some temperature in the alpha-beta range followed by an aging cycle at a lower temperature. While the properties of titanium alpha-beta alloys can be significantly improved by heat treatment and aging, the relative strengthening is much less than that obtained by heat treatment of steel and aluminum alloys.

The most of the alpha-beta alloys are weldable, but the joint ductility is somehow low. Also some of the alpha-beta alloys are welded by flash or spot-welded and a few are fusion weldable. The most important and widely used alpha-beta alloy is Ti6Al4V (which is also used in the experiments), and another one is

Ti6Al2Sn4Zr6Mo, which is mainly used for manufacturing of parts for advanced jet engines.

5.3.3 Properties of Ti6Al4V

Ti6Al4V is one of the most widely used titanium alloys, which accounts for more than 50% of all titanium tonnage in the world. It is especially used in aerospace industry, which leads to more than 80% of this usage. The next largest application of Ti6Al4V is medical prostheses, which accounts for about 3% of the whole market. The automotive, marine, and chemical industries also use small amounts of this alloy. As a result, in addition to its mechanical and thermal characteristics, the availability of this material is an important factor in selecting Ti6Al4V alloy.

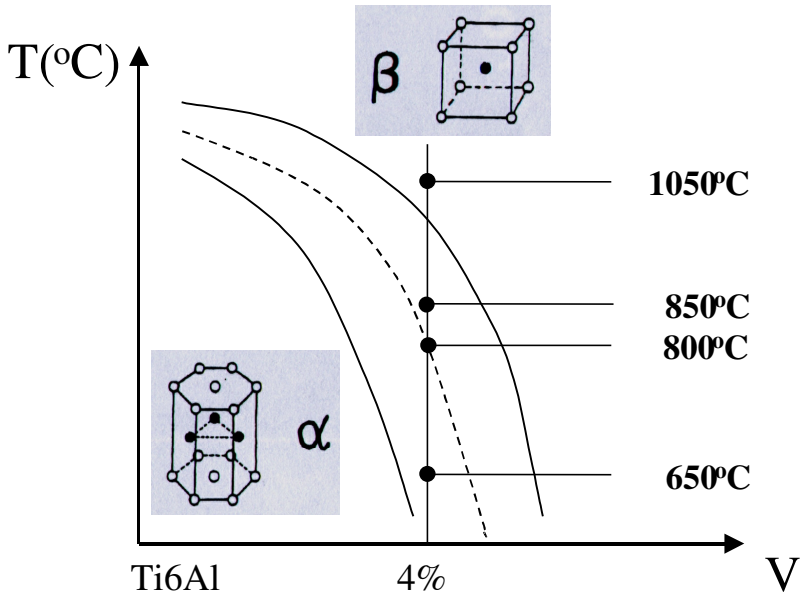

Figure 5.11 Microstructural properties of Ti6Al4V, related to Vanadium content

It is an alpha-beta Titanium alloy, which means that it contains both alpha and beta phases at room temperature. The alpha phase is similar to that of unalloyed titanium but is strengthened by alpha stabilizing additions (e.g., aluminum). The beta phase is the high-temperature phase of titanium but is stabilized to room temperature by sufficient quantities of beta stabilizing elements such as vanadium, molybdenum,

iron, or chromium. The schematic representation of pseudo binary phase diagram (Ti6Al – V) is given in Figure 5.11.

5.3.4 Heat Treatment Examples On Ti6Al4V

In order to comment on the experimental results of Ti6Al4V samples, some heat treatment applications are going to be examined in this section. The final microstructural compositions of the applications will be used to compare to the experimental results. For this purpose Ti6Al4V alloy is heated to three different temperatures (by taking the final microstructure into account) and then cooled fast (water quenched) and slow (furnace cooled) to the room temperature (Figure 5.12). The microstructure is examined after each application [27].

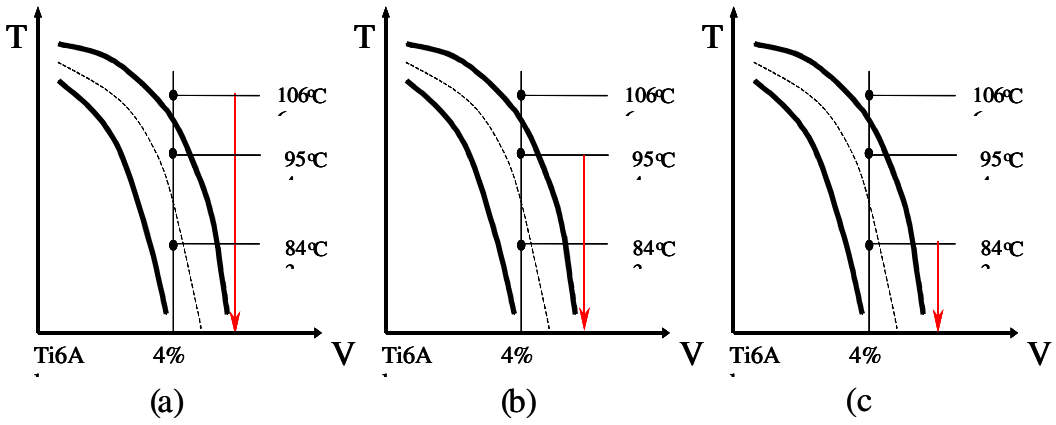

Figure 5.12 Schematic representation of heat treatment application examples Cooling from (a) 1066°C (b) 954°C (c) 843°C.

- *Cooling from 1066°C*: The material is first solution treated at 1066°C for 30 minutes. The initial microstructure of the material is a beta one. If the material is furnace cooled (slow), the microstructure turns to a mixture of alpha and beta structures, such that coarse plate-like alpha is formed whereas beta phase is retained and observed intergranularly (Figure 5.13a). In case of water quenching (fast cooling), titanium martensite is obtained (Figure 5.13b). The product may be tempered to obtain a mixture of alpha and fine beta. Ultimate

tensile strength is approximately 70 MPa higher for Ti-martensite when compared to the furnace-cooled result (1100MPa-1030MPa).

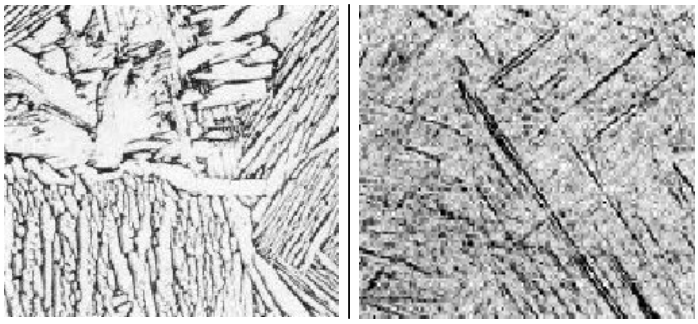

Figure 5.13 Microstructural views of samples that are (a) furnace cooled (b) water quenched from 1066°C

- *Cooling from 954°C*: The material is first solution treated at 954°C for 5 hours. This time the initial phase is a mixture of alpha and beta phases as it can be seen from Figure 5.11 and 5.12b. Again, if the material is furnace cooled (slow), a mixture of primary alpha and enriched beta is obtained (Figure 5.14a). This transformation may be simplified as:

$$\alpha+\beta \xrightarrow{\text{Furnace (slow) Cooling}} \alpha+(\alpha+\beta)$$

In case of fast cooling (water quenching), this time a mixture of primary alpha and titanium martensite is obtained (Figure 5.14b), which again can be transformed to the mixture of alpha and fine beta by tempering.

- *Cooling from 843°C*: The material is first solution treated at 843°C for 1 hour. The initial phase is again a mixture of alpha and beta. If the sample is furnace cooled (slow), the primary alpha-beta phase is preserved. On the other hand if the material is water quenched, mixture of alpha and retained beta phases occurs (Figure 5.15).

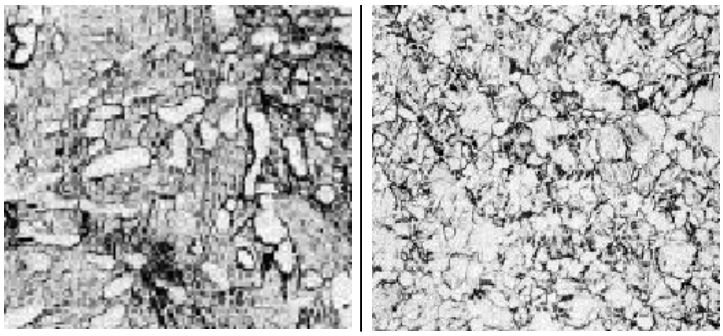

(a) (b)

Figure 5.14 Microstructural views of samples that are (a) furnace cooled (b) water quenched from 954^{o}C

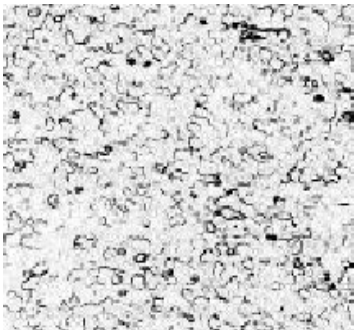

Figure 5.15 Microstructural views of sample that is water quenched from 843^{o}C

5.3.5 Microstructural Investigations

Before commenting on the experimental results it is important to identify the chemical composition of the material used throughout the experiments. As it is stated above, the material composition of Ti6Al4V may be different from sample to sample according to the interstitials. This affects the transus temperatures and mechanical properties, as a result the whole heat treatment strategy.

Ti6Al4V is produced in a number of formulations. Depending on the application, the oxygen content may vary from 0.08% to more than 0.2% (by weight), the nitrogen content may be adjusted up to 0.05%, the aluminum content may reach

6.75%, and the vanadium content may reach 4.5%. The higher the content of these elements, particularly oxygen and nitrogen, the higher is the strength. Conversely, lower additions of oxygen, nitrogen, and aluminum will improve the ductility, fracture toughness, stress-corrosion resistance, and resistance against crack growth. Table 5.2 shows the chemical contents of an ideal Ti6Al4V alloy and Table 5.3, the alloy used in the experiments.

Table 5.2 Standard chemical composition of Ti6Al4V

Element	Ti	Al	V	Fe	O
Weight -%	90	6	4	< 0.25	< 0.2

Table 5.3 Chemical composition of the experimental material (Ti6Al4V)

Element	Ti	Al	V	Fe	Si	Ni
Weight -%	90.7	4.9	4.2	0.15	0.02	0.02

As, it was previously explained in Chapter 4, before doing the forming experiments, about fifty laser-heating experiments are conducted, in order to understand and gain control over the laser heating parameters. In this part, the microstructural investigations of two of these results will be described.

Top, side and microstructural views of the first example, which is cut for processing, are given in Figure 5.16. This is a solid workpiece, which is laser heated in a whole circular path instead of a ring one. There exist no melting on the surface, but the heat penetrated until just below the heated surface. If the microstructure of the product is examined (Figure 5.16c), the titanium martensite region is clearly seen which is formed as a result of the rapid cooling (air cooling and water quenching were utilized in the experiments) from the elevated temperatures to the room temperature.

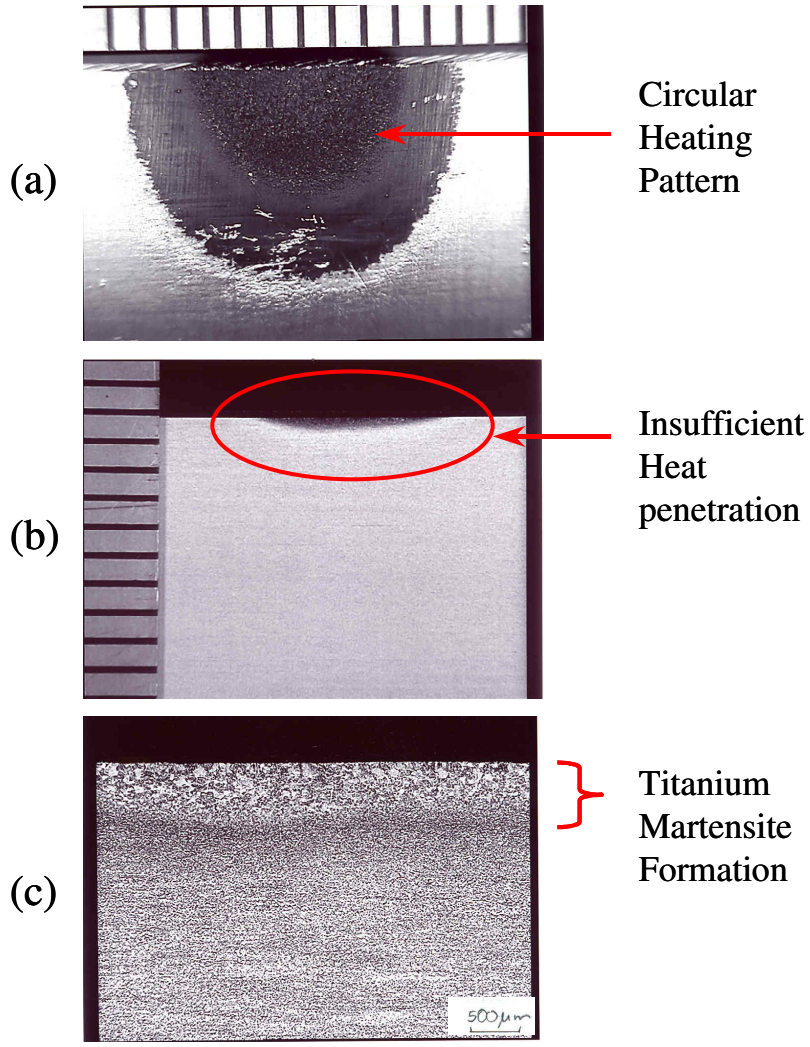

Figure 5.16 (a) Top (b) Side (c) Microstructural views of a laser-heated workpiece.

In the second example, a laser-heated hollow workpiece, which is heated with a ring shape profile, shown in Figure 5.17, is examined. The effect of ring shaped heating profile is clearly observed (Figure 5.17b). This time, because of the excessive heating melting is observed on the heated surface (Figure 5.17a, Figure5.17c). Again titanium martensite formation is observed due to the rapid air-cooling from elevated temperatures.

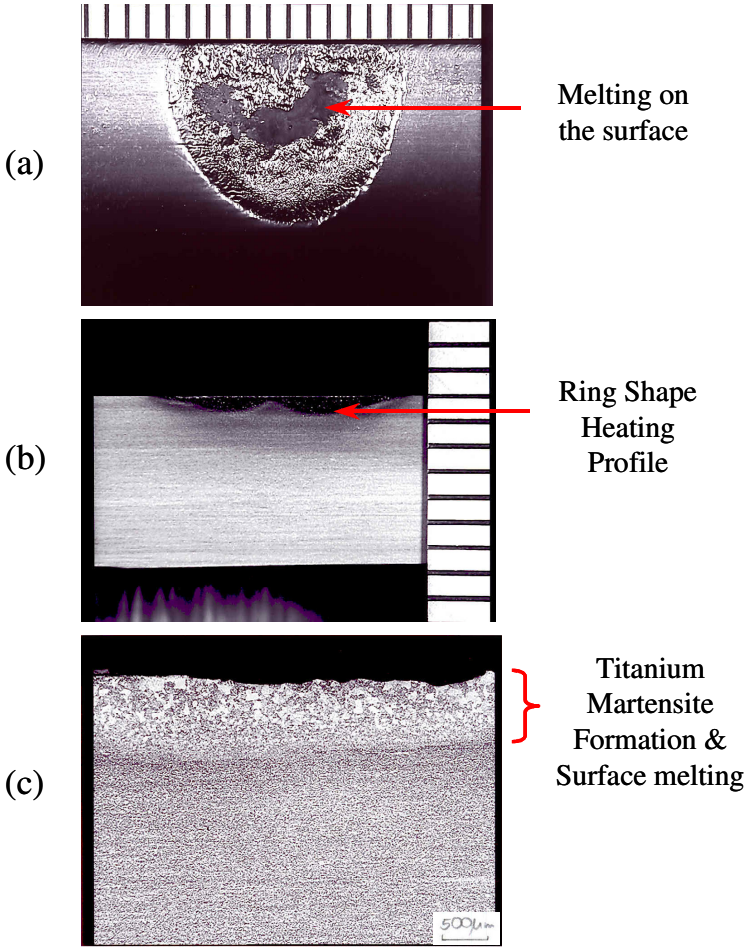

Figure 5.17 (a) Top (b) Side (c) Microstructural views of a laser-heated workpiece.

5.3.6 Hardness Values Of The Formed Workpieces

Regional hardness values of the formed workpieces are important in understanding the formation characteristics and determining the application areas. The subject experiment is "laser heating and forming experiment 37" (see Table 4.3). The heating curve of the workpiece is given in Figure 5.19, which is composed of the data collected by the pyrometer. 500 Volts and 4.1 J/s of energy are applied for the laser heating process. Hardness values of the formed workpiece are shown in Figure 5.18. The hardness study is carried out in two directions. It is important to note that, the maximum hardness value is obtained in the central region, which is explained in

Chapter 4. This is in fact not surprising, as there occurs a kind of cold forming in that region.

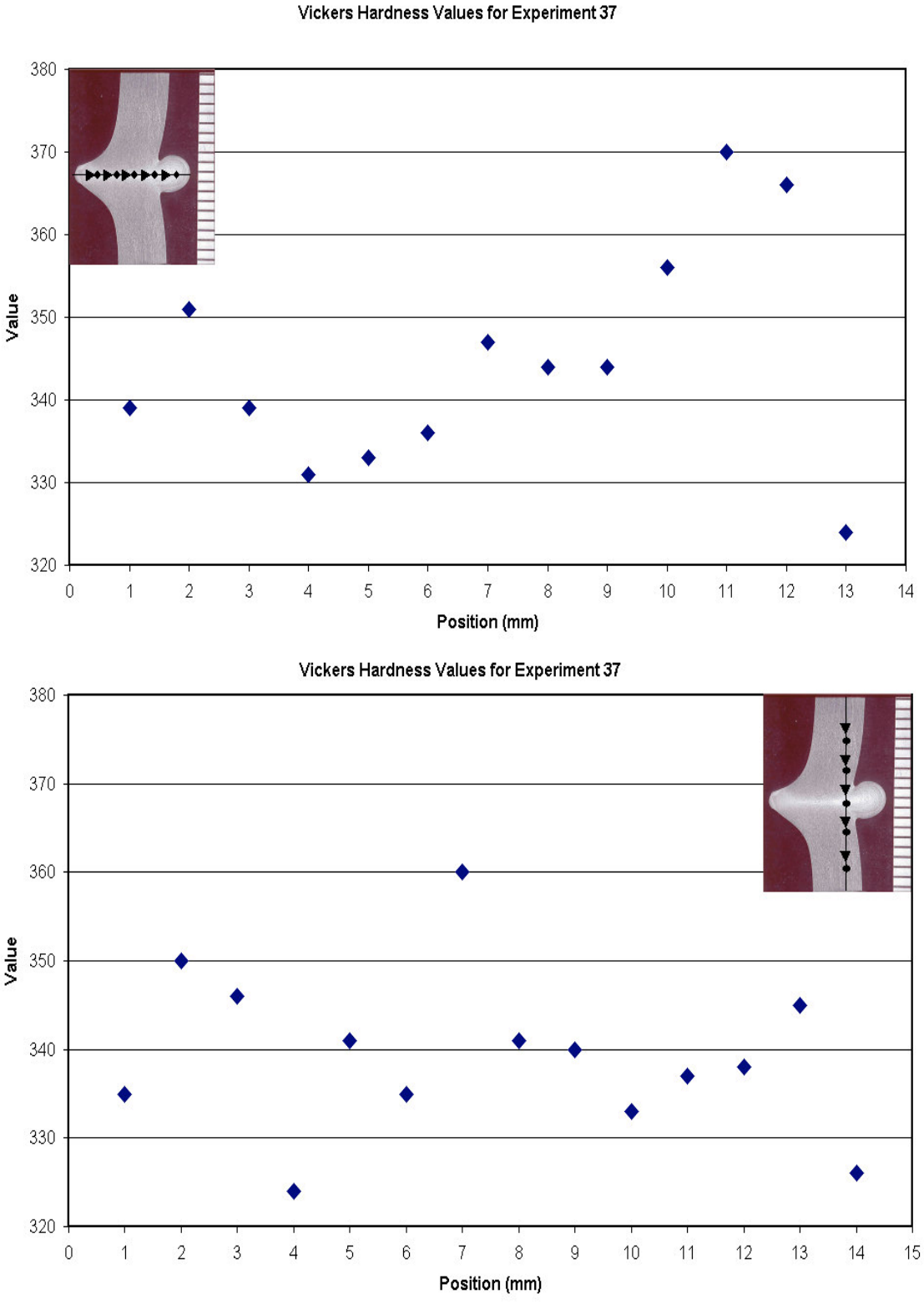

Figure 5.18 Hardness values of Experiment 37 in two directions.

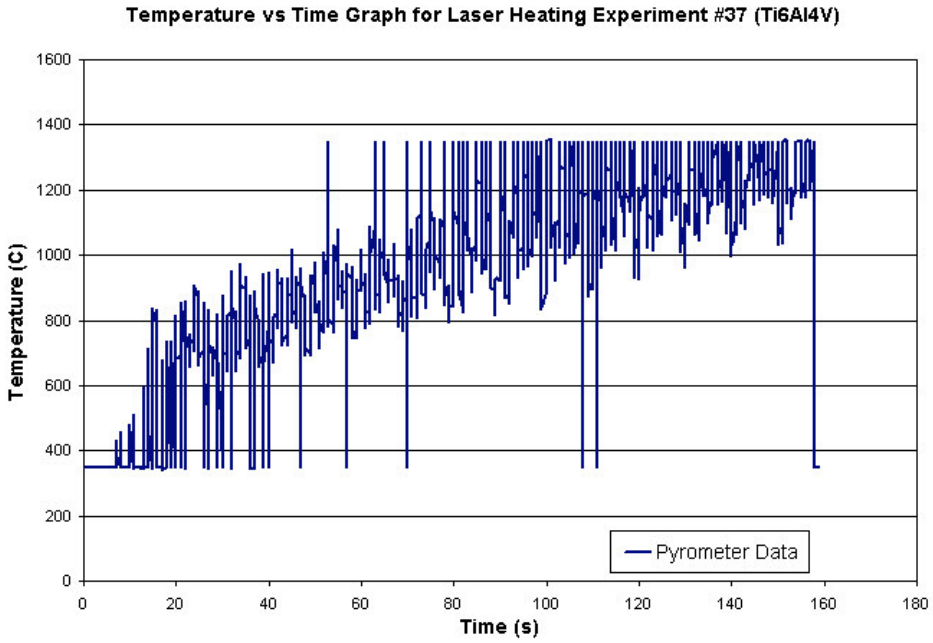

Figure 5.19 Heating curve of experiment 37.

Microstructural photographs of the same experimental result were taken from five different locations (Figure 5.20). There are two locations in the undeformed region (A&E) and three of them are in the locally laser heated and deformed region; one in the primary bulge region (B), one in the central region (C), and one in the secondary inner bulge region (D).

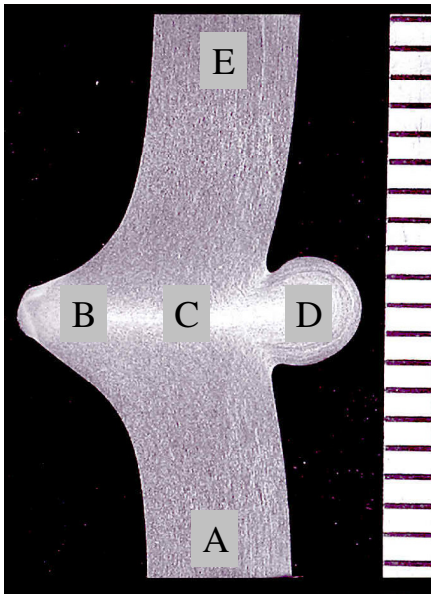

Figure 5.20 Microstructural investigation regions in Experiment 37

If the relative less heat-affected regions that are (A) and (E) are examined, similar structures are observed, as expected (Figure 5.21). These regions are expected to be in the temperature range of around 500°C - 600°C. The structure is an alpha-beta alloy structure, as the transition temperature of ~843°C is not exceeded; there occurs no phase transformation.

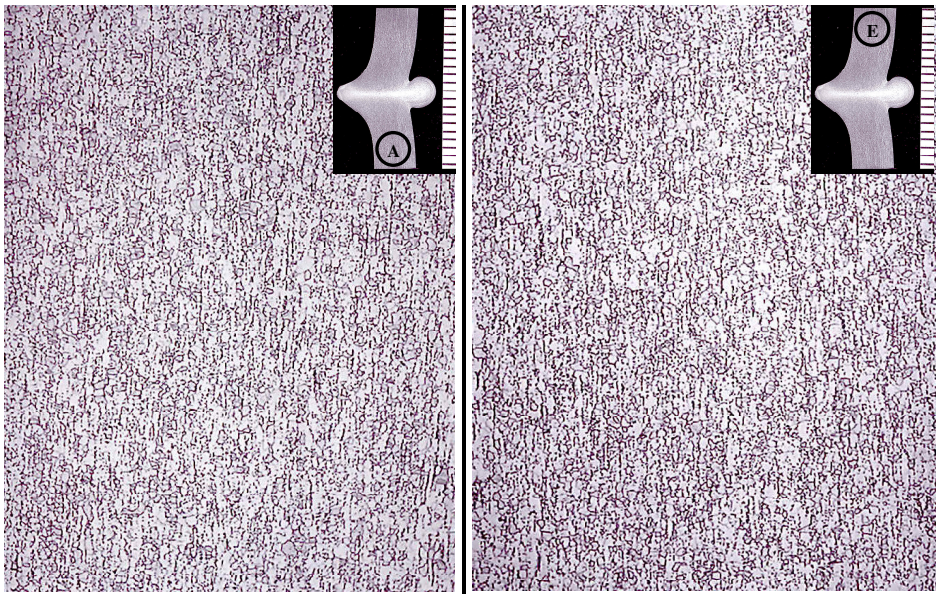

Figure 5.21 Microstructures in regions (A) and (E) (180X)

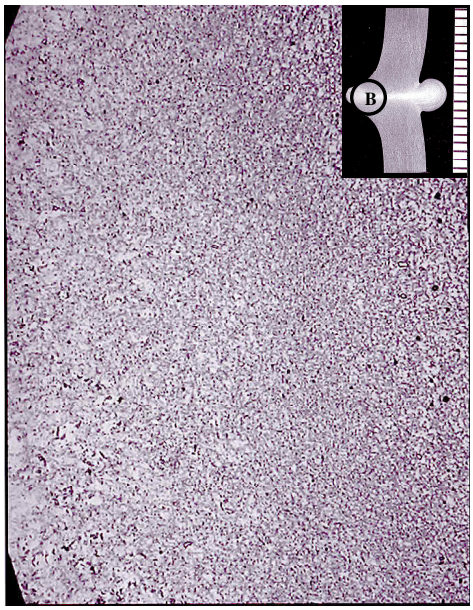

Figure 5.22 Microstructures in region (B) (180X)

The most important region that has to be carefully examined is the region (B), where the effects of local laser heating can be observed (Figure 5.22). As it can be seen in Figure 5.19, the temperature in the local heated region exceeds 1300^{o}C. This corresponds to the heat treatment example 1 shown in Figure 5.12. The Titanium martensite formation can be especially observed in the left side (from where the heat is applied). The growth of grain size in the inner regions shows the effective cooling on the heated side. On the other hand, the cooling rate is less in the inner region, which allows the formation of relatively smaller grains.

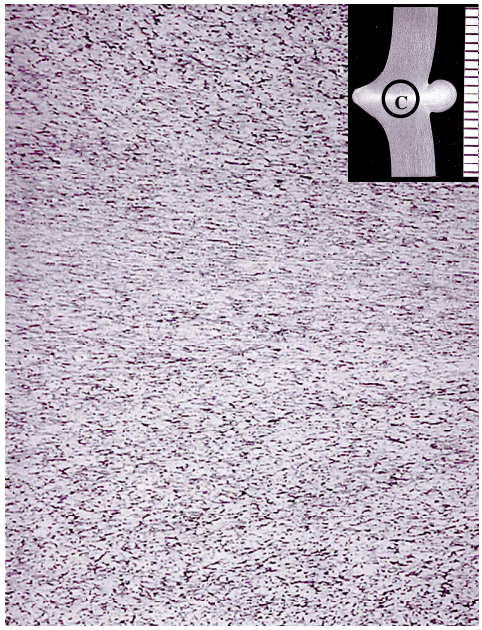

Figure 5.23 Microstructures in region (C) (180X)

In region (C), the most important characteristic that attracts the attention is the position of the grains. In especially the central region, the deformation of the grains shows the path of flowlines. The alpha-beta phase structure is observed in that region (Figure 5.23).

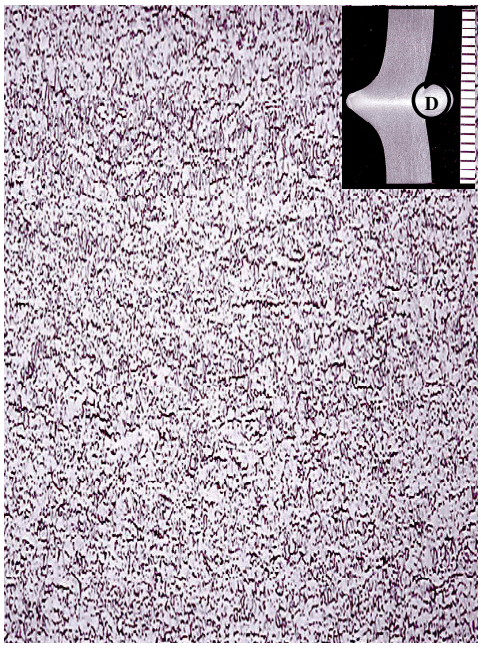

Figure 5.24 Microstructures in region (D) (180X)

Finally, in region (D), it is possible to observe approximately the same microstructure in regions (A) and (E). Again alpha-beta phase is observed (Figure 5.24). This secondary inner bulge region is relatively colder when compared to the regions (B) and (C).

5.4 Conclusions

The most important point that has to be taken into account is the variation of yield strength in different locations. This, in fact causes some difficulties in design applications. Prediction of these physical and metallurgical properties may be done by applying some analytical approaches, but in this thesis these properties are going to be calculated and compared by utilizing FEM in Chapter 7.

In the light of microstructural formations, it is possible to obtain or prevent hardened regions by modifying the heating and cooling rates applied in the process. This must be done by taking also the effect of forming into account.

Finally, surface melting must be considered carefully in selecting the laser heating parameters. The surface meting may be harmful to the equipment used in addition to the fact that the melted region shows poor surface characteristics and has a negative effect on the form of final shape. So, an optimum point that prevents melting but allows the heating of necessary amount of material.

CHAPTER 6

NUMERICAL MODELING OF THE PROCESS

6.1 Introduction

In finite element method, there are two points that have to be taken into account before modeling the problem by a commercial finite element code. First, the modeling strategy must follow a path such that the model represents the actual process the best. This point is realized by forming the geometrical constraints and applying the boundary and initial conditions as close to the reality as possible. On the other hand, there are situations, in which it is impossible or infeasible to model some features. This brings out the second point in finite element modeling, the economy. The finite element model should be as simple as possible, but without disregarding the process's requirements. This optimization results in a shorter computational time. In both of the cases, it is possible to obtain a "garbage-in-garbage-out" result if the model is not satisfactory. For this purpose in order to break the "black box" of finite element method, a brief explanation of the method is given in Chapter 3 in addition to the modeling details given in this chapter.

The finite element modeling of the process is composed of two separate parts as in the actual experiments; the local laser heating and the successive upsetting operation. The boundary conditions and the physics of the two parts are clearly different. This chapter will cover the modeling details of the two operations and finally the next chapter will present the results obtained from the finite element method. As it was previously mentioned, MSC/Marc 2003 and MSC/SuperForm were utilized as finite element codes. Both of the programs are based on the finite element method. MSC/SuperForm is a software specially designed for metal-

forming engineers based on MSC/Marc, a general purpose finite element software which allows the user to model electromagnetic, fluid, acoustic etc. applications. Being a more specialized program, MSC/SuperForm sets most of the parameters related with the metal forming as default. The experiments were designed according to the results of the finite element method application and furthermore, the limits of the process were inspected by applying the extreme values for some parameters, which were limited by the actual experimental setup.

6.2 Finite Element Modeling

In this section a sample model will be introduced through its mesh topology, the boundary and initial conditions applied, material definition, properties and definition of the contact bodies and the other necessary program inputs.

The sample model is used for simulating the laser heating and successive forming of a 60 mm long hollow workpiece with the inner and outer diameters of 16 mm and 30 mm, respectively. The heating procedure is composed of 4 concentric circles, the largest with the diameter of 8 mm. This procedure is repeated 25 times throughout the process (see Chapter 4 for heating procedures).

6.2.1 Mesh Topology

The finite element model of the sample specimen is composed of 23,547 elements, which are *type 7* (full integration, hexagonal, mechanical 3D element type) [16] and 27,408 nodes. Despite the fact that the body is geometrically symmetric it is not possible to model the problem as a symmetric one, because of the application style of the boundary conditions.

If the model is examined longitudinally, four different mesh geometries are observed (Figure 6.1); the two ends of the workpiece are modeled by coarse

elements in order to decrease the number of elements (consecutively to shorten the calculation time), as large deformations are not expected to occur there. Here the element edge lengths are 3 mm. On the contrary, the central region of the model is constructed from very fine elements. Two ideas lie behind this structure; first, to obtain 0.5 mm by 0.5 mm square surfaces for heat flux boundary condition applications and second, to simulate the local form more precisely as main deformation takes place in this locally heated region. Another different mesh structure is constructed between these two regions as a transition region from the finer mesh to the coarse mesh. The element edge lengths are 1.5 mm in this region. Finally, a very thin layer of elements is constructed at the lower end of the body. This *dummy layer* is required to fix the body in the 3-D space (will be explained in the next chapter in more detail).

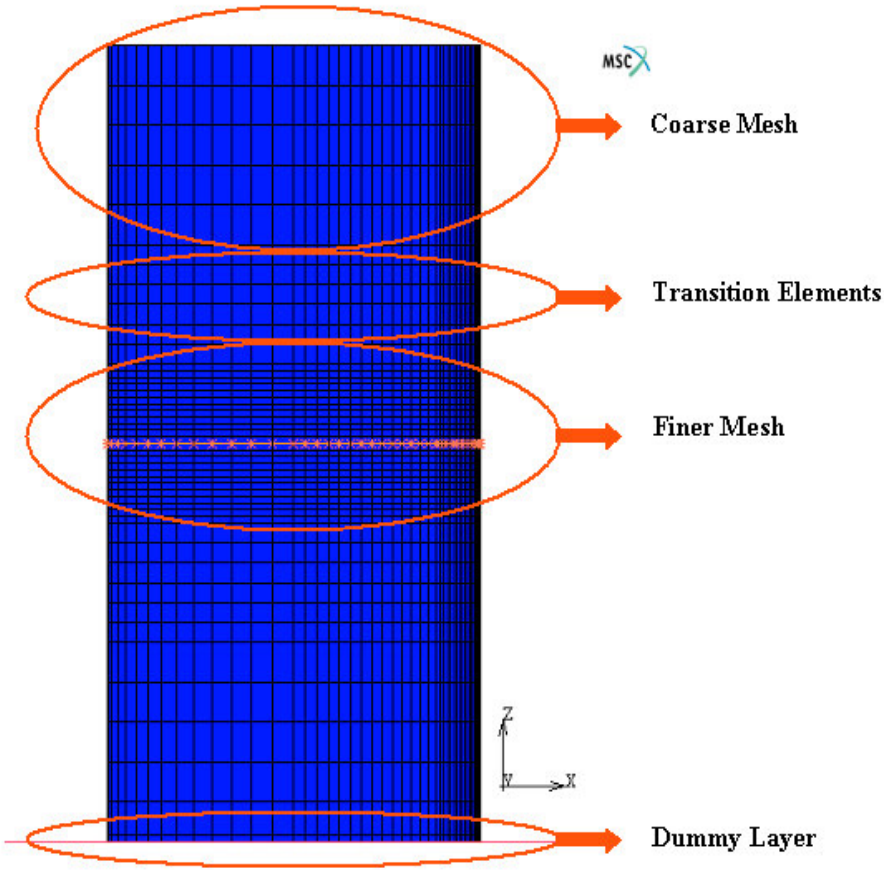

Figure 6.1 Different mesh layers of the modeled body

If the cross section of the model is inspected, again different mesh structures are observed (Figure 6.2). The frontal side of the model is constructed with finer elements in order to produce 0.25 mm^2 areas for surface heat flux boundary conditions and to simulate the deformation better. Whereas, the backside is again composed of more coarse elements in order decrease number of elements used and to shorten the calculation time. Here, an important point has to be taken into account. Minimum number of elements through the wall thickness should be three in order to model the behavior of bending (Figure 6.3). Each element will be correspondent to one state of stress such as tension, neutral and compression during bending.

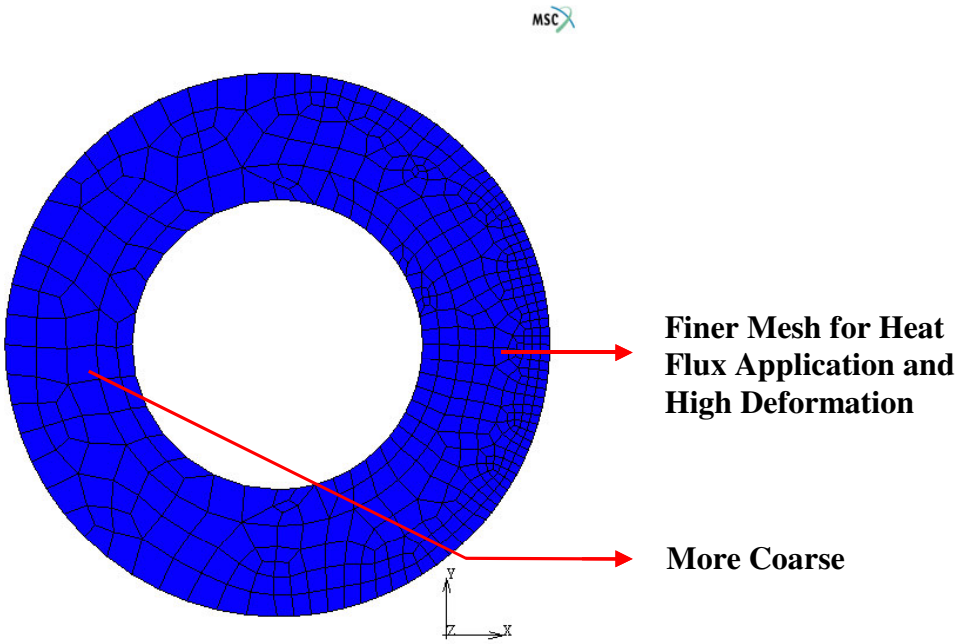

Figure 6.2 Mesh structure in the cross section of the body.

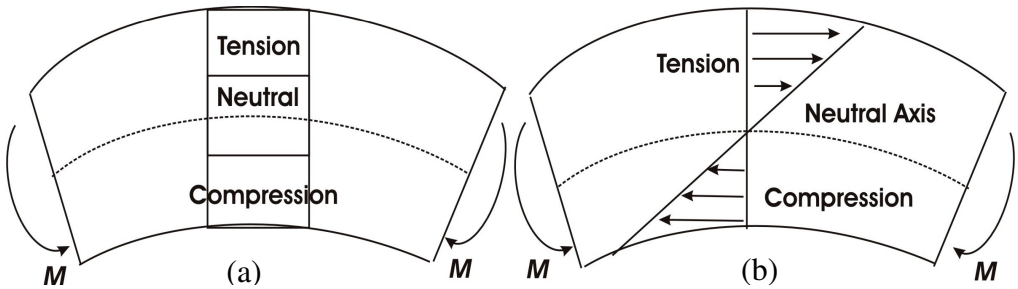

Figure 6.3 Bending behavior in simulations (a) and actual case (b)

6.2.2 Application of Initial and Boundary Conditions

The only initial condition of the problem is related with the temperature. The workpiece is modeled to be at the room temperature (at 25^{o}C) at the beginning of the calculation, which was in fact the real case. This initial temperature is applied to the nodes of the mesh structure.

Two different types of boundary conditions, which are very important in modeling the real problem, are applied. These are *fixed displacement boundary conditions* and *heat flux boundary conditions*. In fact, the fixed displacement boundary conditions are applied at the thin layer of elements constructed in the mesh structure. This layer is used to give the displacement boundary conditions of the problem to fix the body in the space (Figure 6.4). The body is fixed by restricting the movement in *x* and *y* directions on the two axes. This is not done directly at the lower end of the body, as there occurs confusion between the boundary condition given and the boundary conditions of the lower die. As a result a thin layer of elements is modeled (which is 0.5 mm away from the end of the body) and the displacement boundary conditions are given inside of the body.

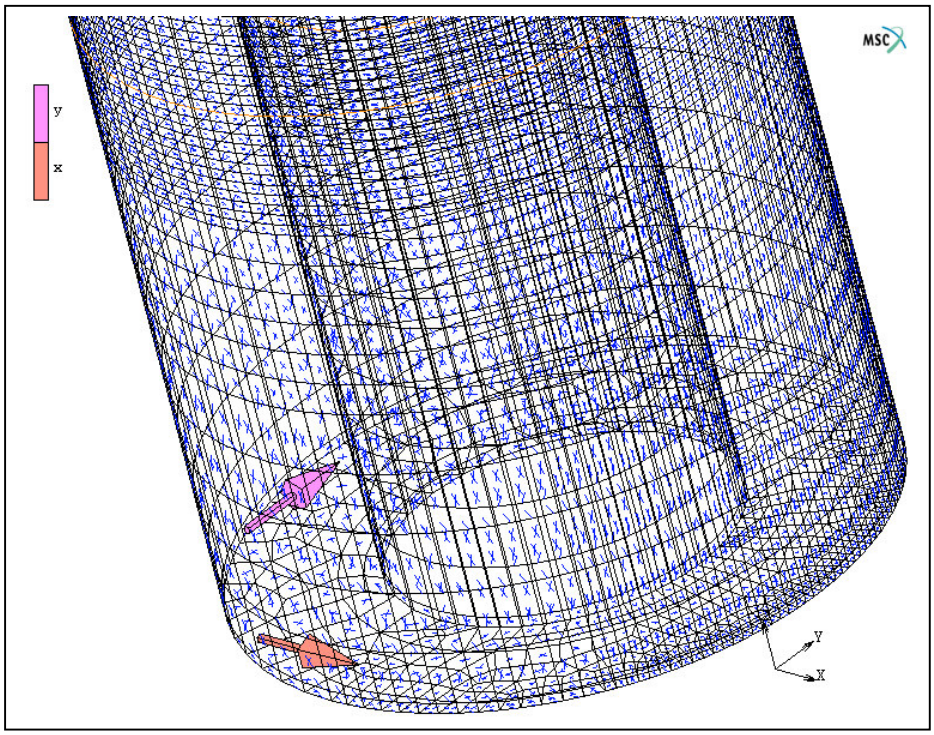

Figure 6.4 Displacement boundary conditions of the model

In order to model the laser heating, some assumptions have to be made. These assumptions are related to the shape of the heating profile applied by the robot arm, and the model of the laser spot. In Chapter 4, the heating profile is described as a ring shape composed of concentric circles but in finite element modeling, because of the structure of the elements it is not possible to create a perfect circular heating path. Instead, the heating profiles are designed to be parallelograms on the finite element model (Figure 6.5). Each heating circle is represented by a separate parallelogram. In addition to this, as circular elements does not exist in finite element method, the laser spot, which is in fact a circle, is modeled by using the combination of square surfaces with the edge lengths of 0.5 mm. The heat flux boundary conditions are given by using point flux or surface flux options. Both of the cases are acceptable, if the flux values are correctly set. A conversion between these two styles can be given as (for only one heating surface):

$$\begin{aligned} \textit{Heat Input} &\equiv \textit{Surface Heat Flux} \times \textit{Flux Area} \\ \textit{Heat Input} &\equiv \textit{Point Flux} \times \textit{Number of Nodes on the Area} \end{aligned} \tag{6.1}$$

This idea is proved by utilizing the two-dimensional axisymmetric analyses and presented in Section 6.3.

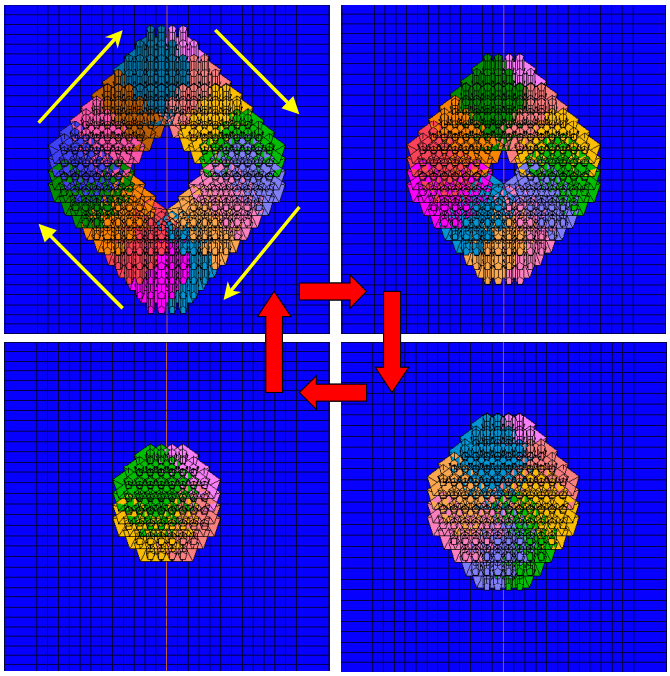

Figure 6.5 Four parallelograms representing the four concentric heating circles

Forty surface heat flux boundary conditions are applied for this sample problem, each are activated one by one by the help of the timetables given. Only one surface heat flux boundary condition is activated at a time, which represents the laser beam position at the corresponding time interval. As the laser beam moves to another position after a while the previously activated surface boundary condition is deactivated and the next boundary condition at a different position (neighbor of the previous one) is activated for the corresponding time interval. After the completion of the last boundary condition of a heating circle (or the parallelogram), the first boundary condition of the inner one activates. By this way, all of the boundary conditions are activated (and then deactivated) and one cycle is completed after the completion of the last boundary condition of the innermost circle. Afterwards, the first boundary condition of the outermost circle is activated and the second heating cycle starts. As a result the whole movement of the laser beam is modeled. Figure 6.6 shows the heat propagation characteristics of the sample model.

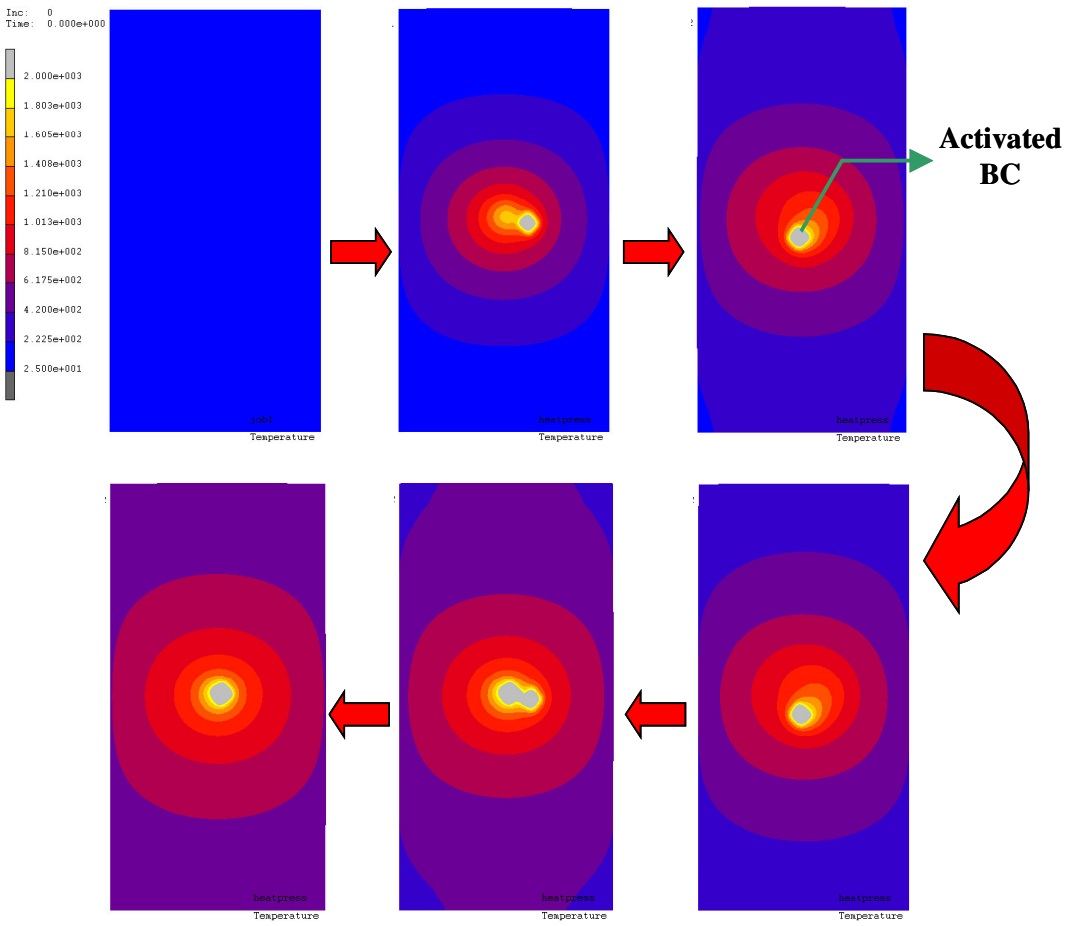

Figure 6.6 Propagation of heat in the workpiece body

6.2.3 Material Properties, Contact Bodies & Program Inputs

In order the mesh topology to have a physical meaning, material properties have to be assigned to the elements. The material properties are assumed to be isotropic for the modeling. Mass density, Young's modulus, Poisson's ratio and the thermal expansion coefficient are the main mechanical properties given as input data. Elastic-plastic material assumption is applied (explained in Chapter 3). In addition to this thermal properties such as thermal conduction coefficient and specific heat are given as functions of temperature for more accurate modeling. These material properties are given in Appendix A.

Contact bodies must be defined as a last step in the finite element modeling. For this purpose, the dies are defined as rigid bodies, whereas the workpiece is modeled to be a deformable body with the material properties given above (Figure 6.7). One of the dies is modeled as a fixed body, which in fact represents the upper die in the actual case. On the other hand, the lower die is modeled to have a speed of 3.6 mm/s.

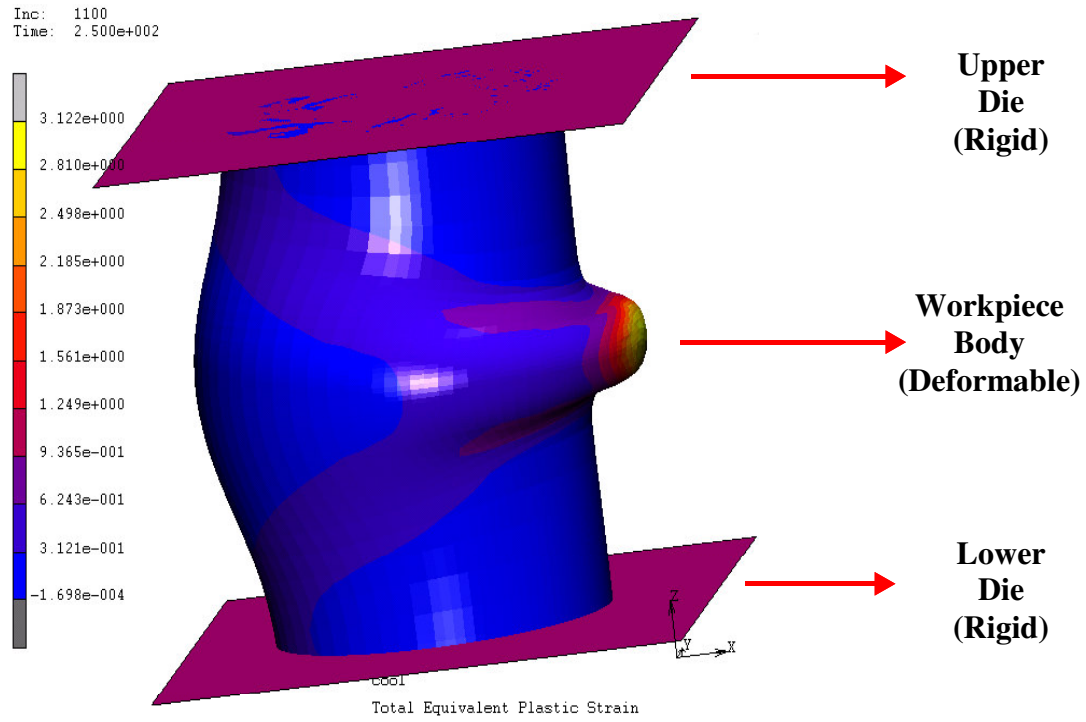

Figure 6.7 Contact Bodies

The friction coefficients are applied to the contact surfaces between the dies and the workpiece. Except for the parameter study, the friction coefficient is given as 0.06 (Coulomb), which is found by applying the ring compression test for two different material types. The initial dimensions of the ring compression test specimens are given in Figure 6.8. The tests are conducted at the room temperature. The same value can be directly used in the simulations because the two ends of the workpiece and the dies are relatively colder as a result of the local heating characteristics. The experimental data is plotted together with FEM simulation result (Figure 6.9). The relative sliding velocity is set as 1.0 in the simulations (see Section 3.11). After the heating period is completed, the workpiece is upset.

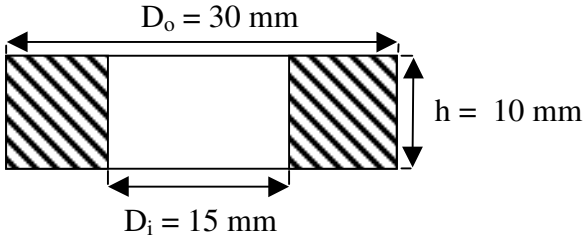

Figure 6.8 Initial dimensions of the ring compression test specimen

In the calculation part of the problem, a coupled quasi-static analysis is done in which residuals or displacements are taken into account as the convergence criteria. Relative force \ displacement value of 0.1 is used in the calculations. As it was stated in section 3.10, this is done by taking the ratio of maximum residual force to the maximum reaction force (or the ratio of maximum displacement of the last iteration to the actual displacement change of the increment) into account. As a result Equations 6.2 and 6.3 are satisfied. Full Newton-Raphson iterative procedure is applied together with large-strain assumption.

$$\frac{\left\| F_{residual} \right\|_\infty}{\left\| F_{resident} \right\|_\infty} < 0.1 \tag{6.2}$$

$$\frac{\left\| \partial u \right\|_\infty}{\left\| du \right\|_\infty} < 0.1 \tag{6.3}$$

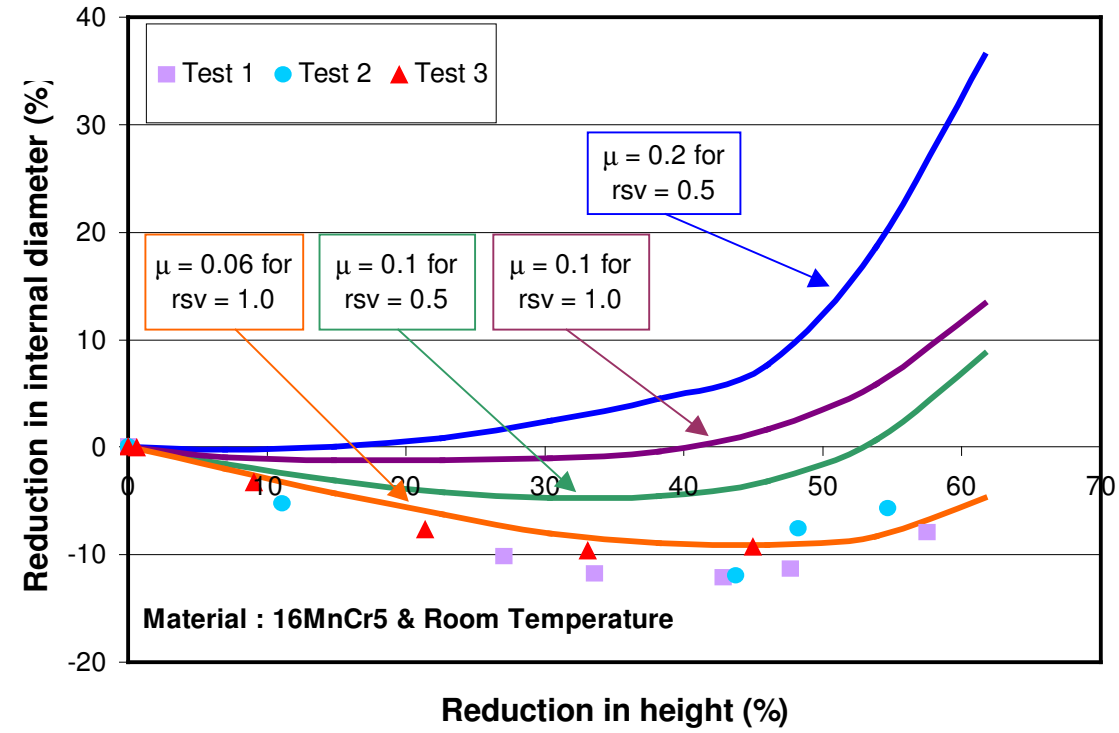

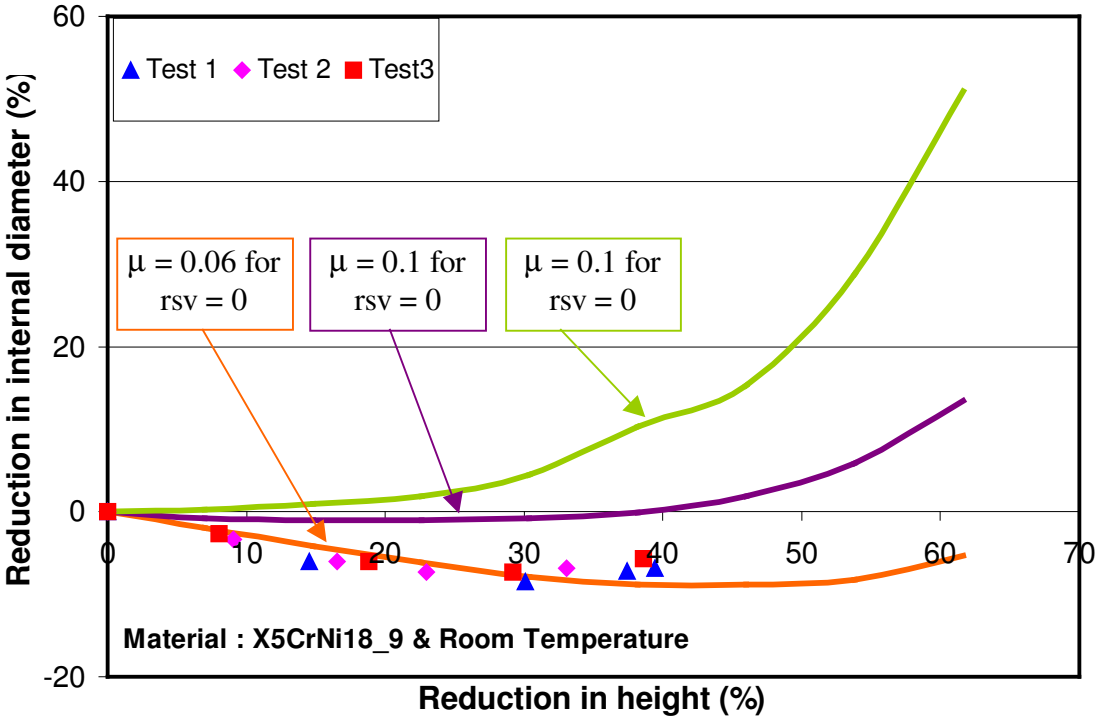

Figure 6.9 Friction Coefficient study through ring compression tests

6.3 Two Dimensional Finite Element Analyses

In the very beginning of the study two dimensional finite element method applications were carried out in order to get accustomed to the computer program package and to better understand the concept of the project. These preliminary applications are 2-D axisymmetric models, which cover both heating and forming analyses.

As it is stated in Section 6.2.2, it is possible to apply both point flux or edge flux boundary conditions in order to simulate the heating characteristics provided that Equation 6.1 holds. In order to prove this conversion circumferential heating is applied on a 2-D axisymmetric model as shown in Figure 6.10. The test specimen is selected to have the length of 30 mm and the diameter of 10 mm. The model, on the other hand is constructed by utilizing the elements with the edge length of 0.625 mm. As it was shown on the figure, edge flux boundary conditions of 5000 mW/mm^2 are applied to the edges of 5 elements. These 5 elements are enclosed by 6 nodes, which form the locations for point flux application. The inner four nodes are shared by two adjacent elements, which brings together the requirement of the factor 2. The exterior two nodes belong to only one heating edge for each. As a result if the total energy is taken into account and Equation 6.1 is applied, the point flux can be calculated approximately as;

$$Q_P \text{ x } \textit{Number of nodes} = Q_E \text{ x } \textit{Total Edge Length}$$

Where

Number of Nodes = 10

Total Edge Length = 5 x 2 x π x 5 x 0.625

Q_E is given as 5,000 mW/mm^2 then

$$Q_P \approx 50{,}000 \text{ mW} \tag{6.4}$$

After the application of the two types of heat flux boundary conditions, the results are compared. For this purpose final temperature data (at the surface, internal region and the center) between the two edges of the model is plotted for both of the cases

(Figure 6.11). The maximum temperature value is obtained in the middle as expected. The temperature data of the two cases fit to each other, which proves the interchangeability of the two modeling approaches.

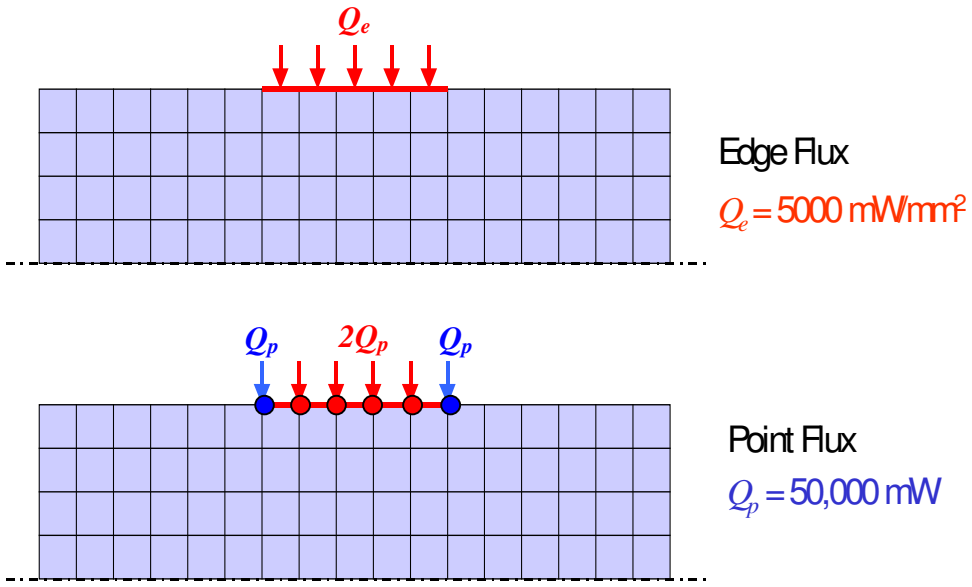

Figure 6.10 Two different heating approaches for a 2-D axisymmetric model

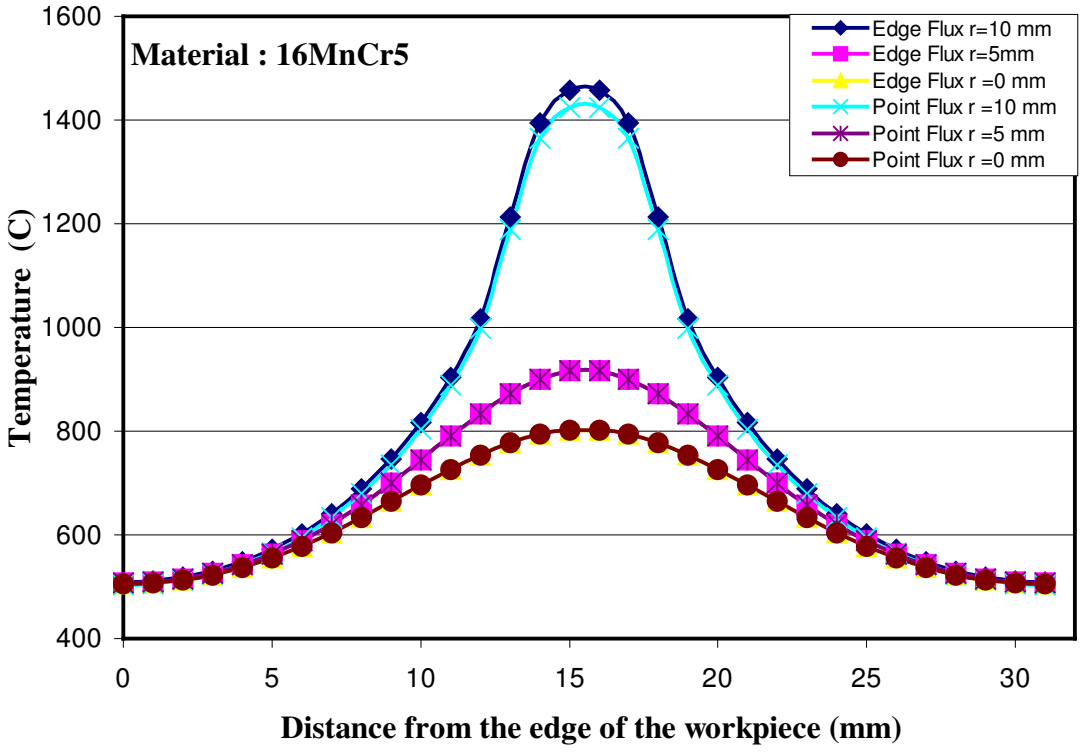

Figure 6.11 Comparison of point and edge flux approaches

Apart from the heating simulations, some preliminary applications on the forming characteristics were done in order to obtain a starting point for the experiments and 3-D FEM simulations. Figure 6.12 shows that the amount of the heat energy applied to the specimen have a direct effect on the final geometry. The meaning of the trend to the value 1 in the ratio of deformed to undeformed diameters is that, the most of the deformation is realized in the locally heated zone, which is in fact the desired case. In this group of simulations, an ideal, frictionless upsetting case is designed. The final diameters of the test models are measured and the graph is drawn. For this particular case, it can be concluded that; in order to obtain a local formation on the body, more than 800 W of heat energy is required to be applied for 10 seconds. The less the energy is, the more homogenous is the deformation on the body.

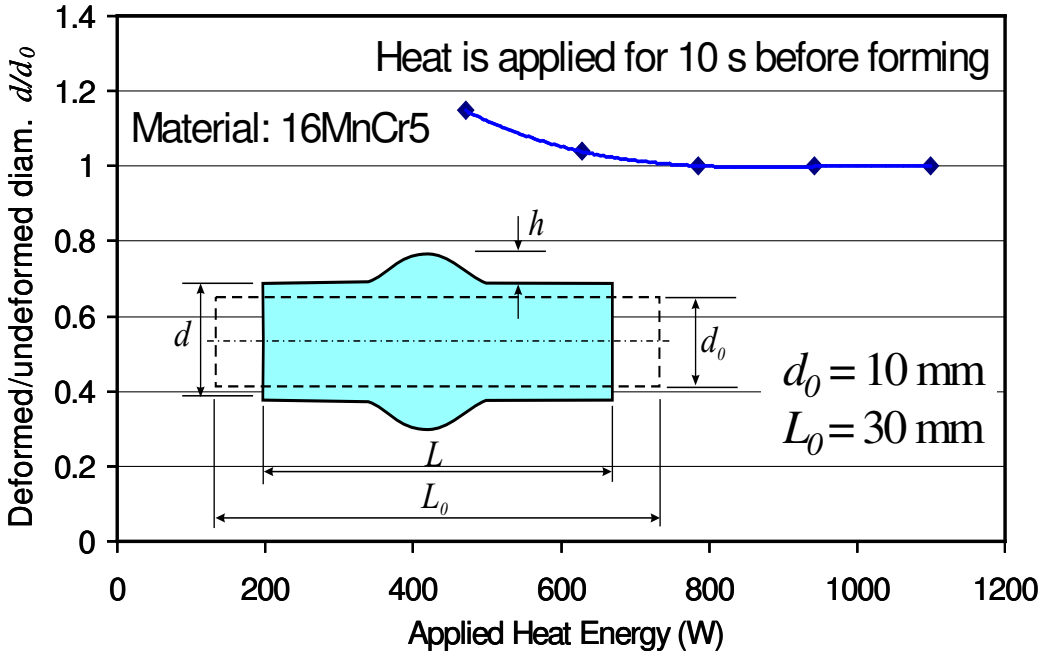

Figure 6.12 Effect of heat energy on the deformation characteristics

Another 2-D study on deformation behavior is done to investigate the effect of the initial geometry. For this purpose, the initial length or the initial diameter of the workpiece is kept constant and the other parameter is gradually changed (Figure 6.13). The ratio of final height of the local bulge to the final radius of the specimen is observed to decrease as the ratio of initial radius to the initial length of the specimen increases. Buckling behavior of the specimen is not taken into account in

the axisymmetric 2-D simulations; therefore the results must be interpreted carefully.

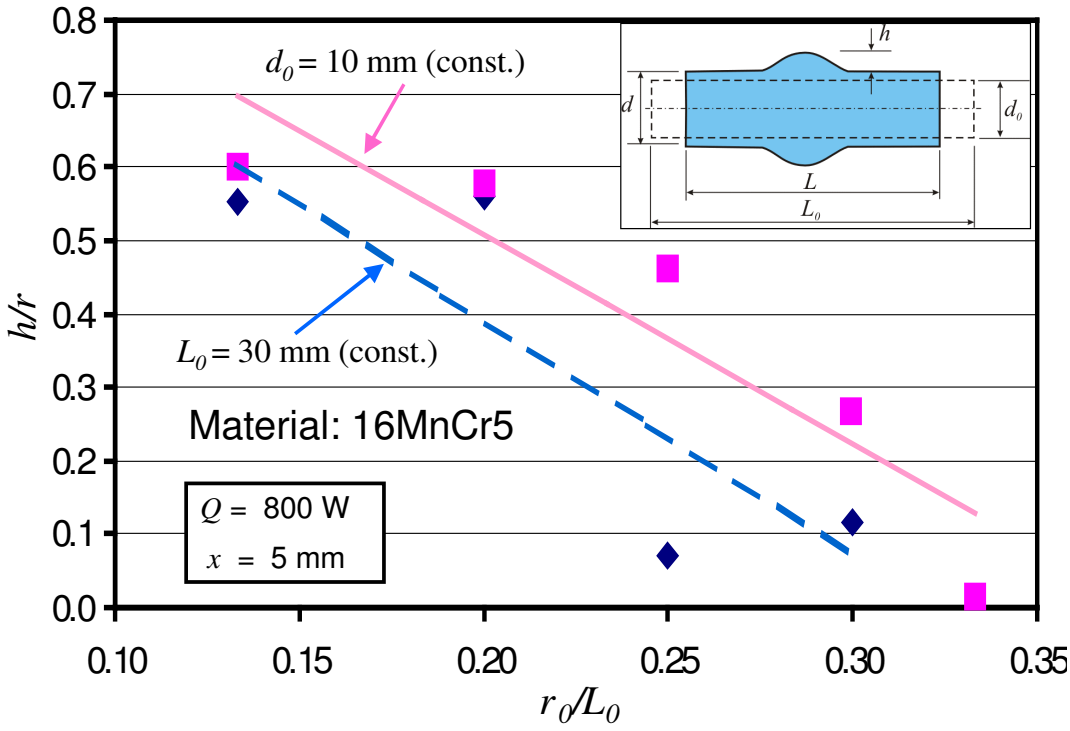

Figure 6.13 Effect of initial geometry on the final local form

6.4 Three Dimensional Finite Element Analyses

The 3-D simulation of the laser heating and successive forming application is done according to the principles given in Section 6.2. As it was stated, the modeling of the laser beam has great importance in the modeling of the simulation. The area of the laser beam is given as 1 mm^2 theoretically, but the heating effect of the laser beam would be larger than this value, as there may be deflections in the laser position or size. This fact is better shown in Figure 6.14, where the diameter of the heating area of the laser beam is shown as 5.45 mm. As the main problem in the finite element modeling of the process is the concentration of high amount of energy on a very small area, this physical situation can be modeled in the simulation by increasing the surface heat flux area and decreasing the value of the flux.

The concentration of the heating energy on a very small area causes the *"excessive deformation"* error in the FEM computer package MSC/SuperForm. This is because of the fact that the elements, which are subjected to the heat flux, tend to suddenly expand as a result of thermal expansion characteristics. The thermal expansion is directly proportional to the increase in the temperature. On the contrary, the surrounding elements stay at a relatively much lower temperature, which restricts this expansion behavior and a contradiction arises. In order to avoid this numerical difficulty, the thermal expansion characteristics is limited as if melting occurs at a certain temperature. For this purpose, four different heat expansion models are created [28]. Three models include dominant thermal expansion characteristics up to 300°C, 500°C and 700°C, whereas one of them simulates a "non-thermal expansion" case (Figure 6.15). Above these particular temperature values, the thermal expansion coefficient is decreased to 1 % of its initial value. The effect of this application is examined through two different beam area models (Figure 6.16) and three different total surface heat flux values of 30,000 J/smm^2, 40,000 J/smm^2.

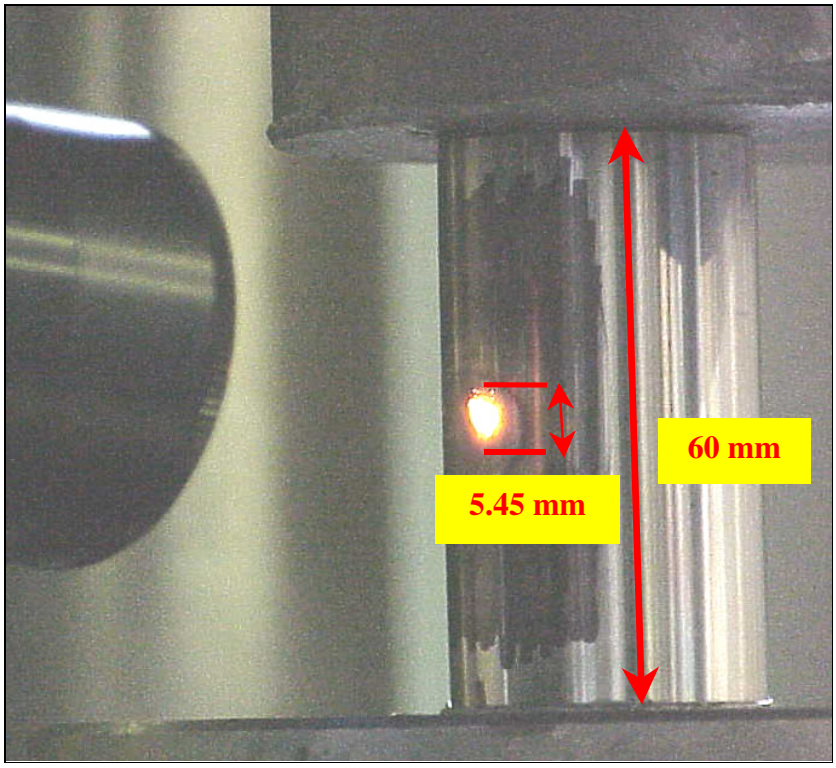

Figure 6.14 Heat affected zone of the laser beam

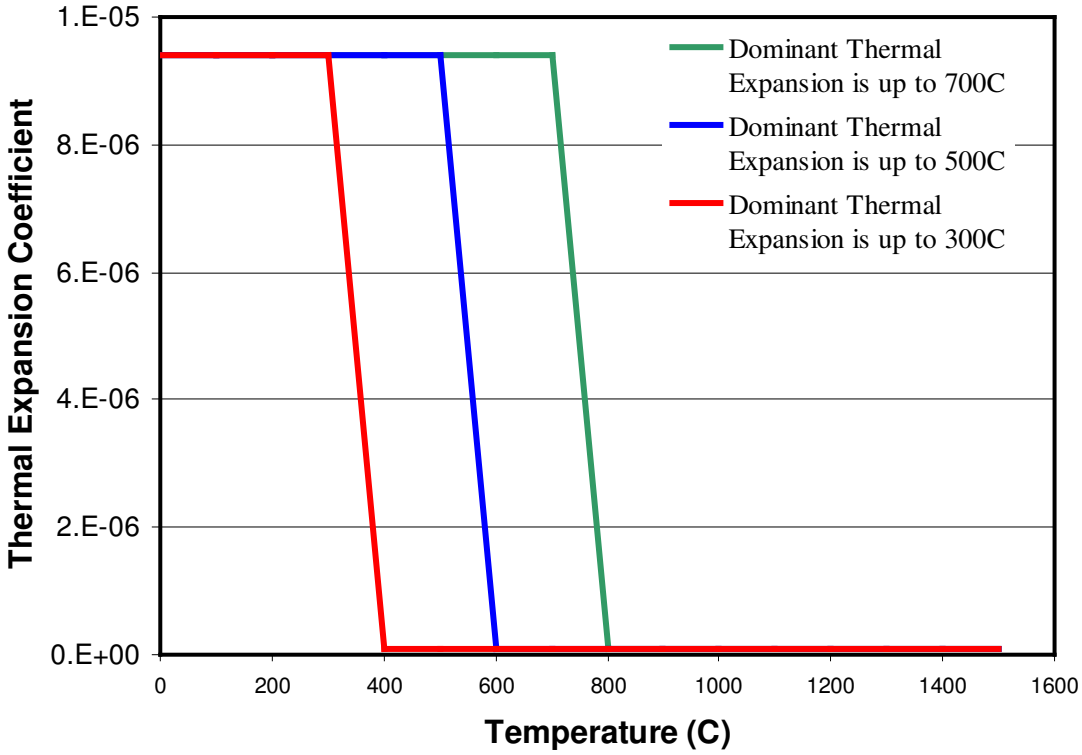

Figure 6.15 Thermal expansion models, showing the dominant thermal expansion coefficient temperature ranges.

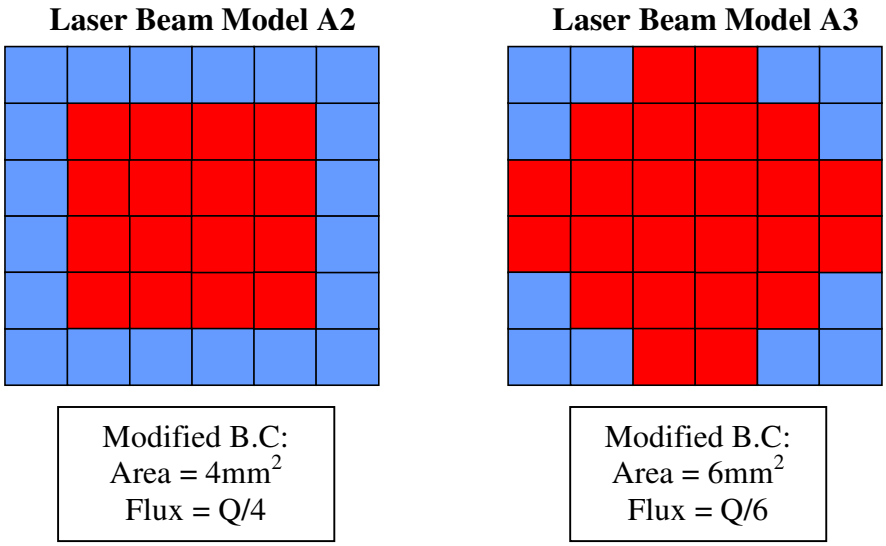

Figure 6.16 Two different laser beam models

The results of the different FEM simulations were compared in longitudinal direction on the surface and along the wall thickness inside the specimen (Figure

6.17), in order to find out, if the thermal expansion models are acceptable or not. For this purpose total equivalent plastic strain, equivalent stress and bulge geometry data are collected and plotted for different applications.

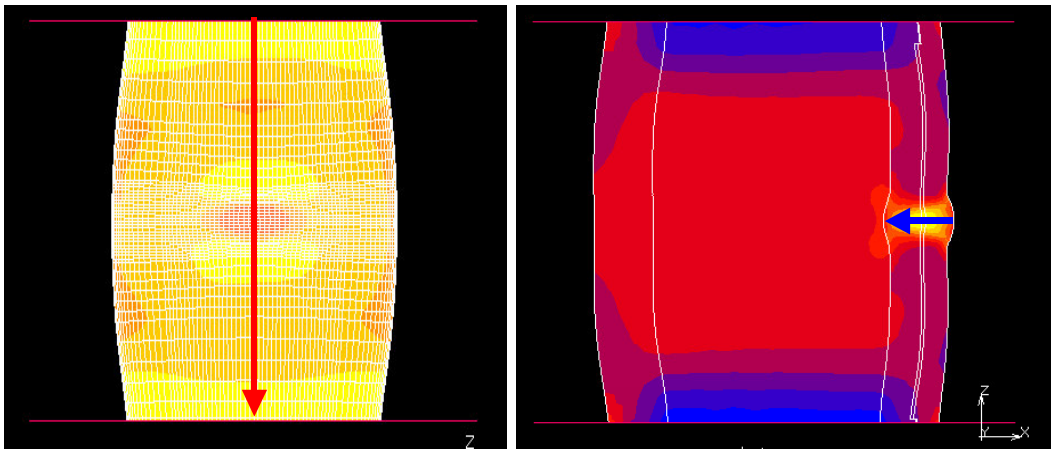

Figure 6.17 The data is collected from two different paths.

The results of the simulations with the laser beam area model A2 and the flux value of 30,000 J / s mm^2 in longitudinal direction are shown in Figure 6.18. The maximum error is observed in the equivalent plastic strain values, which is about 20% in the central region. In addition to this, the bulge size is less for the no-thermal expansion case, which is in fact an expected result.

The same comparison is done by increasing the heat flux value to 40,000 J/smm^2 and changing the laser beam model to a larger one (model A3). The characteristics of the selected variables of three different thermal expansion models are shown in Figure 6.19. The equivalent stress has approximately the same distribution in all of the cases, whereas the total equivalent plastic strain and the profile of the local form show deviations of up to 25% from the no-thermal expansion case, which is beyond the limits of an acceptable model.

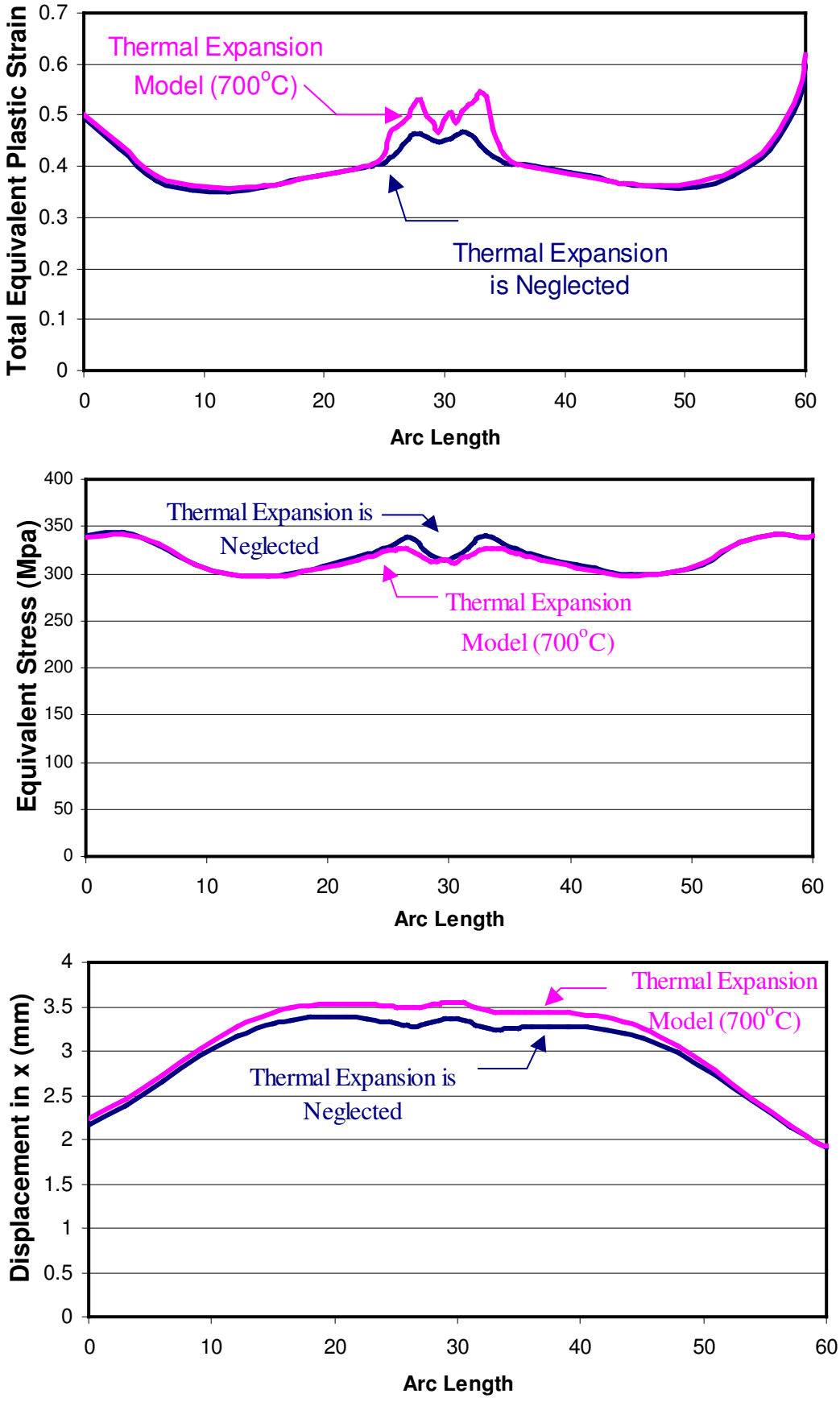

Figure 6.18 Results for Q = 30,000 J/smm^2 and laser beam model A2

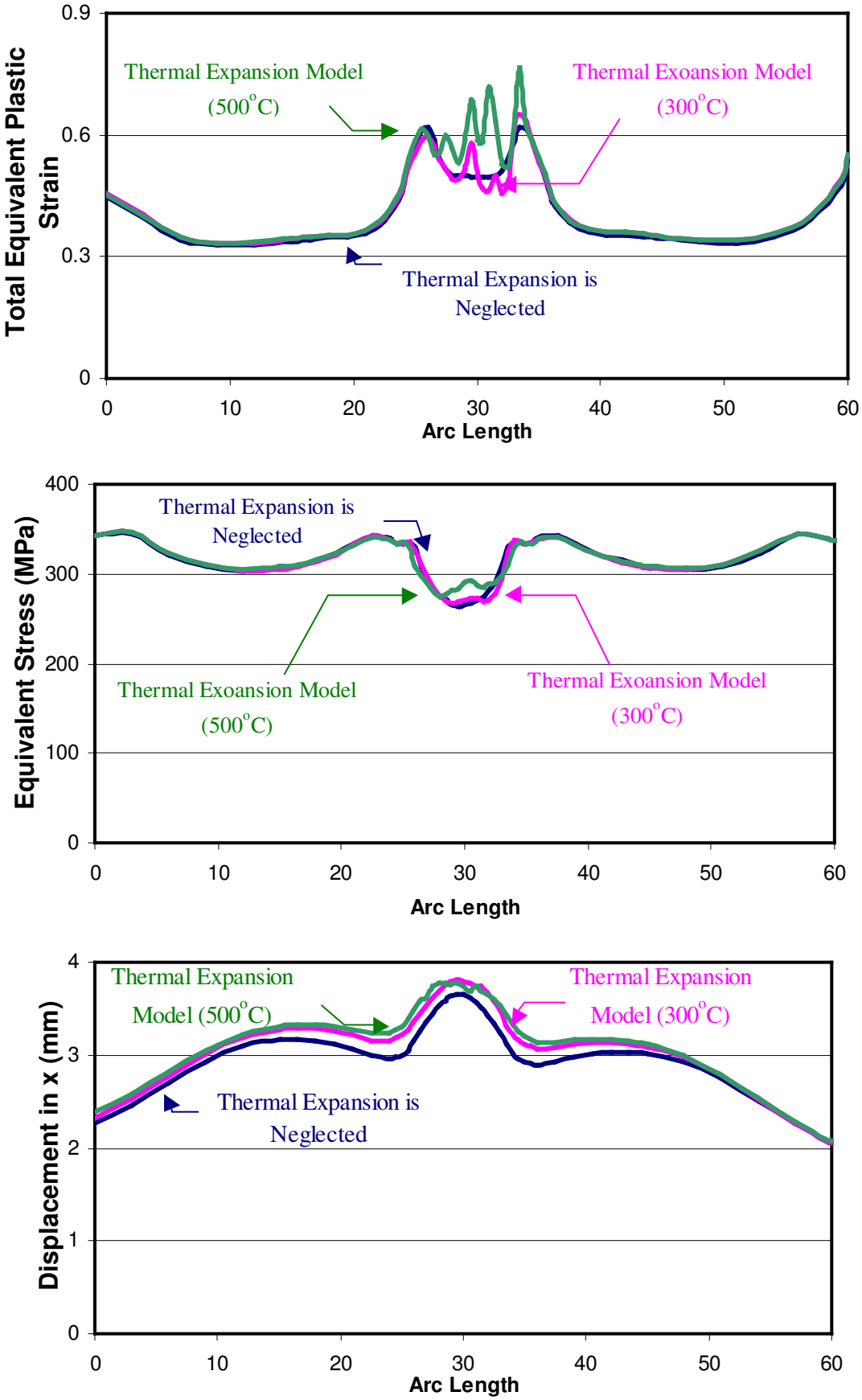

Figure 6.19 Results for Q = 40,000 J/smm^2 and laser beam model A3

Apart from the investigation on the surface of the test model in the longitudinal direction, equivalent stress and total equivalent plastic strain distributions are examined in the locally formed region inside the material. Again surface heat flux values of 30,000 J/smm^2 and 40,000 J/smm^2 are applied on the laser beam models A2 and A3 respectively. Figure 6.20 and Figure 6.21 show that the stress and strain characteristics of the thermal expansion and non-thermal expansion models are approximately the same along the wall thickness of the test specimen.

In the light of the results of the simulations, the models, in which the thermal expansion is neglected, have approximately the same equivalent stress distribution with the thermal expansion models in the longitudinal direction and along the wall thickness. The maximum error between the data of the two approaches is in the order of 5%. From this point of view the no-thermal expansion models are acceptable, on the other hand, the maximum error values reach 20% if the total equivalent strain and the local bulge profiles are compared. As the final shape of the product is the main criterion for the simulations, neglecting the thermal expansion behavior may lead to the unsatisfactory simulation results, even if the computational time is approximately 4 times longer (approximately 6 hours for a non-thermal expansion and 24 hours for a model with thermal expansion characteristics) for a model with thermal expansion characteristics (for MSC/SuperForm, 1.8GHz, 512Mb of RAM). This is better explained by simulating a real experiment (Experiment 85) with the no-thermal expansion assumption models. For this purpose six different laser beam area models with the areas of 1 mm^2, 4 mm^2, 6 mm^2, 9 mm^2, 16 mm^2, and 25 mm^2 together with the corresponding heat flux values are applied. Seven different measures (Figure 6.22) that specify the final product are compared with the simulation results (Table 6.1).

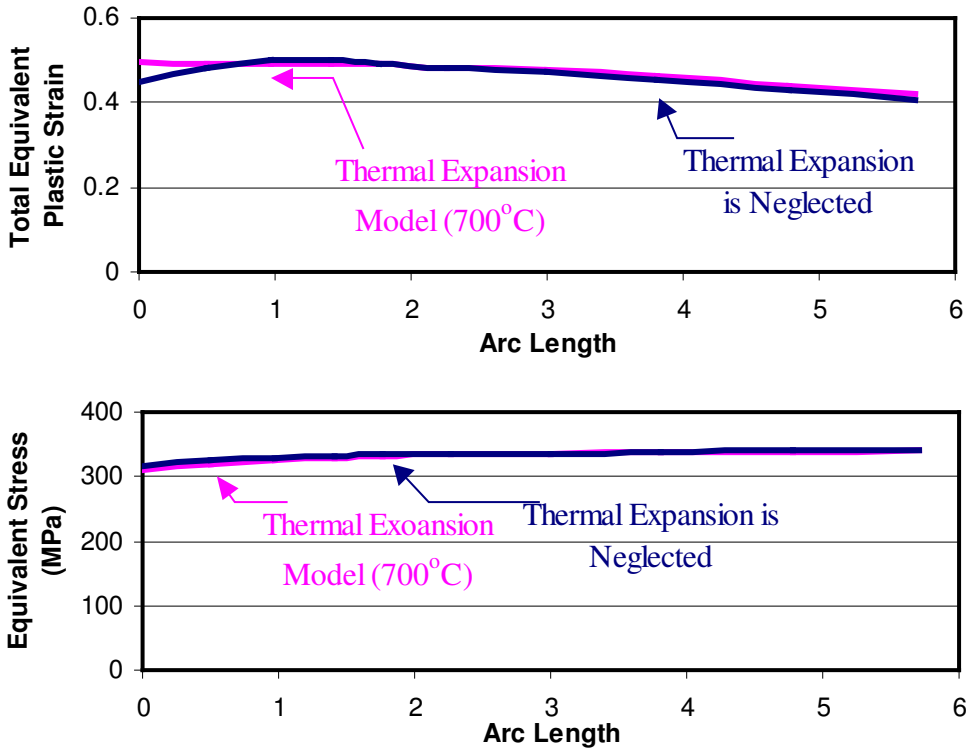

Figure 6.20 Results for Q = 30,000 J/smm^2 and laser beam model A2

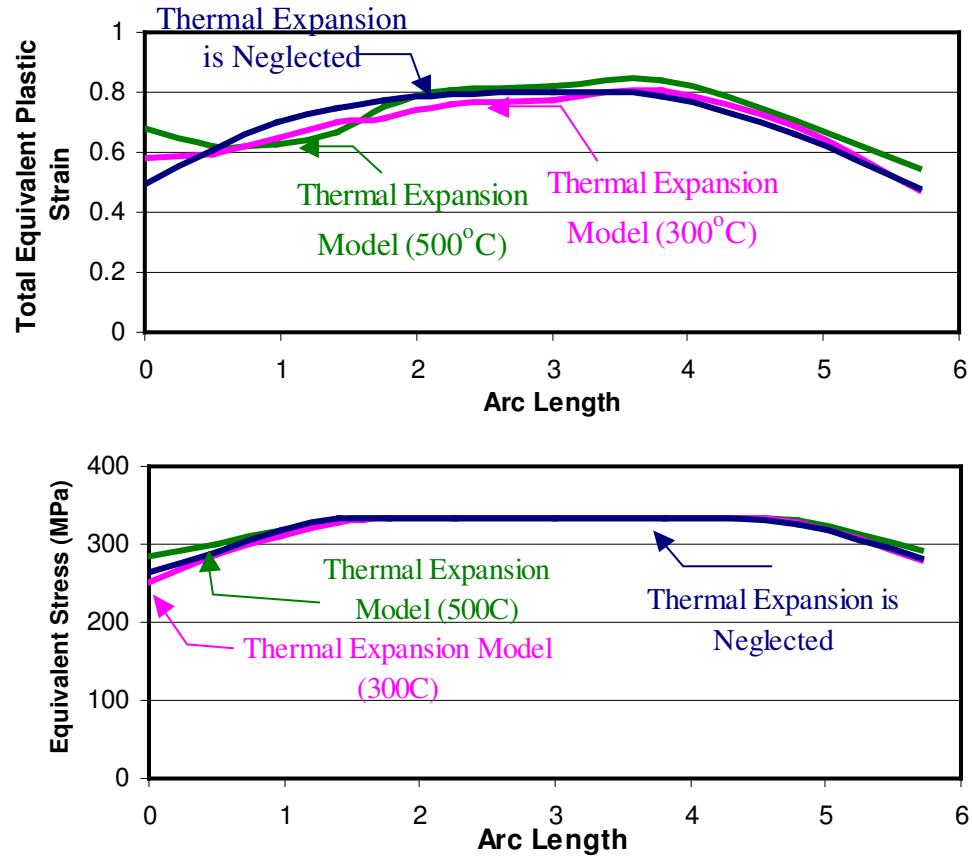

Figure 6.21 Results for Q = 40,000 J/smm^2 and laser beam model A3

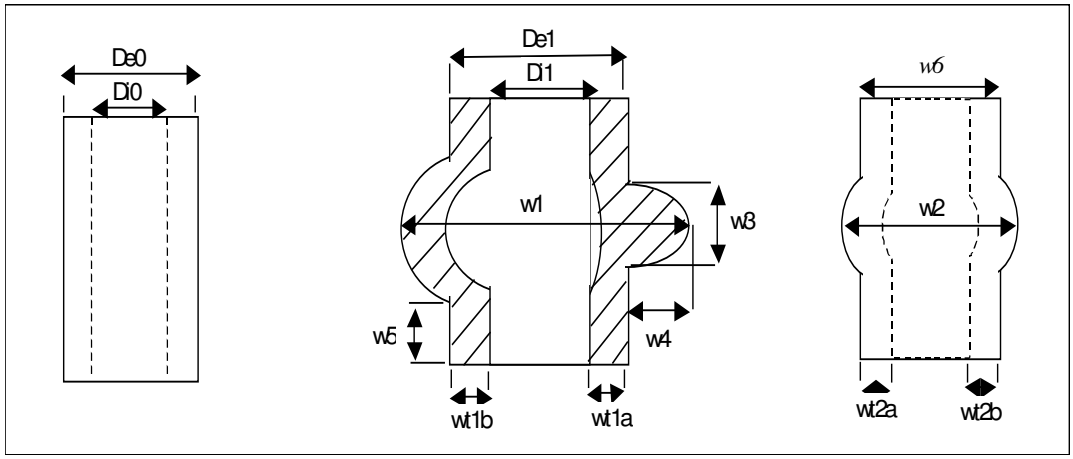

Figure 6.22 Measurement positions

Table 6.1 Specific measures of the experiment and the simulation results.

LHEXP 85	**d_{e0}**	**di_0**	**L_0**	**d_{e1}**	**d_{i1}**	**L 1**	**w1**	**w2**	**w3**	**w4**
Experiment	**30**	**16**	**60**	**30.99**	**15.85**	**43.58**	**41.53**	**41.83**	**9.23**	**5.54**
A1	30	16	60	33.82	17.72	43.57	37.17	37.23	10.36	2.46
ERROR %	0.00	0.00	0.00	-9.13	-11.80	0.02	10.50	11.00	-12.24	55.60
A2	30	16	60	34.52	17.95	41.57	38.72	38.37	9.36	3.3
ERROR %	0.00	0.00	0.00	-11.39	-13.25	4.61	6.77	8.27	-1.41	40.43
A3	30	16	60	34.33	17.93	41.57	38.76	38.29	9.4	3.1
ERROR %	0.00	0.00	0.00	-10.78	-13.12	4.61	6.67	8.46	-1.84	44.04
A4	30	16	60	34.37	17.95	41.57	38.35	38.37	9.47	2.85
ERROR %	0.00	0.00	0.00	-10.91	-13.25	4.61	7.66	8.27	-2.60	48.56
A5	30	16	60	34.35	17.94	41.57	38.39	38.25	9.47	2.77
ERROR %	0.00	0.00	0.00	-10.84	-13.19	4.61	7.56	8.56	-2.60	50.00
A6	30	16	60	34.37	17.94	41.57	38.18	38.33	9.58	2.73
ERROR %	0.00	0.00	0.00	-10.91	-13.19	4.61	8.07	8.37	-3.79	50.72

The results of the simulations are unsatisfactory with the maximum errors in the order of 50%, which is unacceptable. This behavior shows the danger of neglecting the thermal expansion characteristics of the problem. But on the other hand, the

problem cannot be solved by utilizing the current finite element package. The following possible solution approaches may be considered;

- A much more *finer mesh structure* can be constructed. The current model is composed of about 27,000 elements, which makes the solution slow and furthermore high capacity is required for the computers. The finer mesh solution seems to be not economical for the simulations.
- *Modifications on the laser beam models* maybe considered but table 6.1 shows that the laser beam area does not have a strong effect on the final product shape.
- *Density of the material – temperature* relation can be set but this is not allowed by the current computer package.
- *Modifications in the solution parameters* are done such as, changing the element type of the model, the convergence criteria, number of solution increments or the solution procedures (direct solution and iterative methods). But no solution is obtained.
- *An advanced general purpose finite element tool* can be utilized to simulate the complex nature of the laser heating instead of the specific one, which is designed for metal forming applications. For this purpose the toughest question, in which the thermal expansion coefficient is given as a constant value and no melting behavior is modeled in MSC/Marc 2003. The solution is completed in seven days. The results of the measurements are given in Table 6.2 and Table 6.3. The error values obtained are concluded to be in the acceptable range. The largest error is found in the dimension w3. Here the measured dimension only shows an average value, as it is not possible to make an exact measurement because of the curvature shape in that region.

Table 6.2 Specific measures of the experiments 85 with the simulation results.

LHEXP 85	**$d_{o\,0}$**	**$d_{i\,0}$**	**L_0**	**$d_{e\,1}$**	**$d_{i\,1}$**	**L 1**	**w1**	**w2**	**w3**	**w4**
Experiment	**30**	**16**	**60**	**30.99**	**15.85**	**43.58**	**41.53**	**41.83**	**9.23**	**5.54**
A2	30	16	60	31.65	16.06	43.5	42.23	40.82	10.11	5.44
ERROR %	0.00	0.00	0.00	-2.13	-1.32	0.18	-1.69	2.41	-9.53	1.81

Table 6.3 Specific measures of the experiments 62 with the simulation results.

LHEXP 62	**$d_{o\,0}$**	**$d_{i\,0}$**	**L_0**	**$d_{e\,1}$**	**$d_{i\,1}$**	**L 1**	**w1**	**w2**	**w3**	**w4**
Experiment	**30**	**20**	**60**	**30.75**	**20.09**	**46.95**	**39.05**	**40.38**	**10.42**	**4.30**
A2	30	20	60	30.95	20.31	47.10	39.72	39.76	9.50	4.40
ERROR %	0.00	0.00	0.00	-0.65	-1.10	-0.32	-1.72	1.54	8.83	-2.33

The following chapter will cover the parameter study of the process through this final model, and by utilizing the FEM computer package MSC/Marc 2003.

CHAPTER 7

FINITE ELEMENT SIMULATIONS

7.1 Introduction

The experimental procedure and applications are given in Chapter 4 and the principles of FEM modeling are given previously in Chapter 6. In addition to these, the results of the FEM simulations, comparisons with the actual experiments and parameter studies on the process will be given in this chapter together with conclusions and further recommendations. The aim of the parameter study is mainly to investigate the nature of the process, which is in fact impossible to be done by actual experiments because of the limitations of the setup such as maximum allowable upsetting ratio or the maximum speed of the press.

7.2 Comparison of Numerical Results with Experiments

The final model for the FEM application is given in Chapter 6 together with the specific dimensions of the specimen and the simulation result (Table 6.2). As the primary aim of the finite element analysis of this study is to simulate the application and to obtain the final product shape with the minimum error possible, the most important measures to be examined are bulge height and the bulge width (w_3 and w_4 respectively in Figure 7.1). An error in the order of 10% will be concluded as "acceptable" for the study, because of the nature of the application, and inherent measurement errors due to the measuring inaccuracies related with the complex geometry of the part. In the light of this information, the simulation results of the experiments 85 and 62 (Table 6.2 and Table 6.3) are within the target error range.

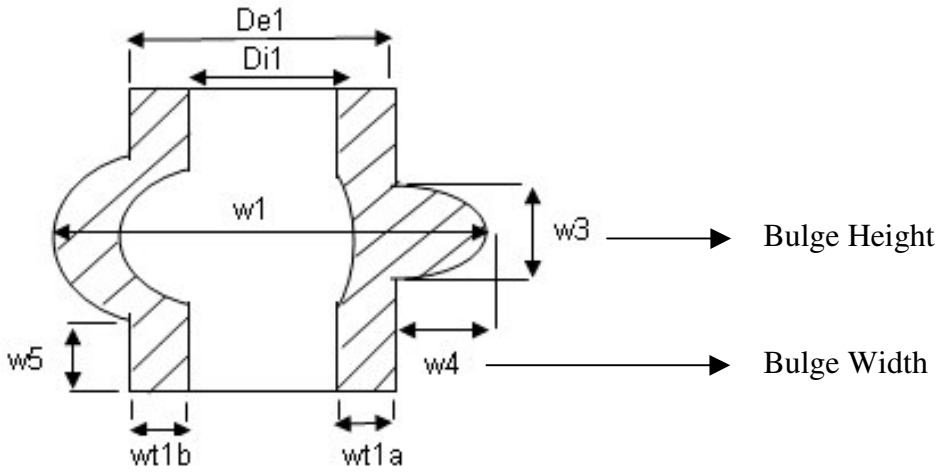

Figure 7.1 Specific dimensions of the local form

The largest error is between the simulations and experimental results are observed in the bulge height dimension (w3). The difference between the absolute values of the measures is approximately 0.9 mm, which brings out the relative error in the order of 9%. As the measured dimensions are small and difficult to be measured, the high percentage error is closely affected by the measurement errors. On the other hand, the general shape of the final product of FE analysis reflects the real case successfully. The local form on the front side and the buckling behavior on the backside are compared in Figure 7.2 and Figure 7.3.

It is believed that, apart from the measurement errors, the main reason of the dimensional errors is the distorted mesh structure in the local deformation zone. In Figure 7.4, it is seen that the aspect ratios of the elements are beyond the acceptable limits. The finite element codes in general include remeshing property in order to avoid such problems. But, it is not possible to apply remeshing to the 3-D hexahedral elements in MSC/Marc 2003, therefore a comparison between "remeshed" and "not remeshed" cases could not be presented in this study.

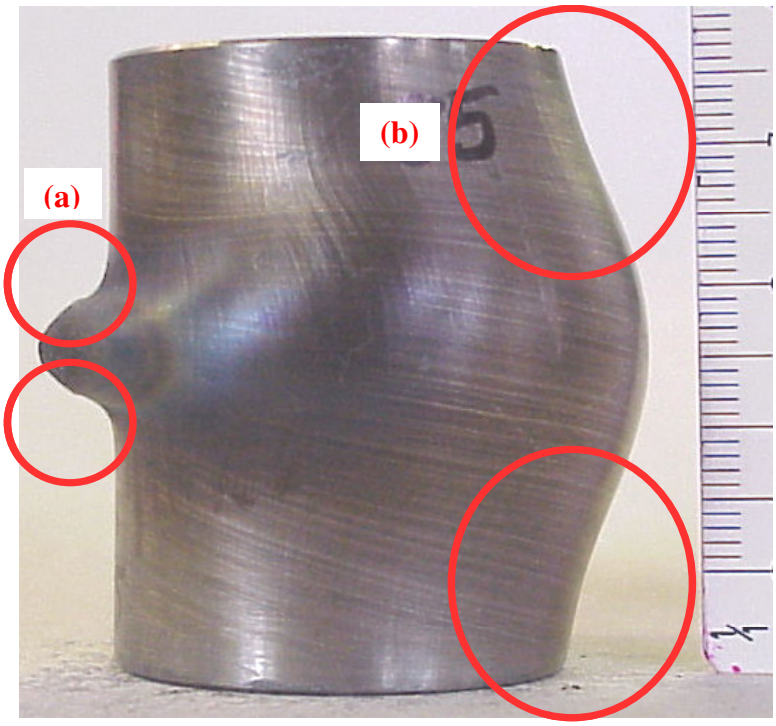

Figure 7.2 (a) Local deformations and (b) buckling behavior on the backside (Experiment 85)

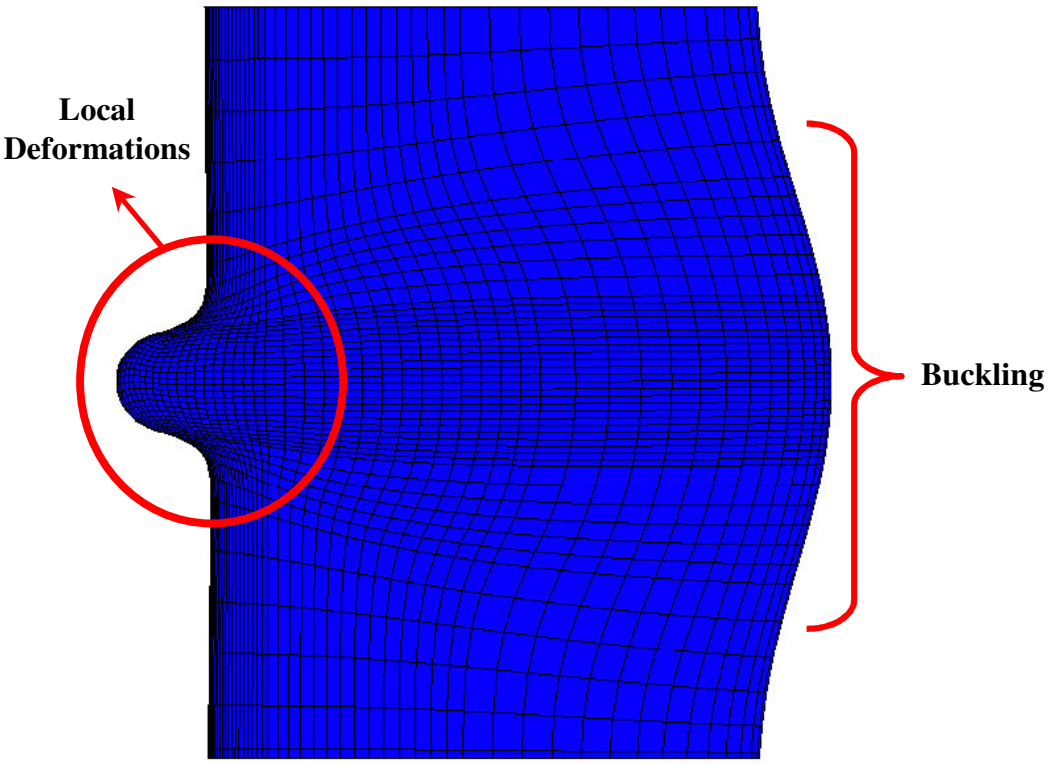

Figure 7.3 Finite element analysis of the product (Experiment 85)

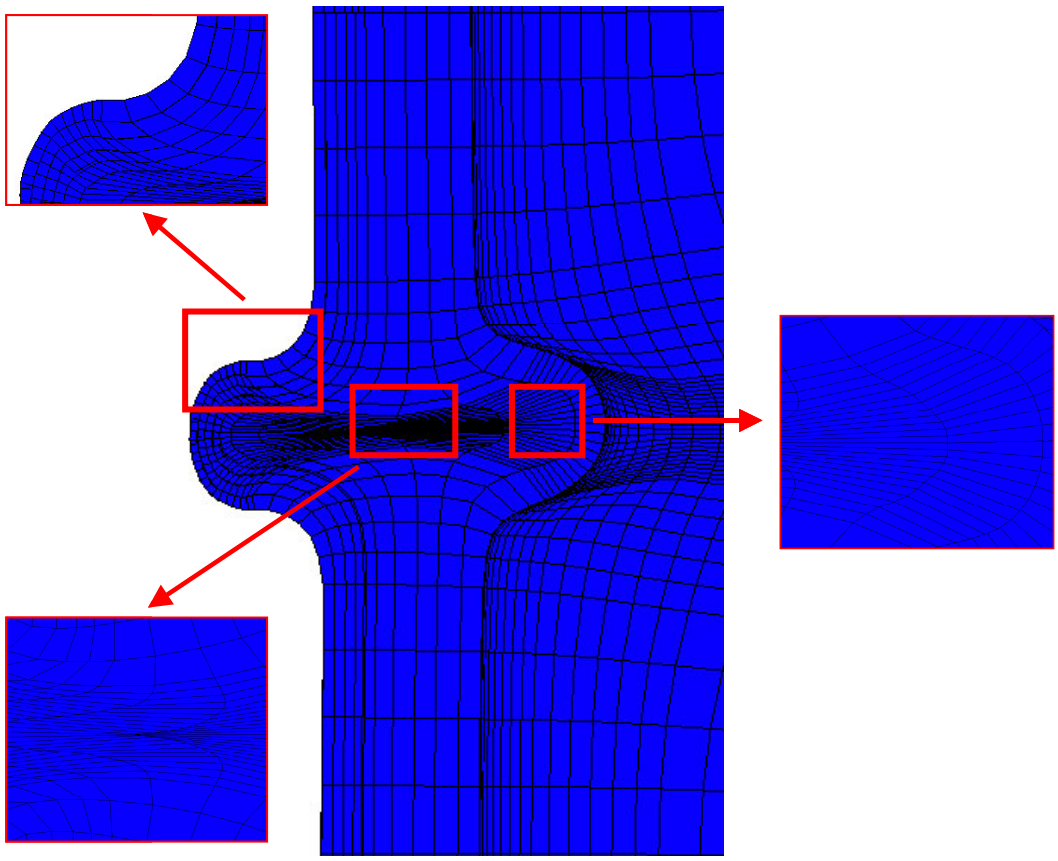

Figure 7.4 Distortions in the mesh structure

7.3 Effect of Heat Flux

The effect of heat flux or the total heat energy given to the workpiece is discussed in Chapter 4, where real case examples are presented. But, on the other hand, during the experiments there might be errors related with the positioning of the initial specimen or with the performance variations of the laser device. In order to be sure about the affect of the heat flux given, a finite element method investigation on this subject must be carried out. For this purpose, again experiment 85 is taken into account. The comparison between the temperature versus time curves of three different heat flux value applications are given in Figure 7.5, where numerically the actual heat flux value, 80% and 60% of the heat flux value are presented.

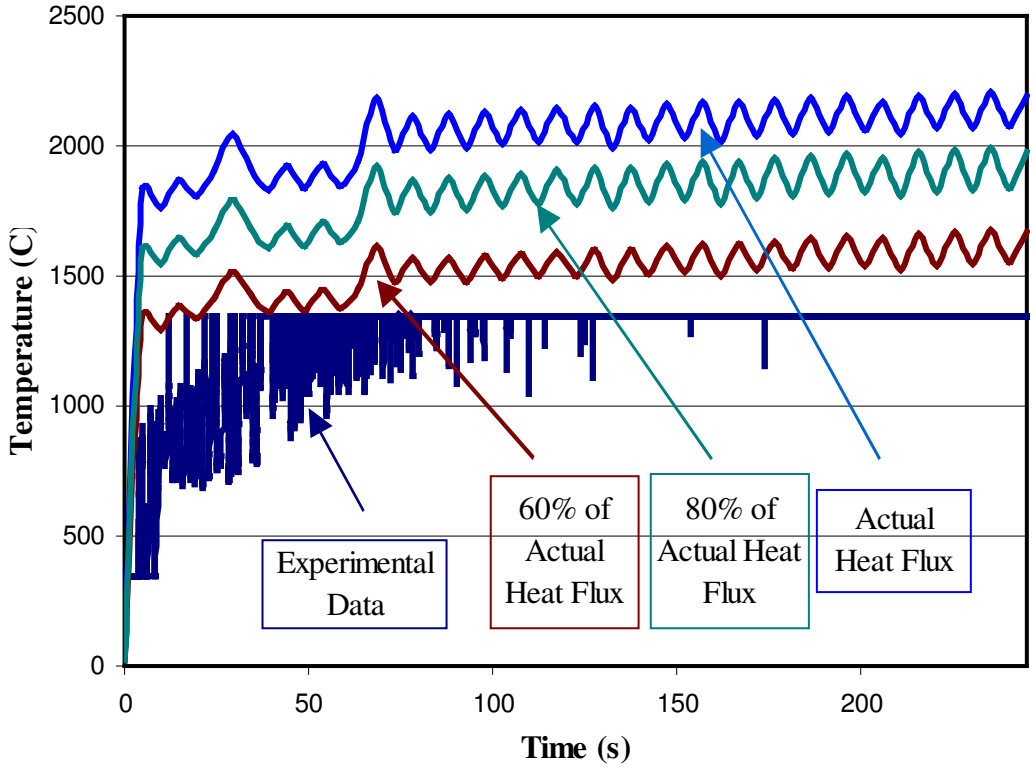

Figure 7.5 Surface temperature data of different heat flux applications

Bulge widths (w_4) of the three simulation results are 5.44 mm, 5.1 mm and 4.10 mm for the actual heat flux, 80% and 60% of the actual heat flux applications, respectively. This means that a 40% decrease in the total heat energy given to the workpiece leads to the resultant decrease in the bulge size, approximately in the order of 25% (Table 7.1). The final (half) products for these three heat flux applications are presented in Figure 7.6.

Table 7.1 Specific dimensions of different simulations

LHEXP 85	$d_{o\,0}$	$d_{i\,0}$	L_0	$d_{e\,1}$	$d_{i\,1}$	**L 1**	**w1**	**w2**	**w3**	**w4**
100% Heat Flux	30	16	60	31.65	16.06	43.50	42.23	40.82	10.11	5.44
80 % Heat Flux	30	16	60	31.99	16.47	43.50	41.30	40.34	11.13	5.11
60 % Heat Flux	30	16	60	31.97	15.85	43.50	40.00	40.26	13.10	4.10

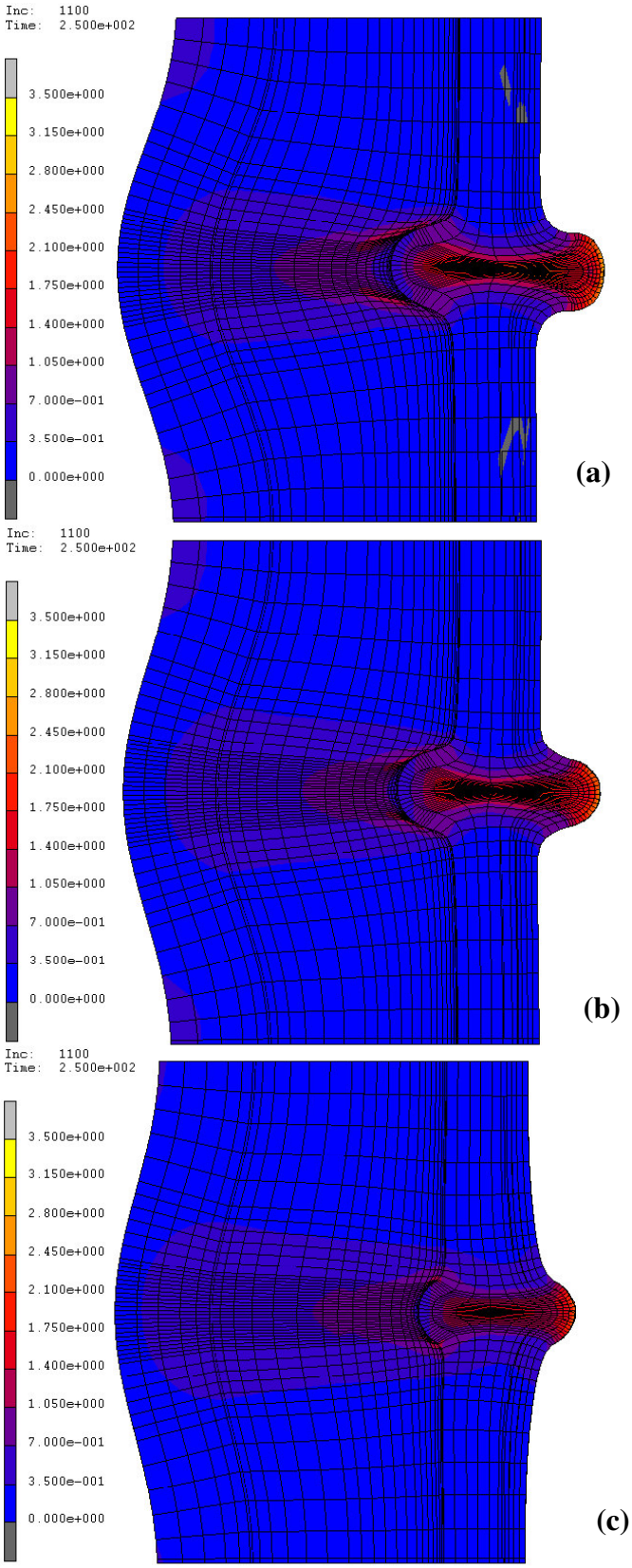

Figure 7.6 Results for heat flux application of (a) 100%, (b) 80%, (c) 60% of actual value (scale is total equivalent plastic strain)

In addition to this, the punch force versus time graphs of these different heat flux applications are given in Figure 7.7. The punch force required to form the workpieces that are preheated by applying the 60% and 80% of the actual heat flux is approximately 25% to 50% higher compared to the one with the actual heat flux application. This is mainly due to the existence and volume of the relatively softer material in the locally heated zone. Theoretically, if more heat energy is applied, it becomes easy to form the material as the result of the general characteristics of the flow curves. As the volume of the heated material is increased by increasing the heat flux value, (and by keeping the heating profile and time constant) the required force for forging operation decreases. But, on the other hand, for this particular study, application of higher heat flux values has negative effect on the final shape of the product because through heating occurs as a result of thermal conduction. The increasing behavior of the punch force in the figure can be explained by the cooling of the specimen and strain hardening, which is the common case for all three applications.

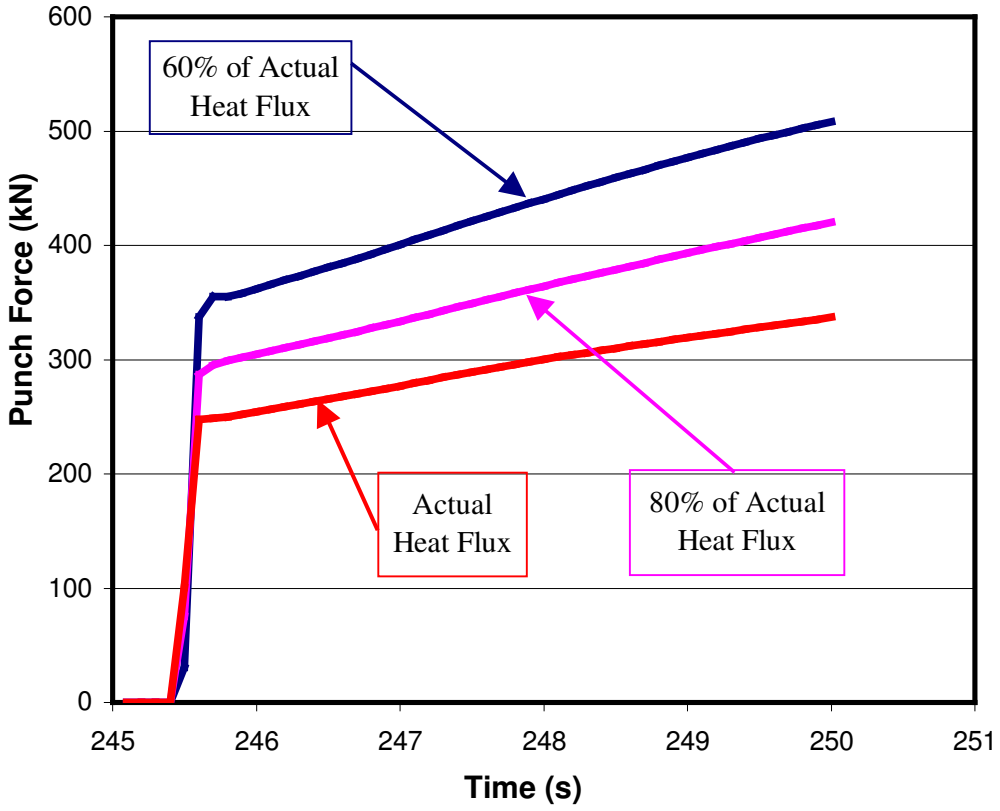

Figure 7.7 Punch force versus time graphs for three different heat flux values

7.4 Effect of Punch Speed

Another important process parameter in this study is the speed of the punch, which was kept constant as 3.6 mm/s throughout the experiments. In fact, the effect of the punch speed is somehow related with the heating characteristics or the temperature distribution in the workpiece body. As the speed of the punch is increased, less time is left for heat diffusion in the specimen, which means that, the local heating will be more dominant. In order to study the effect of the punch speed three different speed values are analyzed; 0.9 mm/s (1/4 of the actual speed), 3.6 mm/s (the actual speed), and 14.8 mm/s (4 times the actual speed). The temperature distributions of the final products (half) are given in Figure 7.8. As the process time is much shorter in the case of a higher press speed the heat propagation through the workpiece is limited. The temperature at the tip of the local form is about 1200^{o}C for the punch speed of 14.4 mm/s whereas it is approximately 400^{o}C less for 0.9 mm/s at the end of the deformation. That means there still exist hot material for further local deformation on the heated side. But on the other hand, again buckling on the rear side has to be taken into account, as cold forming occurs in that region.

Another important point in this subject is the plastic strain distribution of the final products. The bulge heights of the three cases are measured to be 1.5 mm, 3.5 mm and 4.2 mm for the punch speeds of 0.9 mm/s, 3.6 mm/s and 14.4 mm/s respectively. In Figure 7.10, the total equivalent plastic strain distributions of the final products are shown. The strain values on the local forms are approximately in the same order of magnitude. But if whole bodies are examined, as the bulge width increases, the required material for the local form is fed from the other relatively colder parts, which creates strains on the sides. This fact leads to a considerable increase in the punch force required for deformation process (Figure 7.9).

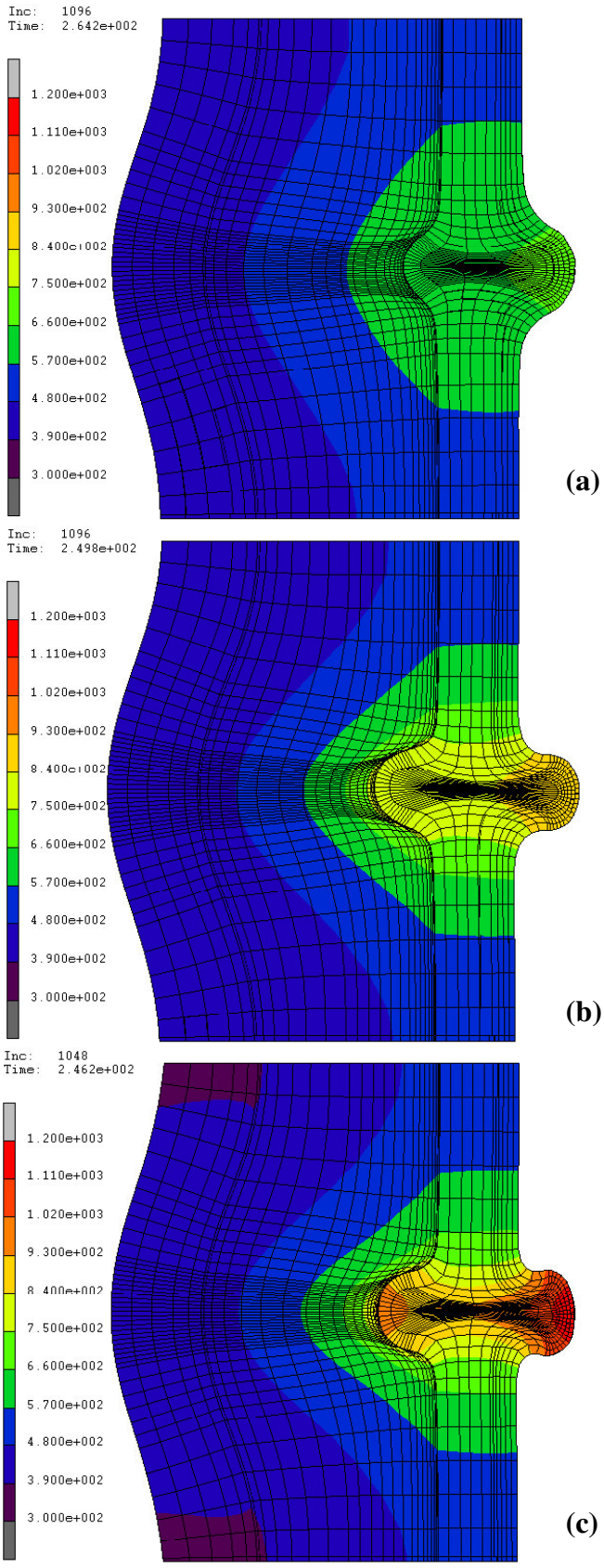

Figure 7.8 Temperature distributions on the final products, for the punch speeds of (a) 0.9 mm/s, (b) 3.6 mm/s, and (c) 14.4 mm/s

In the light of the information and the results presented in Section 7.3, one may expect to have lower punch force values for a faster punch speed case by taking the temperature values in the local deformation into account. But, here two important facts have to be considered; first, an increase in the deformation rate results a shorter process time, which limits the heat propagation in the body. This means that the majority of the workpiece is cold formed. Secondly, according to the general characteristics of the flow curves of the metals, the flow stress tends to increase; as the strain rate is increased for constant strain and temperature and as the temperature is decreased for constant strain rate and strain values. As a result, in Figure 7.9, it is observed that approximately 15% more punch force is required if the punch speed is increased to four times the initial value. Besides, the intersection of 0.9 mm/s and 3.6 mm/s curves indicated the cooling effect on the process after certain time period more punch force is required to form the colder specimen.

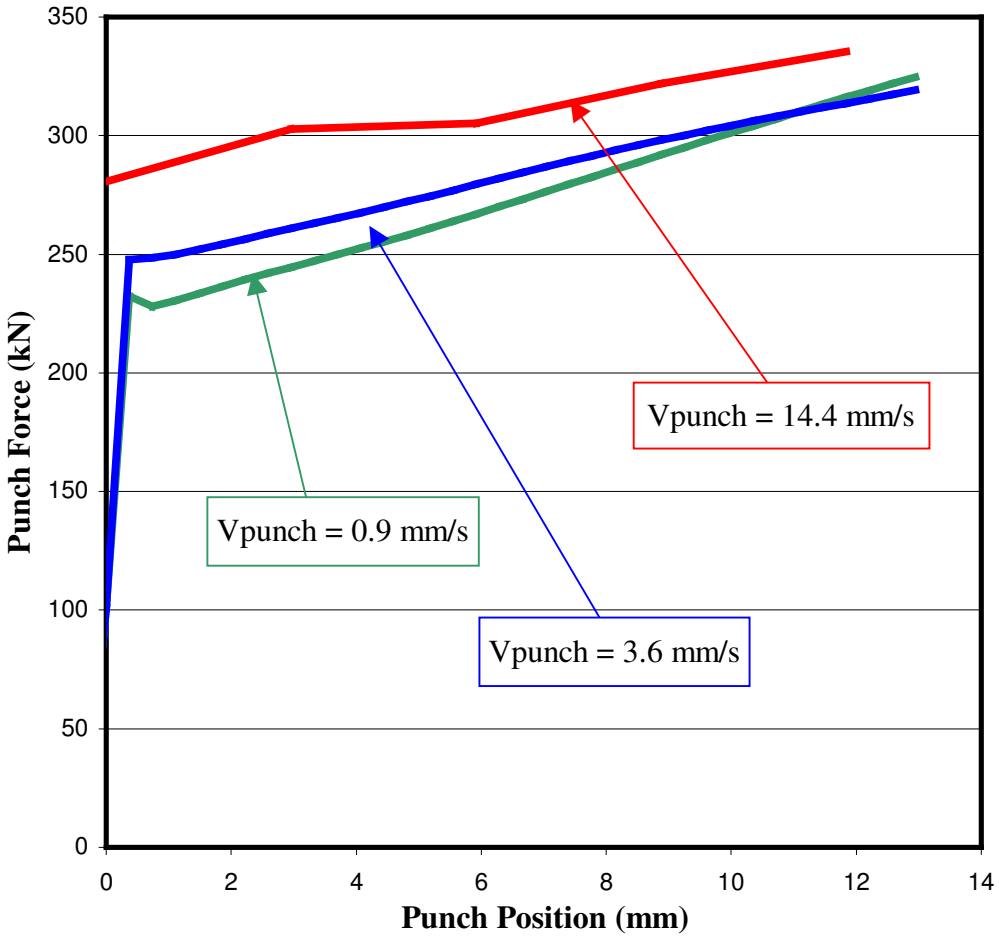

Figure7.9 Punch force versus punch position graph for different punch speeds

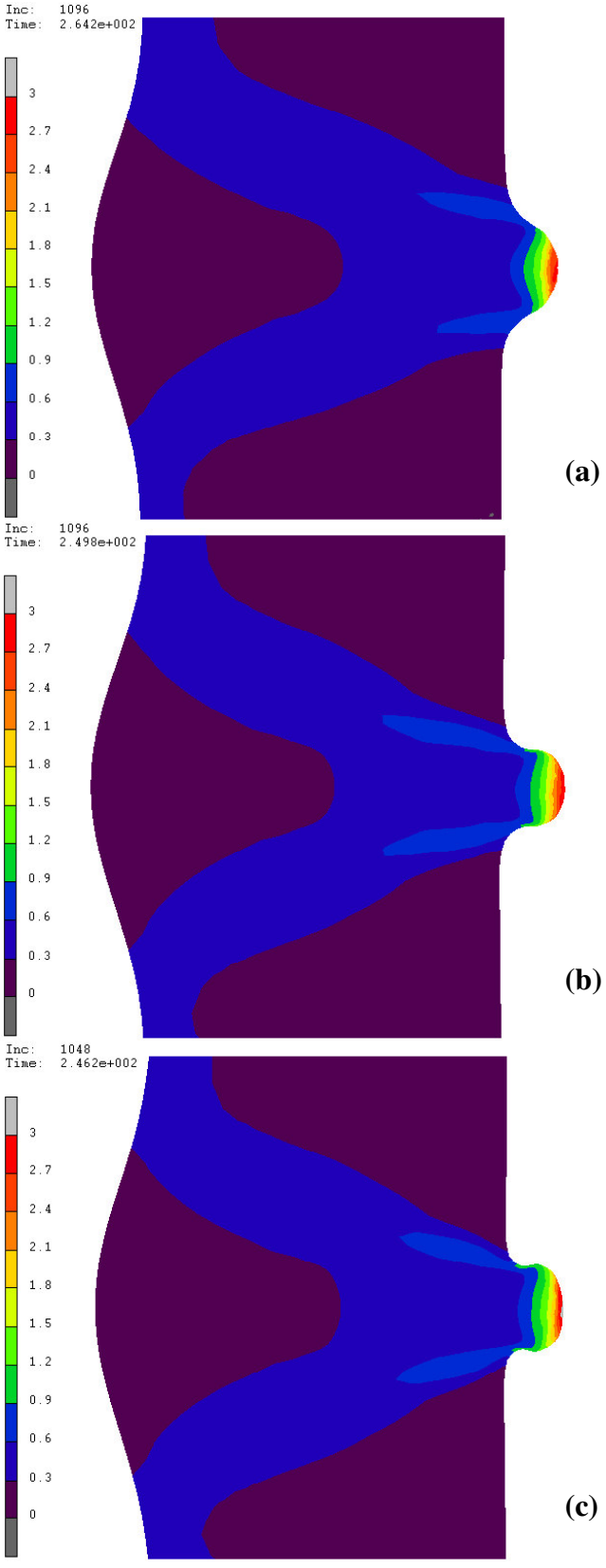

Figure 7.10 Total equivalent strain plots, for the punch speeds of (a) 0.9 mm/s, (b) 3.6 mm/s, and (c) 14.4 mm/s

7.5 Effect of the Initial Geometry

It was previously shown in Chapter 4, that the initial geometry of the specimens has great effect on the local deformation process. This effect must be considered both in the thermal and mechanical point of view. The wall thickness or the solid structure of the workpiece directly affects the heating characteristics as a result of the heat conduction inside the material and the convection on the inner surface. For example, a thin walled example may be considered as an extreme case. It becomes easy to heat such a specimen as a result of conduction. That means through heating of the workpiece for this study, which weakens the local deformation characteristics. On the contrary, as the inner diameter increases, the convection surface of the material increases, which means a higher cooling capacity and hence strengthens the heat localization. A similar trade-off is also valid for the mechanical point of view. For an initially thin walled specimen, it becomes easy to produce the local forms whereas the buckling characteristics on the sides and the backside of the specimen have an opposite effect on the process.

The finite element analysis tool is very helpful to examine such parameters, as it is possible to provide the same production parameters for the workpieces with different initial geometries. For this purpose a fixed total energy of 269,400 Nmm/s is applied with the same heating procedure (4 cycles, heating radius of 4 mm and 25 passes). The sample hollow specimens, which have the inner diameters of 16 mm and 20 mm and a solid one, are examined. The specific dimensions for the study are given in Table 7.2. The total equivalent plastic strain scaled simulation results (halves of the products) are also given in Figure 7.11.

Table 7.2 Specific dimensions of different simulations

Specimen	$\mathbf{d_{o\,0}}$	$\mathbf{d_{i\,0}}$	$\mathbf{L_0}$	$\mathbf{d_{e\,1}}$	$\mathbf{d_{i\,1}}$	**L 1**	**w1**	**w2**	**w3**	**w4**
Hollow 1	30	20	60	30.71	20.01	47.57	40.59	39.55	8.86	5.06
Hollow 2	30	16	60	31.28	16.16	47.57	39.46	37.95	11.79	4.44
Solid	30	-	60	31.96	-	47.57	38.33	36.18	13.06	3.99

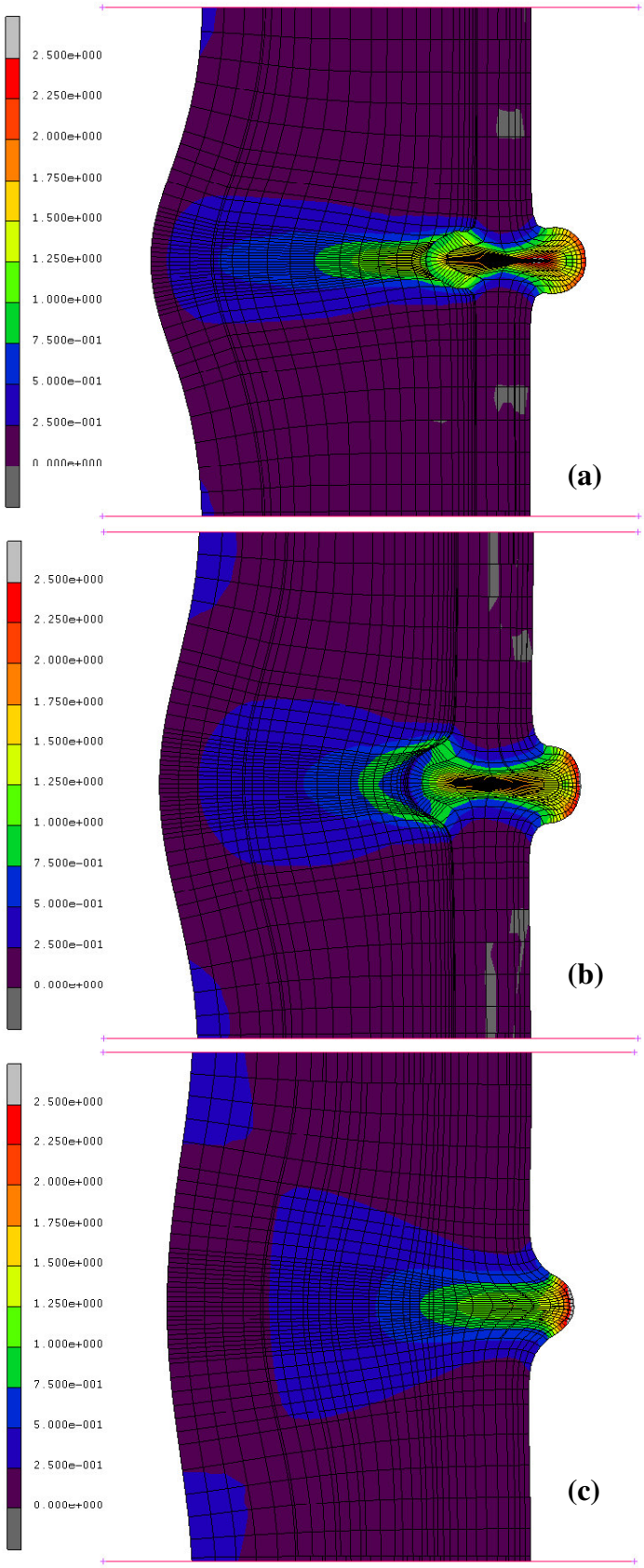

Figure 7.11 Results for specimens (a) Hollow 1, (b) Hollow 2, (c) Solid (scale is total equivalent plastic strain)

The results show that the heating effect on the locally heated region dominates the deformation characteristics. As the wall thickness decreases, the heat localization and hence the local deformation is observed on the front side, which is a positive effect for the process idea. On the other hand, the buckling effect is clearly seen on the backside especially for the minimum wall thickness case.

7.6 Local Deformation Criterion

The main aim of this study is to produce local forms on axisymetrical workpieces. Here a local deformation criterion has to be set. Considering the general shape of the final product, absolute value bulge width (w_4) cannot be the only criteria for local deformation. The buckling behavior is also observed on the circumferential region. The dominant deformation should be obtained on the locally laser-heated region in order to realize the local deformation idea. This means that the deformation rate should be higher compared to the buckling zone I and buckling zone II (Figure 7.11). For this purpose the deformation characteristics of the experiments 85 and 62 are examined (see Table 4.3 for the details of the experiments).

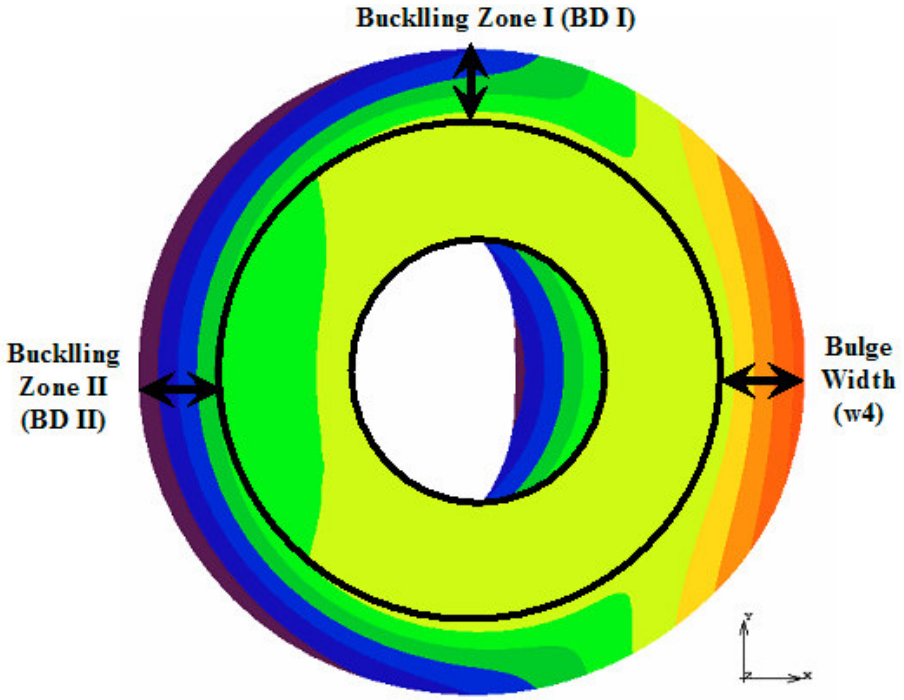

Figure 7.12 The top view of the final product

The deformation characteristics of the process is observed through dimensionless parameters w_4 / *BD I* and w_4 / *BD II*. These two parameters are evaluated with respect to the length of the product.

Experiment 85 is examined in Figure 7.12. Here two regions must be carefully evaluated. First, $\Delta L/L_o$ (ratio of change in final length to the initial length) ratio of approximately 0.05 is the peak point of local deformation. Here it can be claimed that the deformation is highly localized on the preheated region. But, as it is the very beginning of the process, the size of the local form is insufficient. Second, the 0.15-0.20 region of $\Delta L/L_o$ value is important, as the ratio of bulge dimension to the buckling dimensions become less than the critical value 1. The importance of this value is that, from this point on, the deformation becomes dominant on the buckling regions. So beyond this level, the local deformation idea is no more valid.

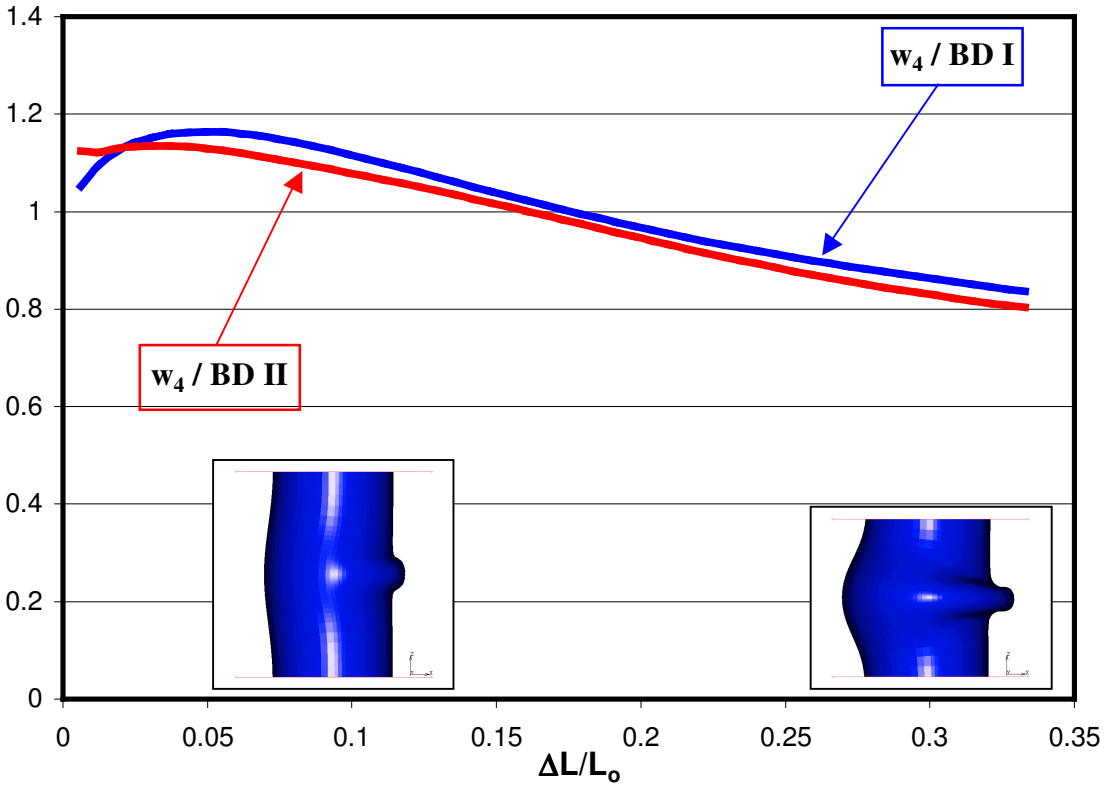

Figure 7.13 Local deformation characteristics for Experiment 85

The same study is also done for experiment 62, which is shown in Figure 7.13. This time the peak performance of the process is realized for the $\Delta L/L_o$ value of approximately 0.04. After this value, a steep decrease in local deformation characteristics is observed. The critical value of local form dimension to buckling dimensions is reached for the $\Delta L/L_o$ value of 0.10-0.13. These values are smaller compared to the results of the experiment 85, which mean that it is more difficult to maintain the local deformation characteristics in experiment 62. This is mainly due to the difference in the wall thickness. The inner diameter is 16 mm for experiment 85 and 20 mm for the experiment 62, which results in a more dominant buckling behavior in experiment 62.

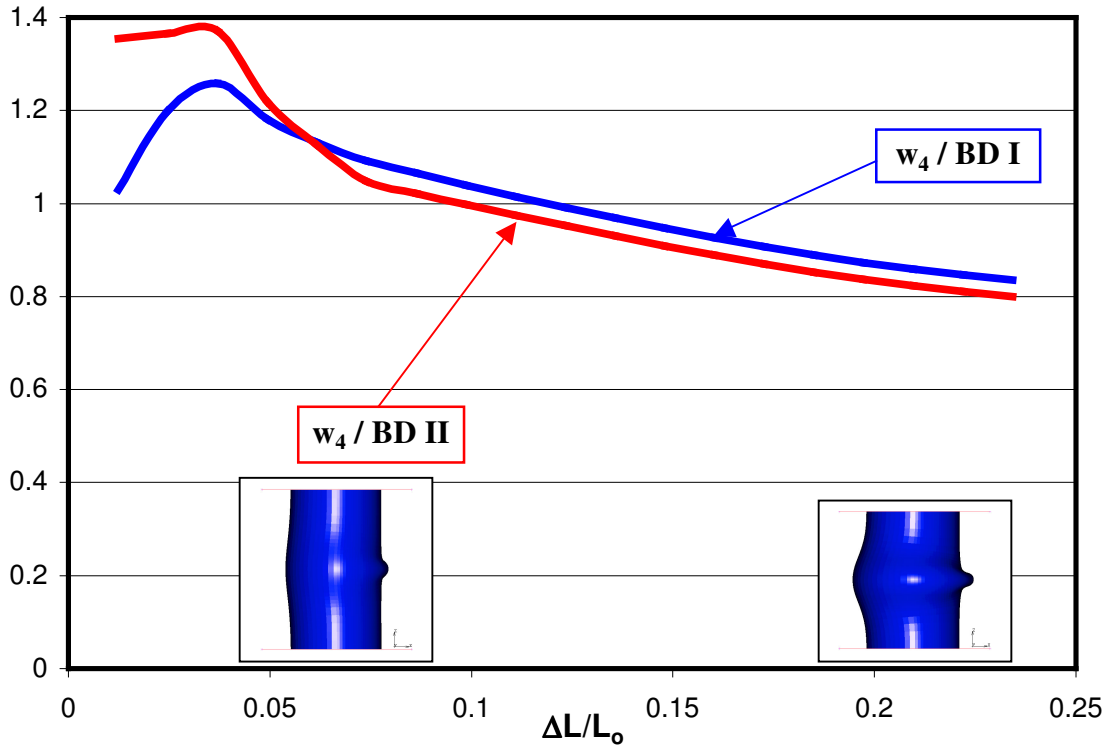

Figure 7.14 Local deformation characteristics for Experiment 62

Apart from the analysis of the real experiments, the deformation characteristics of the simulation results must also be examined in order to observe the effects of the parameters more clearly. For this purpose the effect of the heat flux given to the workpiece and the effect of the initial geometry on the final product, which are

presented in Section 7.3 and Section 7.5 are studied through the w4 / BDII parameter as the backside buckling is the main limitation on the local deformation criteria.

The effect of the heat flux given to the workpiece is given in Figure 7.15. From the local deformation point of view, again 0.15-0.20 region of the $\Delta L/L_o$ parameter is important as the buckling effect dominates the process for further deformation. But, here two important facts have to be considered carefully. First, the graph shows that an increase in the heat flux value of the laser does not always mean a better local deformation characteristic. This fact was also discussed in Chapter 4 previously, which leads to the conclusion that after a certain point the through heating case occurs and local deformation becomes no more valid. Second, the analyses show that the effect of the energy given to the workpiece has a converging effect on the process. It is possible to observe that all of the resulting curves converges to the ratio of approximately 0.83 for $\Delta L/L_o$ ratio of 0.3. this means that due to the cooling of the specimen the deformation characteristics of the different processes tend to converge a specific value. This value is naturally different for different initial geometries or total heat energy values, which may be examined as a further study on this research.

The effect of the initial geometry of the specimen is also given in Figure 7.16. In Section 7.5, it was shown that the, the product with the minimum initial wall thickness value has the maximum bulge height (w_4). But on the contrary, according to the local deformation criteria w_4 / BDII, the local deformation behavior of the Hollow 1 specimen shows a steep decrease as a result of the strong dominating effect of the buckling behavior.

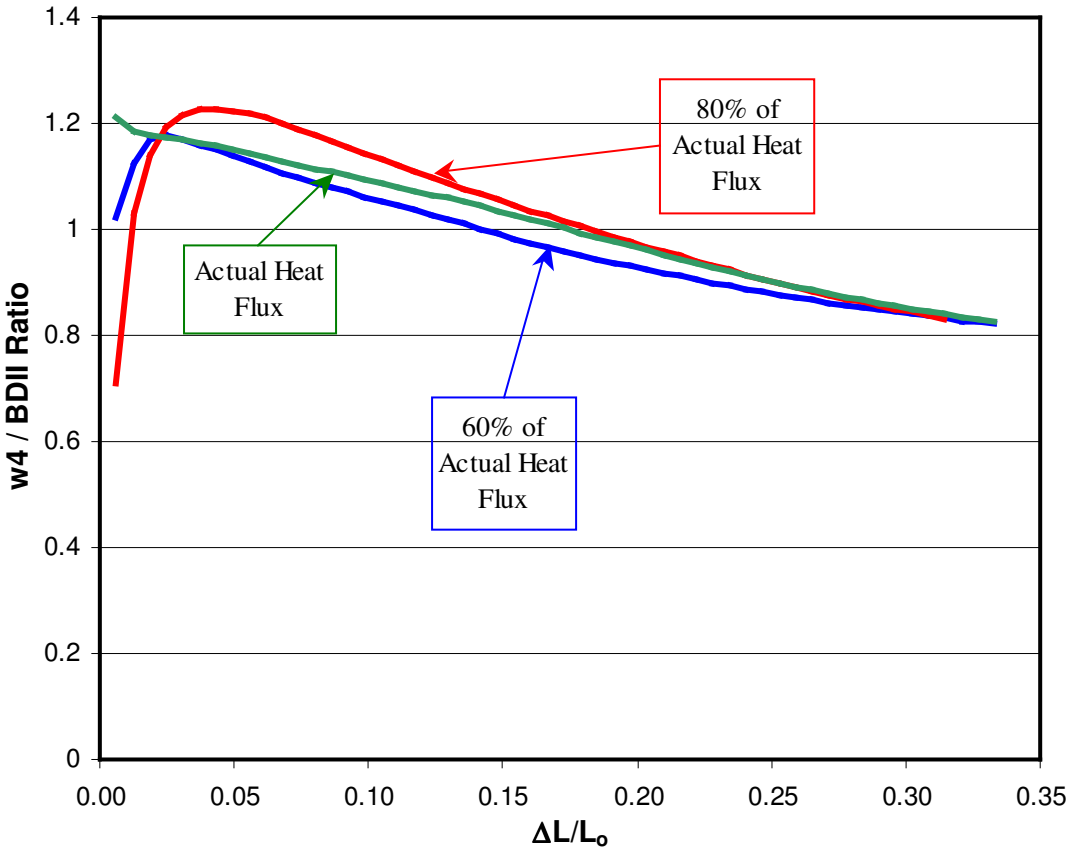

Figure 7.15 Local deformation characteristics for the heat flux analyses

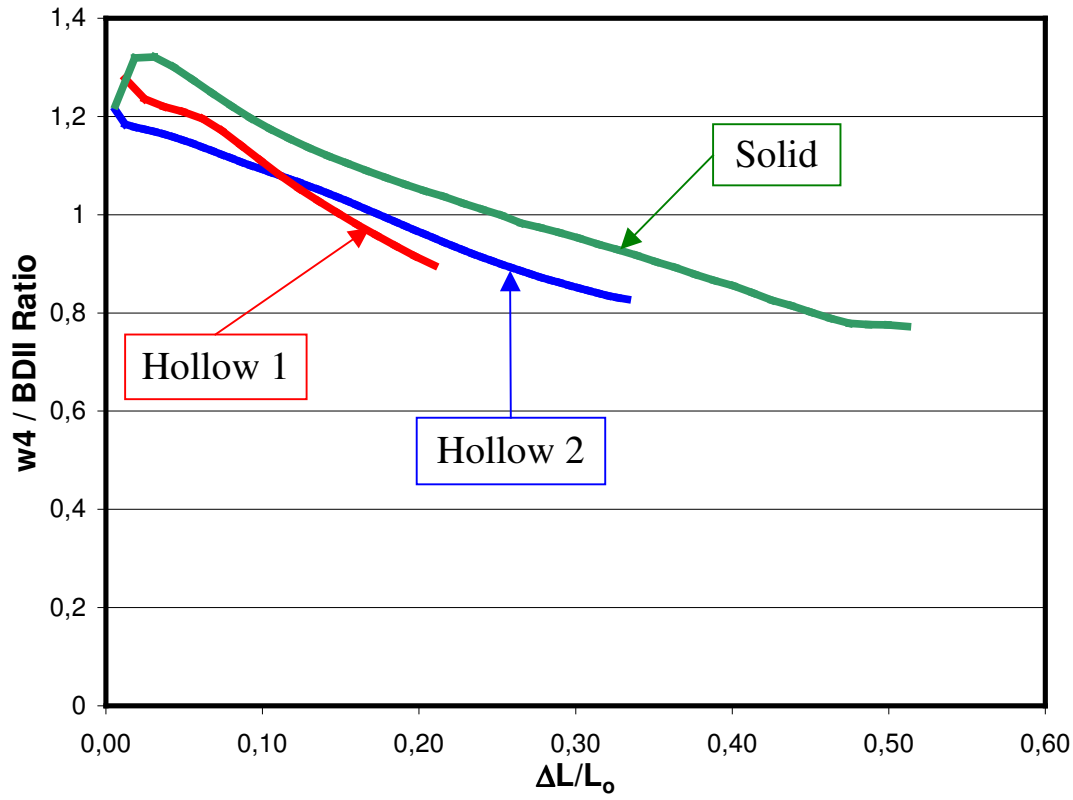

Figure 7.16 Local deformation characteristics for the initial geometry analyses

7.7 Local Bulge Formation Criterion

The local deformation criterion explained in the previous section is helpful in understanding the dominant deformation characteristics of the process. On the other hand, an additional criterion has to be set in order to investigate the local bulge formation. This can be done by comparing the local bulges obtained in the final product. For this purpose, an explanation must be done to define the term *local bulge.* In Figure 7.17, the dimensions of the local bulge are shown. The bulge height and bulge width (Figure 7.1) are the key dimensions in the definition of the local bulge term. The bulge width is measured from the edge of the workpiece to the bulge tip and the bulge height is measured between the 10 % of the bulge width regions.

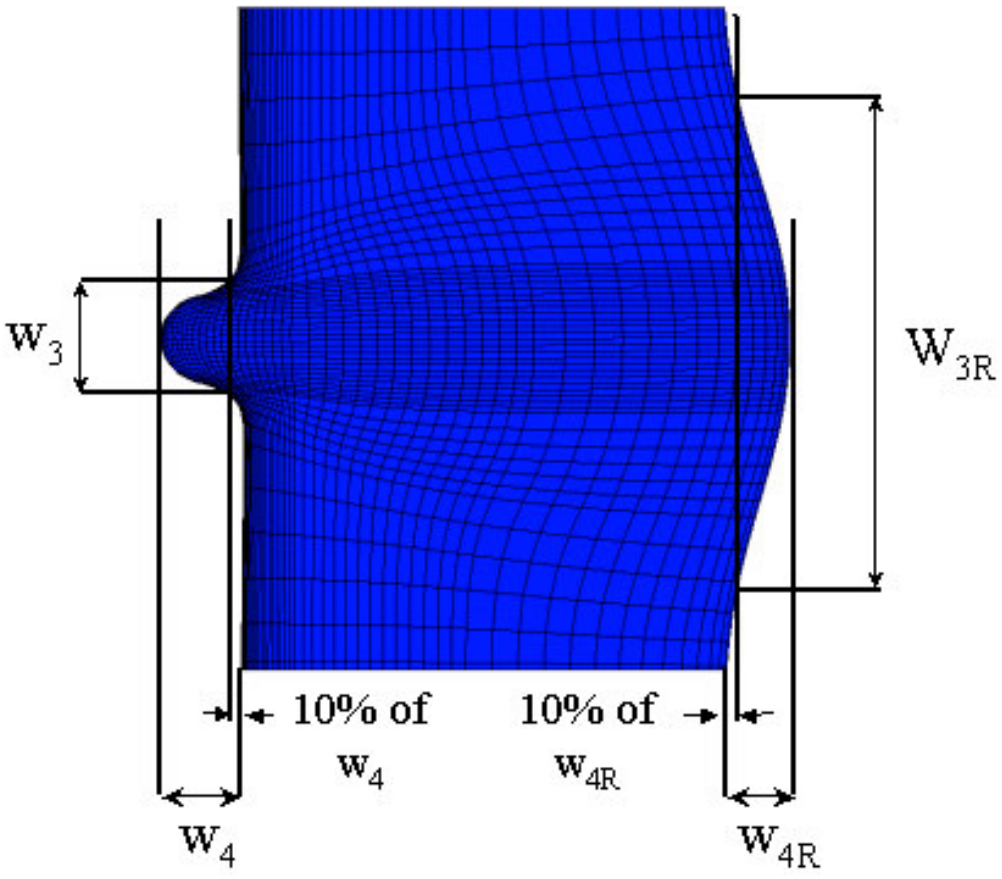

Figure 7.17 Dimensions of the local bulge

The bulge deformation is claimed to be more "local" if the w_3 / w_4 (or w_{3R} / w_{4R}) value is higher, which means that the material is formed in a restricted region without spreading to the whole body. Again these parameters are examined with respect to the dimensionless ΔL / L_o (ratio of change in final length to the initial length) parameter.

Experiment 85 is examined according to the local bulge formation criterion in Figure 7.18. It is clearly observed that the bulge formation is much more *local* in the heated region. The peak value of approximately 0.6 is observed in that region together with the further increase tendency, whereas on the rear side the local bulge formation ratio is below 0.1 as a result of the relatively higher w_{3R} and lower w_{4R} values.

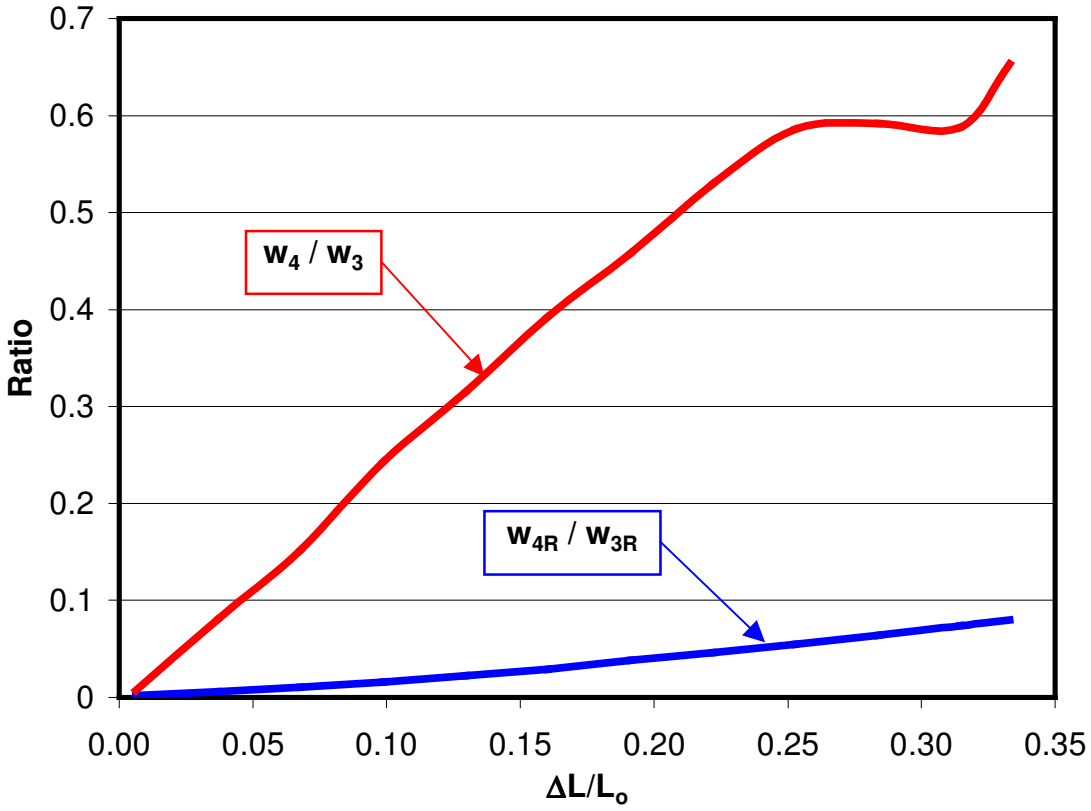

Figure 7.18 Local bulge formation characteristics for Experiment 85

The same study is again done for experiment 62, which is shown in Figure 7.19. This time the peak value of 0.5 is reached for the local bulge formation ratio and again the increasing tendency is observed in the heated and the rear sides. It is believed that the decrease after the $\Delta L / L_o$ value of 0.2 is temporary and due to the measurement errors. The overall characteristics should be taken into account for more reliable comments. The bulge formation due to buckling on the rear side is more visible with the bulge formation value of approximately 0.15. This result is related with the lower wall thickness of the initial specimen which leads to more dominant buckling behavior.

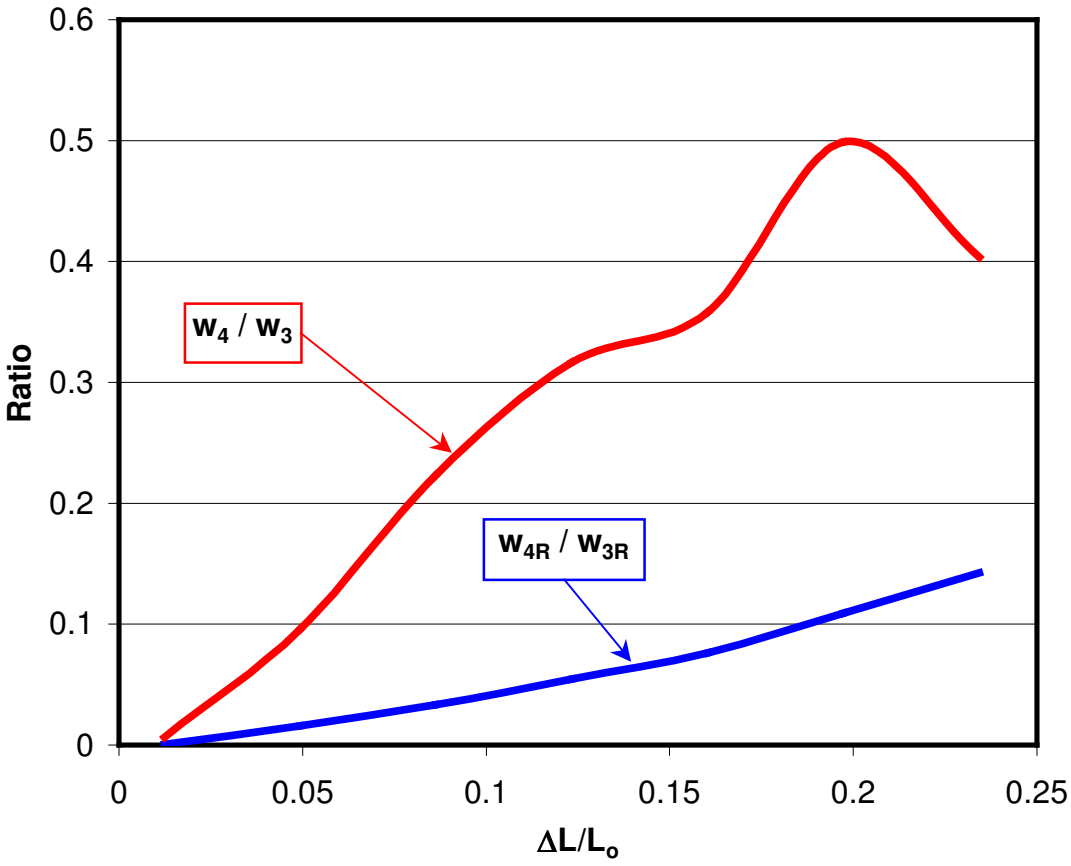

Figure 7.19 Local bulge formation characteristics for Experiment 62

If the local bulge formation characteristics of the experiments 85 and 62 are examined, it can be concluded that the local deformation by local laser heating process is successful as the bulge formation is approximately four times larger in the heated region.

In order to observe the effects of the parameters on the local bulge formation more clearly, the simulation results of the parameter studies must also be examined. For this purpose the effect of the heat flux given to the workpiece and the effect of the initial geometry on the final product are studied through the same local bulge formation criterion.

The effect of the heat flux given to the specimen on the local bulge formation is presented in Figure 7.20. The bulge width to the bulge height ratio decreases to its 1/3 as a result of a reduction of 40 % in the total heat flux applied to the workpiece. The converging characteristics to the ratio of 0.2 for the bulge formation criterion of 60 % of actual heat flux application is de to the overall cooling of the specimen, which can be taken as a limit for such a local deformation process.

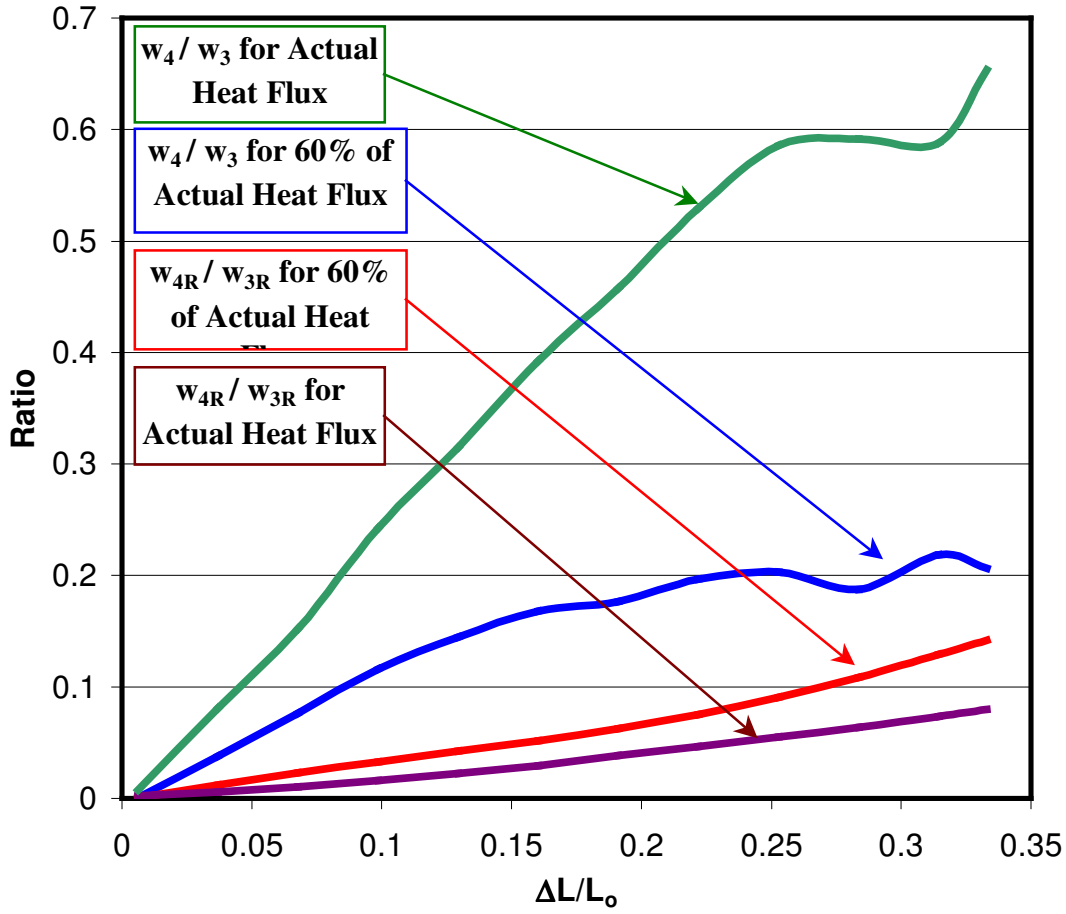

Figure 7.20 Local bulge formation characteristics for the heat flux analyses

Another important point related with Figure 7.20 is the local bulge formation ratio of the rear side of the workpiece. Even though the rear side is not directly heated by the laser the bulge formation characteristics is closely effected by the amount of the total heat flux. This behavior can be explained by the material flow paths inside the material due to heat distribution. As a result of inadequate heating and successive cooling the forming characteristics on the heated and unheated parts tend to converge.

The effect of the initial geometry of the specimen is also given in Figure 7.21, where the hollow 1 and solid specimens (see Table 7.2) are compared according to the local bulge formation criterion. As it was previously stated same amount of total energy is given to the workpieces together with the same heating procedure.

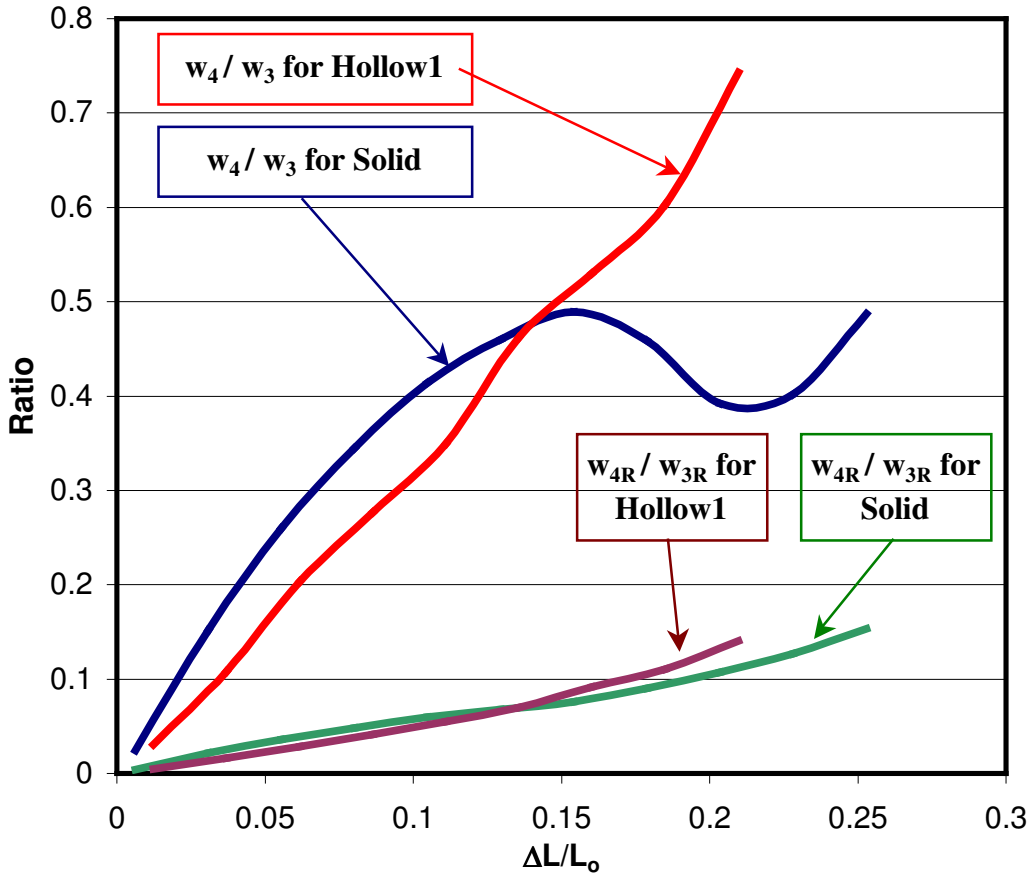

Figure 7.21 Local bulge formation characteristics for the initial geometry analyses

The local formation characteristics of the hollow 1 specimen is observed to be stronger than that of the solid one. This is again mainly related with the heat conduction inside the material. On the other hand the heat is localized on the heated side for the hollow 1 specimen ad therefore a more dominant local bulge formation is obtained.

As a result, the local deformation characteristics and the final product of the process should be considered together, in order to define the production strategy. The bulge height, the local deformation and the local bulge formation parameter studies would lead to the optimum point of process, which means that a considerable number of analyses should be done.

CHAPTER 8

CONCLUSIONS, DISCUSSIONS, RECOMMENDATIONS & FURTHER STUDIES

The aim of this thesis study is to produce local forms on the axisymetrical workpieces by applying local laser heating procedures and successive free forming. The limits of the process, the geometries of the final products, possible failures and drawbacks of the process are covered by experimental and numerical researches. The solutions and possible ways to obtain satisfactory final products are investigated.

The experiments and the numerical studies were carried out simultaneously to observe the effects of parameters on the process closely. Moreover, finite element analyses are utilized to investigate the limits of the process beyond the limits of the experimental setup.

Throughout the research, the process is examined in two main parts as, local laser heating and free forming of the specimen. In fact, the research was carried on in a closed loop interaction of these two parts (Figure 8.1). The heating directly affects the deformation characteristics and the inspections on the final product show the way to modify the heating or forming parameters.

It is observed that, controlling the local laser heating process is very difficult due to number of the parameters, which affect the temperature distribution in the specimen to be upset. Amount of the applied energy, material type and thermal properties of the specimen, absorption or reflection characteristics due to the surface conditions

of the material and the orientation of the laser head, the initial geometry of the workpiece, the heating profiles applied by the five axes robot arm have direct effects on the local heating and consequently on the final shape of the product.

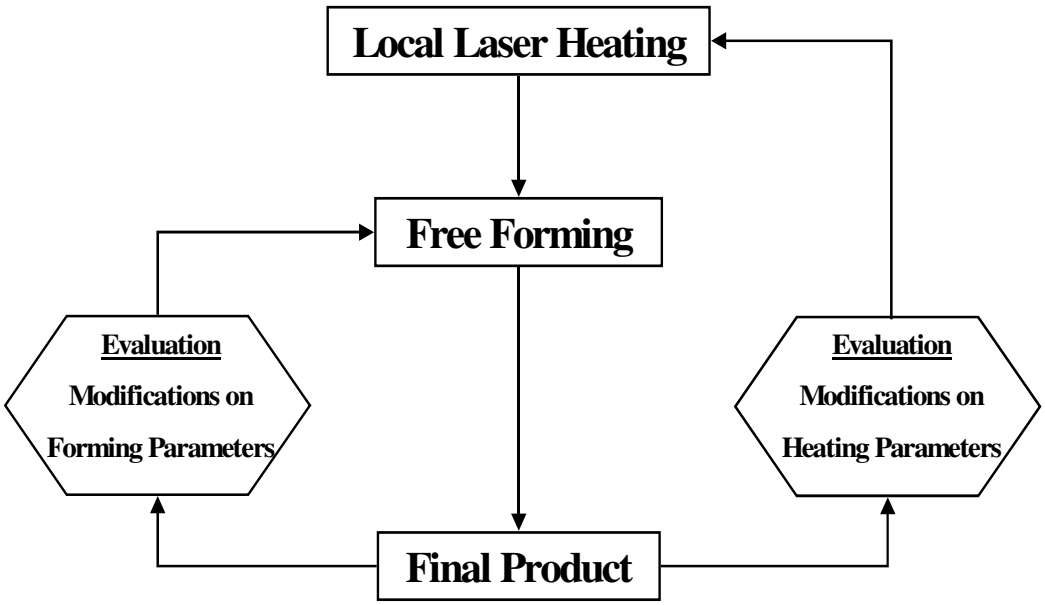

Figure 8.1 Flowchart of the research studies

The amount of the heat energy transmitted to the specimen is found to be as high as possible to invoke more material volume to flow, but as low as possible to avoid melting on the surface and through heating of the specimen which leads to flange-like formation on the circumference. In order to obtain a more detailed process window, this research must be done experimentally or numerically for all of the initial specimen geometries and material types with different laser heating procedures. The further studies on this subject, therefore needs long calculation time for FE analyses with the current modeling application. The writer's recommendation on this subject is first to study on a more "economical" finite element model and than to scan the process limits. For this purpose, a detailed study on the simulation of the final temperature distribution of the workpiece can be done by applying appropriate initial conditions and waiting times rather than simulating the real heating procedure.

Apart from the production and transmission of the heat energy, the material type and the thermal properties (such as thermal diffusivity) of the specimen together with the surface conditions also have dramatic effect on the local heating. This is mainly related with the percentage of the energy used for local heating as a result of absorption-reflection characteristics and thermal properties.

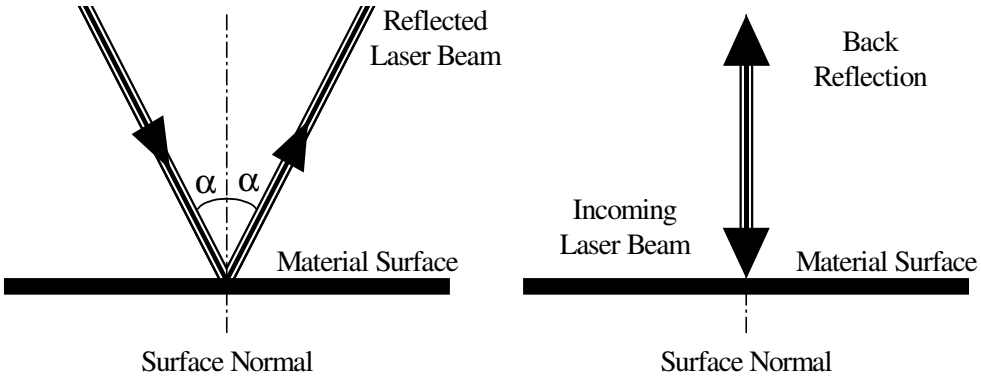

Figure 8.2 The incident angle and back reflection in laser applications

The absorption-reflection characteristics are related with both the surface condition of the material and the orientation of the robot arm. The studies have shown that the materials such as stainless steel or titanium should be used for laser heating after coating or painting because of their shiny surfaces, which reflect the laser back to the environment. As a considerable amount of energy is reflected, the heating effect of the laser could not be obtained on the workpiece. In addition to the surface conditions, the incident angle between the workpiece and the laser head plays also an important role in the absorption-reflection characteristics. In general, the incident angle must be close to zero for maximum efficiency, but must also be large enough to avoid back-reflection, which may harm the lens of the laser (Figure 8.2). As the removable laser head is directed by the robot arm, the workspace of the arm must be carefully examined to ensure the right position for heating. It is not possible to follow the surface contour of a cylinder by using a five axes articulated robot arm (Figure 8.3(a)). Because of this, the incident angle on the heating profile shows differences on different points, which leads to different heat flux applications on different positions of the heating circles. In order to avoid such a problem, six axes

articulated robot arm should be used to follow a circular contour (Figure 8.3(b)) without changing the incident angle (α).

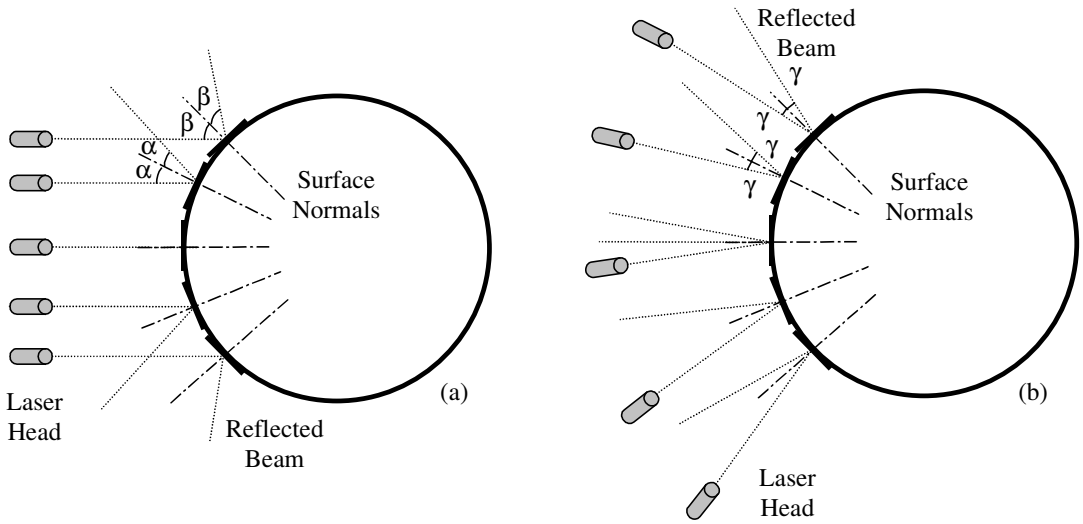

Figure 8.3 Surface scanning capabilities of (a) the five-axes (b) the six-axes articulated robot arms

Apart from these points related with the application of the laser, the shape of the final product is also affected by the thermal properties of the material. Thermal diffusion, which is presented in Section 4.3, is the main indicator of how the heat propagation occurs in the workpiece. In order to realize the local heating, the thermal diffusivity of the material should be small in order to store the thermal energy in a local volume rather than conducting to the whole workpiece volume. Here, the two theoretical extremities of the process must be evaluated to understand the mechanism. First, if the thermal diffusivity of the material is very high (theoretically infinity), homogenous heat distribution in the material will occur, which is in fact the through heating case and no local form will be produced as the deformation will also be homogenous. On the other hand, very low (theoretically zero) thermal diffusivity value should be taken into account as the second case, in which there will not be any heat conduction and all of the thermal energy will be concentrated on the surface as a thin layer. Again, no local form would be observed for such a case, as there will not be enough volume of heated material.

Another important parameter in the local heating part of the process is the laser heating procedure (presented in Section 4.4). Infinitely many variations may be created to examine the effect of the shape of the procedure. In addition to this, the speed of the application must be studied in detail in order to obtain a heating procedure based process window.

From the metallurgical point of view, the melting and martensite formation in the locally heated zone can cause problems for the further forming operations. As a solution to the problem, annealing should be utilized for better microstructural properties.

On the free forming side of the process, the press speed and the upsetting ratio have to be carefully set in order to obtain the maximum width for local form. The press speed, in fact is related with both the heating and forming applications, as it directly affects the process time (for heat diffusion). The finite element simulations of different press speeds are presented in Section 7.4. The press speed is found out to be the maximum value available for a specific heating procedure in order to obtain the maximum local form width. The main limitation would be the maximum available force of the punch and crack propagations on the workpiece body as the result of the high strain rates together with the low temperature values especially on the relatively colder rear parts (for brittle materials such as the titanium alloy Ti6Al4V). Consequently, researches on material properties must be carried out to find available more ductile materials with proper thermal diffusion characteristics.

As a recommendation for increasing the width local form, the design of the dies should be changed. The local form would be directly shaped by the modified dies shown in Figure 8.4. Also a similar solution could be found to avoid buckling on the rear side on the specimen.

Unfortunately, there is no analytical approach to the subject case, which makes the finite element simulations the only tool to be used in the design of the heating and forming applications.

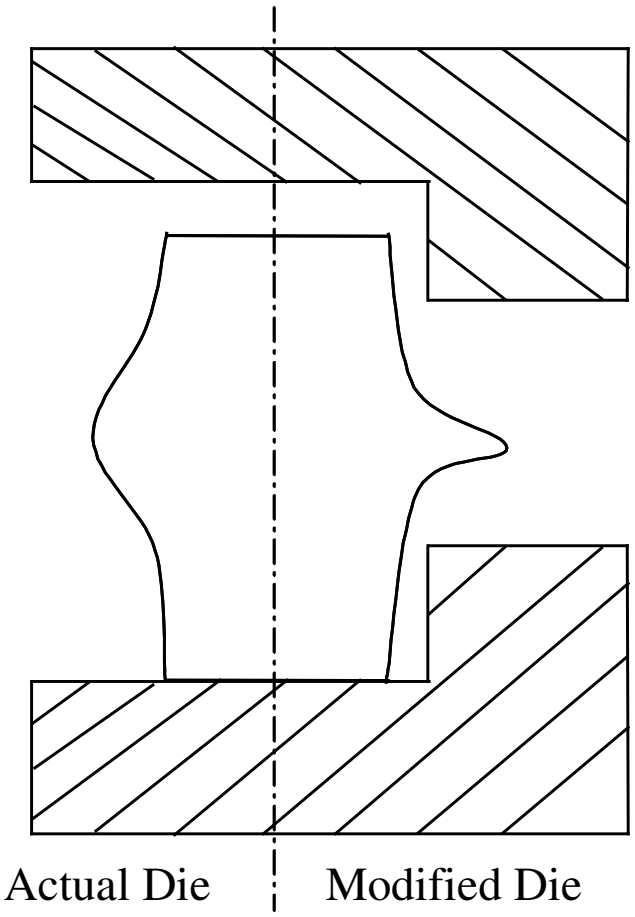

Figure 8.4 Recommended die structure

As a final word, this research is successful to present the correct input parameters for local laser heating and successive free forming applications together with the possible failure modes, drawbacks and limits of the process. It was clearly shown that, with the proper heating and forming parameters, it is possible to obtain local forms on cylindrical parts. The finite element tools are used effectively to guide the manufacturers to produce such parts accompanying the customer needs. Finally, the author believes that this study is an introductory step for local laser heating and forming operations. Long-term researches on this subject should be carried out to gain full control on the process and to obtain different local formations.

REFERENCES

1. Lange, K., *Handbook of Metal Forming*. 1985: McGraw-Hill. 10.10-11.20.

2. Tekkaya, A.E., *ME 453 Lecture Notes*, in *METU*. 2001: Ankara.

3. Bova, B., *The Amazing Laser*. 1971, Philadelphia: The Westminster Press. 17-20,43-45.

4. Lytel, A., *ABC's of Lasers & Masers*. Second ed. 1968, Indianapolis: Howard W. Sams & Co. 13-14.

5. Brown, R., *Laser Tools of Modern Technology*. Doubleday Science Series. 1968, New York: Doubleday & Company. 21-23.

6. Leinwoll, S., *Understanding Lasers and Masers*, New York: John F. Rider Publisher Inc. 16-20.

7. Gibilisco, S., *Understanding Lasers*. First ed. 1989: Tab Books Inc. 25-50.

8. Charschan, S. S., *Lasers In Industry*. Second ed. Western Electric Series. 1972, New York: Van Nostrand Reinhold Company. 190-290.

9. Firth, Kenneth, *A Guide To The Laser*. Second ed, ed. D. Fishlock. 1968, London: Maconald & Co. 85-100.

10. G. Yanjin, S. Sheng, Z. Guoqun, L. Yiguo, *Finite Elelement Modeling of Laser Bending of Pre-Loaded Sheet Metals.* Journal of Materials Processing Technology, 2003(142): p. 400-407.

11. Z. Hu, R. Kovacevic, M. Labudovic, *Experimental and Numerical Modeling of Buckling Instability of Laser Sheet Forming.* International Journal of Machine Tools & Manufacture, 2002(42): p. 1427-1439.

12. N. Hao, L. Li, *Finite Element Analysis of Laser Tube Bending Process.* Applied Surface Science, 2003(208-209): p. 437-441.

13. E. Merrygold, F.H. Osman, *Forging of Complex Geometries With Differential Heating.* Journal of Materials Processing Technology, 1998(80-81): p. 179-183.

14. *Lasers in Chemistry*. Retrieved November 10, 2004, from La Salle University Web site: http://www.lasalle.edu/academ/chem/laser_web

15. Tekkaya, A. E., *ME413 Introduction to Finite Element Analysis Lecture Notes*. 2001, Ankara: METU.

16. *MARC User's Manual*. 1994.

17. Tekkaya, A. E., *ME 581 Finite Element Analysis in Solid Mechanics*. 2003, Ankara: METU.

18. LASAG Industrial Lasers, Description and Technical Data

19. Williams, Samuel C., *Report on Titanium the Ninth Industrial Material.* 1965, New York: Brundage, Story and Rose Research Reports Series A-6. p.162

20. Callister, William D., *Materials Science and Engineering an Introduction*. Fourth ed. 1997: John Wiley & Sons Inc. 236-278.

21. Allen, Dell K., *Metallurgy Theory and Practice*. 1975, Chicago: American Technical Society. 159-172, 409-417.

22. Pollack, *Materials Science and Metallurgy*. Fourth ed. 1988: Prentice-Hall.

23. Neely, John E., *Practical Metallurgy and Materials of Industry*. Second ed. 1984: John Wiley & Sons. 117-127.

24. G.Lütjering, J.C. Williams, A. Gysler, *Microstructure and Properties of Materials*, ed. J.C.M. Li. Vol. 2. 2000: World Publishing Co. Pte. Ltd. 1-12.

25. *Mechanical Metallurgy and Passivation of Titanium Implant Alloys.* Retrieved November 20, 2004, from Saint Jose State University Web site: http://www.engr.sjsu.edu/WofMatE/projects/srproject/srproj5.html

27. *MMAT 380 Lecture Notes.* Retrieved November 20, 2004, from The University of British Columbia Web site: http://www.mmat.ubc.ca/courses/mmat380/lectures/2004/Lecture%2018-Titanium(Complete).pdf

28. Song, S. Brown H., *Finite Element Simulation of Welding of Large Structures.* Journal of Engineering for Industry, 1992. 114(4): p. 441-451.

APPENDIX A

A.1 PROPERTIES Of The SELECTED MATERIALS

Table A.1 Main properties of the selected materials [16, 19]

	16MnCr5	x5CrNi_18_9	Ti6Al4V
Poisson's Ratio	0.3	0.3	0.33
Density (g/cm^3)	7.85	7.85	4.43

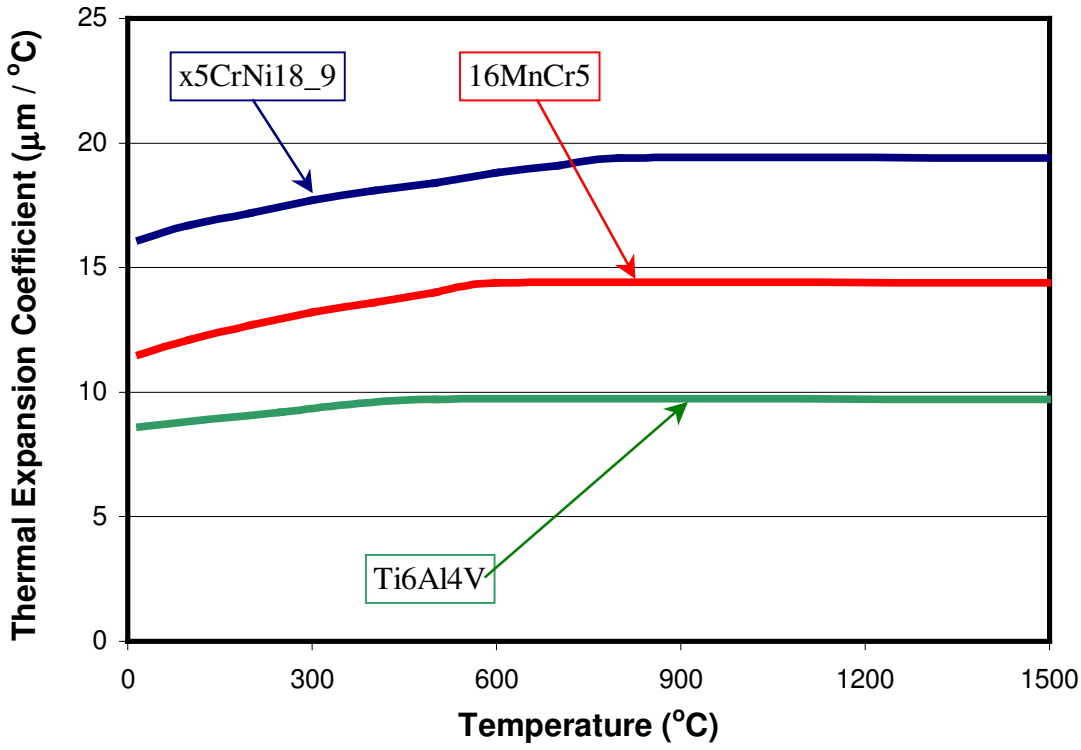

Figure A.1 Thermal expansion coefficients of selected materials

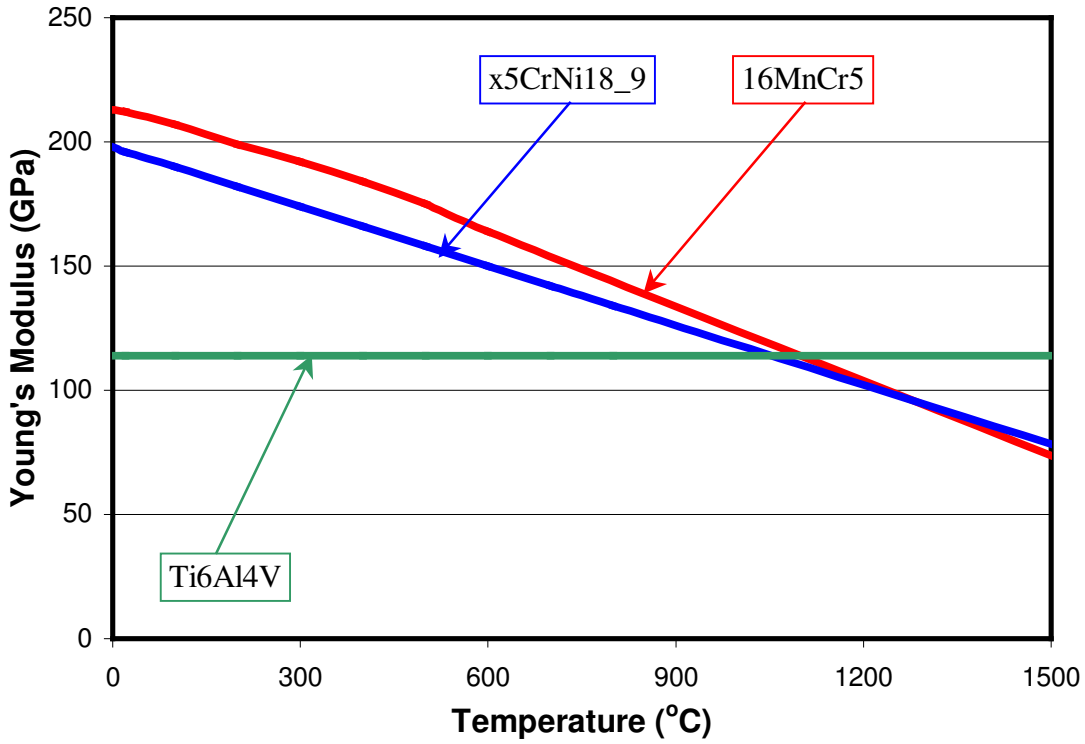

Figure A.2 Young's Modulus characteristics of the selected materials

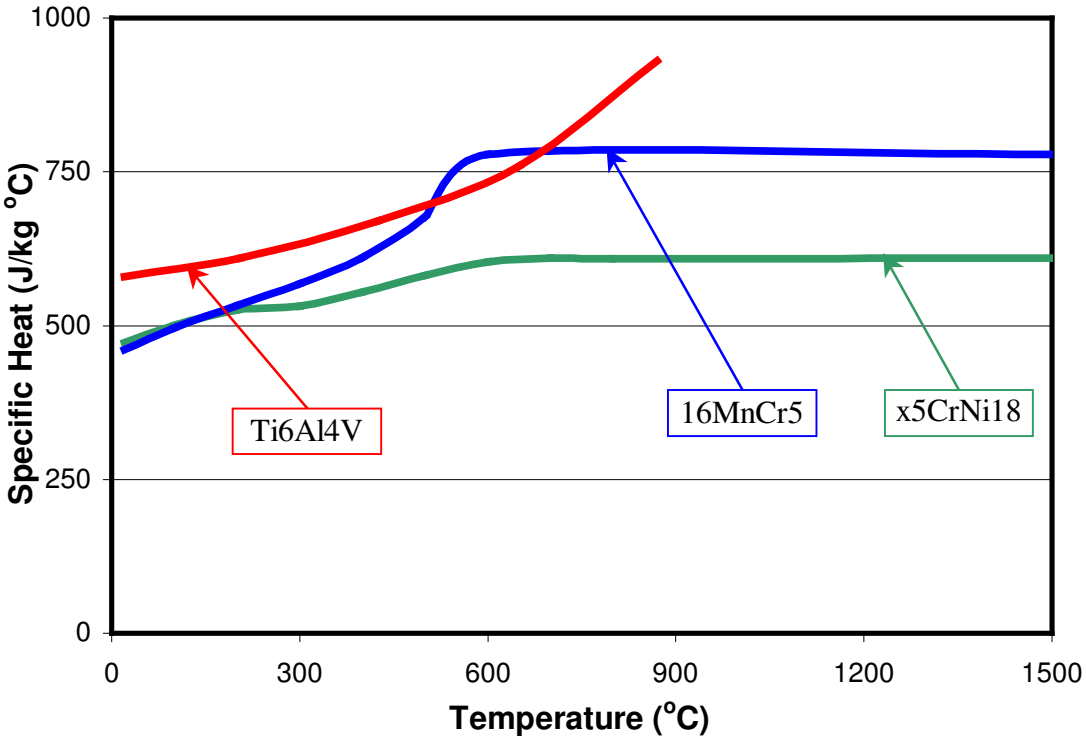

Figure A.3 Specific heat characteristics of the selected materials